INFLUENCE OF THE BEAM AND WINDOW MATERIAL ON LIQUID PHASE TRANSMISSION ELECTRON MICROSCOPY

DISSERTATION

Submitted in partial fulfillment of the requirements for the degree of
Doctor of Philosophy

Department of Chemistry
Faculty of Mathematics, Informatics, and Natural Sciences
University of Hamburg

Submitted by

LINDSEY ANN BULTEMA

Hamburg, Germany

2022

The presented work took place under the supervision of Prof. Dr. R.J. Dwayne Miller at the Max Planck Institute for the Structure and Dynamics of Matter, within the IMPRS-UFAST graduate school from July 2017 to June 2022.

Thesis Evaluation Committee,	Prof. Dr. R.J. Dwayne Miller
	Prof. Dr. Tobias Beck
Examination Commission of Oral Defense,	Prof. Dr. R.J. Dwayne Miller
	Prof. Dr. Robert Blick
	Prof. Dr. Arwen Pearson
Disputation Date,	June 3, 2022
Approved for publication by Prof. Dr. Arwen Pearson,	June 20, 2022

LIST OF PUBLICATIONS

- **Bultema, L. A.,** Bücker, R., Schulz, E. C., Tellkamp, F., Gonschior, J., Miller, R. J. D., & Kassier, G. (2022). The effect of secondary electrons on radiolysis as observed by in liquid TEM: the role of window material and electrical bias. *Submitted to Ultramicroscopy*

  This work is included in Chapter 4

- Azim, S.[†], **Bultema, L. A.,**[†] de Kock, M. B., Osorio-Blanco, E. R., Calderón, M., Gonschior, J., Leimkohl, J-P., Tellkamp, F., Bücker, R., Schulz, E. C., Keskin, S., de Jonge, N., Kassier, G., & Miller, R. J. D. (2021). Environmental Liquid Cell Technique for Improved Electron Microscopic Imaging of Soft Matter in Solution. *Microscopy and Microanalysis*, 27(1), 44-53.

  † Azim, S. and Bultema L. A. are the co-first authors and equally contributed to this work.

  This work is included in Chapter 2.3

- Bücker, R., Hogan-Lamarre, P., Mehrabi, P., Schulz, E. C., **Bultema, L. A.**, Gevorkov, Y., Brehm, W., Yefanov, O., Oberthür, D., Kassier, G., & Miller, R. J. D. (2020). Serial protein crystallography in an electron microscope. *Nature Communications*, 11(1), 1-8.

ABSTRACT

Over the last two decades, liquid phase electron microscopy (LPEM) has been a method used by Chemistry, Biology, and Physics researchers to elucidate the structure, function, and dynamics of samples in their native environment. Mainly it is used for inorganic and organic samples, nanocrystals, soft materials (polymers, gels, proteins, biological molecules), and energy storage processes. Significant advancements involve tailoring the liquid cell (LC) support structure (window dimensions or material) and imaging parameters (dose rate, beam energy, or imaging modality- STEM vs. TEM). However, the following limitations remain: bulging of the window material, thick liquid layers, poor contrast and resolution for low scattering specimens, expensive fabrication steps (time and cost), and beam-induced sample damage or movement. Therefore, this work aims to characterize the influence of the electron beam and window architectures (material and configuration) on LPEM experiments.

This thesis focuses on two areas: 1) fabricating innovative LC architectures and 2) using the nucleation and growth of gold nanoparticles (AuNP) as a probe for radiolysis and the often-overlooked secondary electrons (SE) escape and return. Three LC configurations are presented: 1) the environmental liquid cell (ELC), which uses amorphous silicon nitride (Si_3N_4) windows, a 10 μm spacer, plus pressure and flow to create thin liquid layers. 2) Static 3 mm TEM grid LCs, from commercial carbon grids and for the first time from formvar coated grids. 3) Multi-well LCs with anodic aluminum oxide (AAO) as a spacer and instead of the previously published graphene windows: Si_3N_4, carbon, and formvar. The results from the fabrication of novel LC architectures present ways to control the liquid layer, decrease window bulging, decrease cost, and improve accessibility. The AAO LCs were used to investigate the beam's interaction with the liquid and sample. The LC combinations revealed the dose rate to increase the AuNP growth. The AAO LCs act as individual nano-chambers. This was shown through graphene coated Si_3N_4 window

resulting in bubble generation only within the AAO wells. These results indicated that factors besides liquid layer thickness, generation of radical species, and dose rate must influence the AuNP growth.

Within LPEM, SEs are mainly considered as the cause of Si_3N_4 window charging. Whereas, what is often missed is that SEs are the precursor of the strongest reducing species, hydrated (aqueous) electrons (e^-_{aq}). Therefore, the growth of AuNP was used as a gauge for SE generation with formvar, carbon, and Si_3N_4 AAO LCs. Decreased window conductivity (Si_3N_4) resulted in increased AuNP growth. Applying an electrical bias of +20 V increased and -20 V decreased the AuNP growth. The AuNP growth correlated inversely to the SE emission from the windows. A model describing the influence of window material and bias depicting the SE escape flux (SEEF) and SE return flux (SERF) was introduced that qualitatively matched simulations and electrochemical expectations. Overall, the results from the total work demonstrate the importance of the window material and imaging parameters on the interaction of the electron beam with the solution, sample, and window. Future experiments can use the results presented here to mitigate issues surrounding LPEM.

ZUSAMMENFASSUNG

In den letzten zwei Jahrzehnten wurde die Flüssigphasen-Elektronenmikroskopie (LPEM) von Forschern aus den Bereichen Chemie, Biologie und Physik eingesetzt, um die Struktur, Funktion und Dynamik von Proben in ihrer natürlichen Umgebung zu erforschen. Hauptsächlich wird sie für anorganische und organische Proben, Nanokristalle, weiche Materialien (Polymere, Gele, Proteine, biologische Moleküle) und Energiespeicherprozesse eingesetzt. Zu den wesentlichen Fortschritten gehört die Anpassung der Trägerstruktur der Flüssigkeitszelle (Fenstergröße oder Material) und der Bildgebungsparameter (Dosisleistung, Strahlenergie oder Bildgebungsmodalität - STEM vs. TEM). Die folgenden Einschränkungen bleiben jedoch bestehen: Ausbeulung des Fenstermaterials, dicke Flüssigkeitsschichten, schlechter Kontrast und Auflösung bei Proben mit geringer Streuung, teure Herstellungsschritte (Zeit und Kosten) und strahleninduzierte Probenschäden oder -bewegungen. Daher zielt diese Arbeit darauf ab, den Einfluss des Elektronenstrahls und der Fensterarchitekturen (Material und Konfiguration) auf LPEM-Experimente grundlegend zu charakterisieren.

Diese Arbeit konzentriert sich auf zwei Bereiche: 1) die Herstellung innovativer LC-Architekturen und 2) die Nutzung der Keimbildung und des Wachstums von Goldnanopartikeln (AuNP) als Sonde für die Radiolyse und das oft übersehene Entweichen und Zurückkehren von Sekundärelektronen. Es werden drei LC-Konfigurationen vorgestellt: 1) die Environmental Liquid Cell (ELC), die Fenster aus Siliziumnitrid (Si_3N_4), einen 10 μm großen Abstandshalter sowie Druck und Strömung zur Erzeugung dünner Flüssigkeitsschichten verwendet. 2) Statische 3 mm TEM-Gitter-LCs aus handelsüblichen Kohlenstoffgittern und zum ersten Mal aus formvar-beschichteten Gittern. 3) Multiwell-LCs mit anodischem Aluminiumoxid (AAO) als Abstandshalter und anstelle der zuvor veröffentlichten Graphenfenster: Si_3N_4, Kohlenstoff und Formvar. Die Ergebnisse der Herstellung neuartiger LC-Architekturen zeigen Möglichkeiten zur Kontrolle der Flüssigkeitsschicht, zur Verringerung

der Fensterausbuchtung, zur Kostensenkung und zur Verbesserung der Zugänglichkeit. Die AAO-LCs wurden verwendet, um die Wechselwirkung des Strahls mit der Flüssigkeit und der Probe zu untersuchen. Die LC-Kombinationen zeigten, dass die Dosisleistung das AuNP-Wachstum erhöht. Die AAO-LCs wirken als individuelle Nanokammern. Dies wurde durch ein mit Graphen beschichtetes Si_3N_4-Fenster gezeigt, das zu einer Blasenbildung nur innerhalb der AAO-Wells führt. Die Ergebnisse deuten darauf hin, dass neben der Dicke der Flüssigkeitsschicht, der Erzeugung von Radikalspezies und der Dosisleistung weitere Faktoren das AuNP-Wachstum beeinflussen müssen.

Innerhalb von LPEM werden hauptsächlich SEs als Ursache für die Aufladung des Si_3N_4-Fensters angesehen. Was jedoch oft übersehen wird, ist, dass SEs der Vorläufer der stärksten reduzierenden Spezies, hydrated (aqueous) electrons (e^-_{aq}), sind. Daher wurde das Wachstum von AuNP als Maßstab für die Erzeugung von SE mit formvar, Kohlenstoff und Si_3N_4 AAO LCs. Eine verringerte Fensterleitfähigkeit (Si_3N_4) führte zu einem erhöhten AuNP-Wachstum. Eine elektrische Vorspannung von +20 V erhöhte und -20 V verringerte das AuNP-Wachstum. Das AuNP-Wachstum korrelierte umgekehrt mit der SE-Emission von den Fenstern. Es wurde ein Modell vorgestellt, das den Einfluss des Fenstermaterials und der Vorspannung beschreibt, das den SE escape flux (SEEF) und SE return flux (SERF) darstellt und qualitativ mit den Simulationen und elektrochemischen Erwartungen übereinstimmt. Insgesamt zeigen die Ergebnisse der gesamten Arbeit, wie wichtig das Fenstermaterial und die Abbildungsparameter für die Wechselwirkung des Elektronenstrahls mit der Lösung, der Probe und dem Fenster sind. Zukünftige Experimente können die hier vorgestellten Ergebnisse nutzen, um Probleme im Zusammenhang mit LPEM zu entschärfen.

TABLE OF CONTENTS

LIST OF ABBREVIATIONS

Symbols

σ_{SE} secondary electron coefficient. 98

A

AAO anodic aluminum oxide. iii–v, xiv, xv, 4, 6, 7, 39, 41–43, 45–50, 60–62, 64, 68, 69, 96–98

Ag silver. 2

Au gold. 2

AuNP gold nanoparticles. iii–v, xv, xvii, 3, 4, 36, 38, 50, 55, 57, 60–64, 66, 68–70, 80, 95, 97, 98

B

BIS N,N'-methylenebisacrylamide. xii, 17

BSE back scattered electrons. 71

C

C$_c$ chromatic aberration. 13

C$_s$ spherical aberration. 13

CNT classical nucleation theory. 57

E

e$^-_{aq}$ hydrated (aqueous) electrons. iv, v, 4, 55, 64–70, 97

EDX energy-dispersive x-ray spectrometry. 9

PbS lead(II) sulfide. 2

PNIPAM Poly-N-isopropyl-acrylamide. vi, xiii, 16, 34, 96

S

SE secondary electrons. iii–v, xv, 50, 52, 61, 68–73, 76–81, 84, 86, 90–93, 97

SEBSE SE and BSE. 72

SEE SE emission current density. 87

SEEF SE escape flux. iv, v, 77, 81, 83, 85, 86, 88, 90–93, 98

SEM scanning electron microscopy. 7, 9, 71

SERF SE return flux. iv, v, 77, 81–83, 85–88, 91, 93, 98

Si$_3$N$_4$ amorphous silicon nitride. iii–v, 1, 2, 48, 50, 59, 60, 62, 64–71, 80, 96–98

STEM scanning TEM. 7, 9, 71

T

TEM transmission electron microscopy. 1, 7, 12, 71

LIST OF FIGURES

LIST OF TABLES

1. Introduction

1.1   Liquid Phase Electron Microscopy

Fundamental in-liquid processes within Physics, Chemistry, and Biology occur at the nanometer to even subnanometer scale. Therefore, it is pertinent to have the means to characterize these phenomena in an unperturbed state. Since the 1930s, electron microscopy has aimed to do that.[5] In particular, to elucidate structural details, transmission electron microscopy (TEM) has been consistently used with organic, inorganic, and even biological specimens. TEM requires the samples to be thin, the background/support structure to have a difference in mass-thickness (atomic number, densities), and stability under the high vacuum conditions inside the microscope.[6, 7] As organic and biological samples characteristically have similar mass-thickness as the surrounding medium, a contrast agent is used to stain the sample. Also, cryo TEM vitrifies the samples in amorphous ice to prevent dehydration of the samples.[8, 9, 10] Although these methods can offer extremely high spatial and temporal resolution, they fail to directly show dynamic processes and effects. Alternatively, the environmental TEM (ETEM) emerged to observe reactions with a low vacuum and a humid environment that engulfs the sample.[11, 12, 13, 14] With advancements in nanofabrication, specialized liquid cells (LCs) and subsequently liquid phase electron microscopy (LPEM) surfaced.

For roughly 20 years, LPEM has characterized samples in their native environment by encapsulating a small aqueous sample between two amorphous silicon nitride (Si_3N_4), graphene, or other electron-transparent windows.[2, 15, 16, 17, 18, 19, 20]

In 2003, Williamson *et al.* performed one of the first microfluidic LPEM experiments with the nucleation and growth during the electrodeposition process of copper clusters between two silicon chips with silicon nitride windows. Since then, the interaction of the electron beam with aqueous solutions, followed by the formation of radiolytic oxidating/reducing species, has been used to study corrosion processes and the growth/etching of

nanoparticles.[3, 21, 22, 23, 24] The size and shape of nanoparticles/nanocrystals influence their physical and chemical properties. Therefore, it is crucial to understand and control the morphology and growth mechanisms.[25] Investigating these processes are essential for printed electronics, plasmonics, nanodevices, and medical applications.[1, 26, 27] By 2009, Zheng *et al.* observed Pt nanoparticle growth to sub-nm resolution by beam illumination.[28] Observing nanoparticle growth and etching has been applied to PbS, Ag, Au, and Au nanoparticles.[28, 29, 30, 31] Additionally, more complex systems such as metal-organic frameworks (MOF) and core-shell growth with Au-Pd have been investigated.[32, 33] Two factors dominating the LPEM growth kinetics are electron beam-induced radiolysis and precursor solution composition.[1] Therefore, a lot of experimental and theoretical work has been done to assess these influences.[3] For example, Pb growth switches from island to aggregative growth with HCl addition.[34] Additionally, a capping agent can control the size.[35] The fundamental work by Schneider *et al.* quantitatively described the radiochemistry of LPEM systems with varying dose rates, liquid cell geometry, and solution pH.[3] Woehl *et al.* observed different growth mechanisms and morphologies with different beam currents. Furthermore, Park *et al.* used Au nanoparticles and observed that the growth follows a power-law dependency with dose rate.[25]

Soft materials, such as biological molecules, polymers, gels, and proteins, have low atomic numbers and are challenging to image with LPEM.[36] The challenges are also due to the low contrast to the surrounding medium and sensitivity towards electron beam-induced radiolysis.[37, 38, 39, 40, 41] With a liquid flow cell in 2009, de Jonge *et al.* successfully imaged whole biological cells with 4 nm spatial resolution.[42] To do so, they cultured the fibroblast cells on the Si_3N_4 windows and added a 10 μm spacer to account for the $\sim$ 7 μm height of the sample.[42] Later, PC3 cells and rotavirus particles were observed to sub-cellular levels.[15, 43] The general feasibility of LPEM for imaging biological dynamics was confirmed through imaging a fundamental biological function: nucleic acid base pairing.[43, 44] Labeling agents such as gold nanoparticles and fluorescent dyes have been used as molecular tags to circumvent the poor spatial resolution associated

with soft materials.[45] Dahmke *et al.* labeled epidermal growth factor receptors on breast cancer cells with quantum dot nanoparticles and correlated the LPEM results with fluorescence microscopy.[45] Whereas, Gnanasekaran *et al.* showed *in situ* that a simple $NiCl_2$ salt readily and semi-reversibly stains vesicles made from lipopolysaccharides.[36] The fact that LPEM has been used to elucidate the interaction of macromolecules and cellular functions with and without high scattering tags demonstrates the feasibility of LPEM for medical research and drug development.

The increase in energy demand requires developing and investigating alternative energy sources. Subsequently, LPEM has emerged as a method to characterize energy storage processes. In particular, dendrite formation in batteries, which can cause short-circuiting or explosions, is investigated with LPEM.[1] In 2014 multiple groups observed Li dendrite formation and dissolution with common Li-battery electrolytes.[46, 47, 48] These initial results have led to the investigation of additives to suppress dendrite formation.[49, 50, 51] Furthermore, LPEM has been used to research the lithiation/delithiation of lithium batteries.[52] These examples show that LPEM is a versatile method for electrochemically investigating Na/K-ion, Li-ion, alkalis metal, metal-air, Li-sulfur, and solid-state batteries.[53]

LPEM can be used to investigate a wide variety of samples. However, after roughly two decades of research, limitations remain with LC architectures and imaging. Bulging of the Si_3N_4 windows results in thick liquid layers and an inability to achieve sufficient contrast and resolution for low scattering specimens.[54] In addition, LC fabrication is expensive and time-intensive.[55] Progress has been made in terms of modeling radiolysis.[3, 25, 56] However, there is still a need to understand how the electron beam interacts with different samples and window materials.

1.2 Motivation and Structure of this Work

To tackle the issues above of window bulging, thick liquid layer, and costly fabrication, this work focuses on characterizing the beam and window material/configurations' influence on LPEM experiments. It centers on 1) fabricating novel liquid cell architecture in Chapter 2 and 2) using the growth of gold nanoparticles to investigate inelastic scatting events

pervasive within LPEM: radiolysis (Chapter 3) and the often disregarded secondary electron escape and return (Chapter 4).

Chapter 2 begins with introducing electron microscope methods (sec. 2.2.1), followed by an overview of LC configurations and window materials (sec. 2.2.2) and the trade-offs between liquid thickness, resolution (sec. 2.2.4), and window bulging (sec. 2.2.5). To control the liquid layer and disregard window bulging, the environmental liquid cell (ELC) is introduced (sec. 2.3). Presented within this section are the modifications to the holder (sec. 2.3.2), the flow capabilities (sec. 2.3.3), different ways to calculate thickness (sections: 2.3.4, 2.3.5, and 2.3.6), and the control of the spatial resolution with liquid layer (sec. 2.3.7). Finally, the degradation of polymeric nanogels (sec. 2.3.8) depicts beam-induced radiolysis. The second half of this chapter introduces universal LC architectures based on 3 mm formvar and carbon TEM grids (sec. 2.4). This LC architecture is followed by confined multi-well liquid cells with elliptical windows (sec. 2.5.1) and anodic aluminum oxide (AAO) LCs (sec. 2.5.2). Overall, Chapter 2 presents ways to control the liquid layer, decrease window bulging, and improve cost and accessibility.

Chapter 3 investigates the interaction of the electron beam with aqueous solutions via the growth of gold nanoparticles (AuNP). Therefore, this section establishes fundamentals such as elastic and inelastic scattering (sec. 3.2.1) followed by the radiolysis of water (sec. 3.2.2). As AuNP growth is used within the remainder of the work, the reduction (sec. 3.2.3.1), nucleation (sec. 3.2.3.2), and growth (sec.3.2.3.3) mechanisms are presented. The next part focuses on the experimental results of AuNP nucleation and growth in AAO LCs with different windows as a way to probe a main radiolytic species: hydrated (aqueous) electrons (e^-_{aq}). This chapter introduces two ways to pick and track AuNP growth (sections 3.4.1 and 3.4.2). It presents the influence dose rate has on the total number and area of AuNP (sec. 3.5) and validates a means for the sacrificial scavenging of graphene windows (sec. 3.5.1). Finally, it connects growth rates to the concentration of radical species (sec. 3.6.1), and reaction/diffusion limited growth (sec. 3.6.2). The results indicate AuNP growth dynamics are influenced by more than the liquid layer, dose

rate, and window properties.

Chapter 4 examines the influence secondary electron escape and return have on AuNP growth. Section 4.2 introduces the connection between hydrated electrons (which are the primary driver of AuNP growth) and secondary electrons (formed during scattering events). Subsequently, Section 4.4 shows that the AAO window material influences AuNP growth. The next portion focuses on biasing the LC windows, showing that secondary electrons influence AuNP growth (sec. 4.5) and measuring the secondary electron coefficient (sec. 4.5.1). A model (sec. 4.5.2) is introduced for the secondary electron emission and return to describe the results and validated with simulations (sec. 4.5.3). Finally, an electrical hookup and LC configuration is presented in Section 4.6 that influences the secondary electron emission and return and gates AuNP growth.

Chapter 5 summarizes the findings of the three chapters and provides a brief outlook.

2.   Fabrication and Implementation of Novel Liquid Cells

2.1   Motivation & Synopsis

This chapter addresses the issues facing liquid phase electron microscopy (LPEM) by fabricating novel liquid cell assemblies. The fundamentals section begins with a brief overview of the three electron microscope modalities, followed by a description of the liquid cell (LC) configurations and architectures used with LPEM. Finally, I introduce two issues facing LPEM: 1) the balance between resolution and liquid thickness and 2) window bulging.

Section 2.3 presents a way to control the liquid layer thickness with the environmental liquid cell (ELC).[10] The hydration of polymeric nanogels exemplifies the flow properties of the ELC. I describe multiple ways to determine the window and liquid layer thickness instead of electron energy loss spectroscopy (EELS). I showcase an excellent agreement between thicknesses determined from parallax, the total intensity ratio, and the computed thickness values from a Monte Carlo simulation. Finally, I show the dependency of liquid thickness and resolution. The results from this section are published in Ref.[10].

Section 2.4 presents alternatives to the silicon nitride LCs employed in Section 2.3 by using 3 mm TEM grids as support structures. I present formvar and carbon window materials as alternatives to the graphene liquid cell architecture (fundamentals Section 2.2.2). This is the first time formvar is investigated for LPEM. The presence of liquid was validated by liquid thickness calculations and the observation of gold nanoparticle growth. Although I show formvar and carbon are suitable window materials, the results also showcase a significant downside of 3 mm LCs: irregular pockets of liquid.

Section 2.5 defines ways to circumvent window bulging and the sporadic liquid pockets with confined microwell LCs. Briefly, I present architecture based on traditional silicon nitride windows. Furthermore, I combine the formvar and carbon 3 mm grids from the previous section to encase anodic aluminum oxide (AAO) sheets. With this microwell

configuration, I adapt the total intensity thickness method presented in Section 2.3 to account for multiple scattering from the AAO. Finally, I characterize the success of the AAO-LC formvar and carbon architectures by liquid thickness and the observation of gold nanoparticle growth.

2.2 Fundamentals of LPEM

2.2.1 Electron Microscopy of Samples in Hydrated Environments

The five primary electron microscope modalities for imaging samples in aqueous environments are transmission electron microscopy (TEM), scanning TEM (STEM), scanning electron microscopy (SEM), environmental SEM (ESEM), and environmental TEM (ETEM) (Figure 2.1).

Briefly, TEM is a vacuum column with a thermionic or field emission electron source at one end and a detector at the other. A stationary and uniform electron beam between 60 to 300 keV is passed through electrostatic and magnetic lenses and is illuminated onto a sample's surface. Adjusting these lenses and apertures controls the electron beam's: divergence/convergence, magnification, focus, illumination area, angle, and brightness on the specimen. For example, increased illumination angles and brightness are possible with larger apertures.[57] The objective aperture after the sample defines the image contrast, resolving power, and sets the electron beam's opening semi-angle (α), as shown in Figure 2.1a. This objective lens aperture collects the resulting shadow image, which is magnified by other lenses towards the image plane. Electromagnetic post-specimen lenses magnify the image on the detector. Concerning the downward traveling electron beam and an LC configuration, the highest spatial resolution is achieved when the sample is positioned at the bottom window.[58] This placement is due to the layer below the sample obscuring/blurring the projected image on the detector. Image resolution is influenced by the liquid layer, which broadens the energy spread of the beam due to increased scattering and chromatic aberration of the objective lens.[54] Image contrast and resolution are discussed in more detail in Sections 2.2.3 and 2.2.4, respectively.

With STEM, electromagnetic condenser lenses and electric coils create a sub-nm
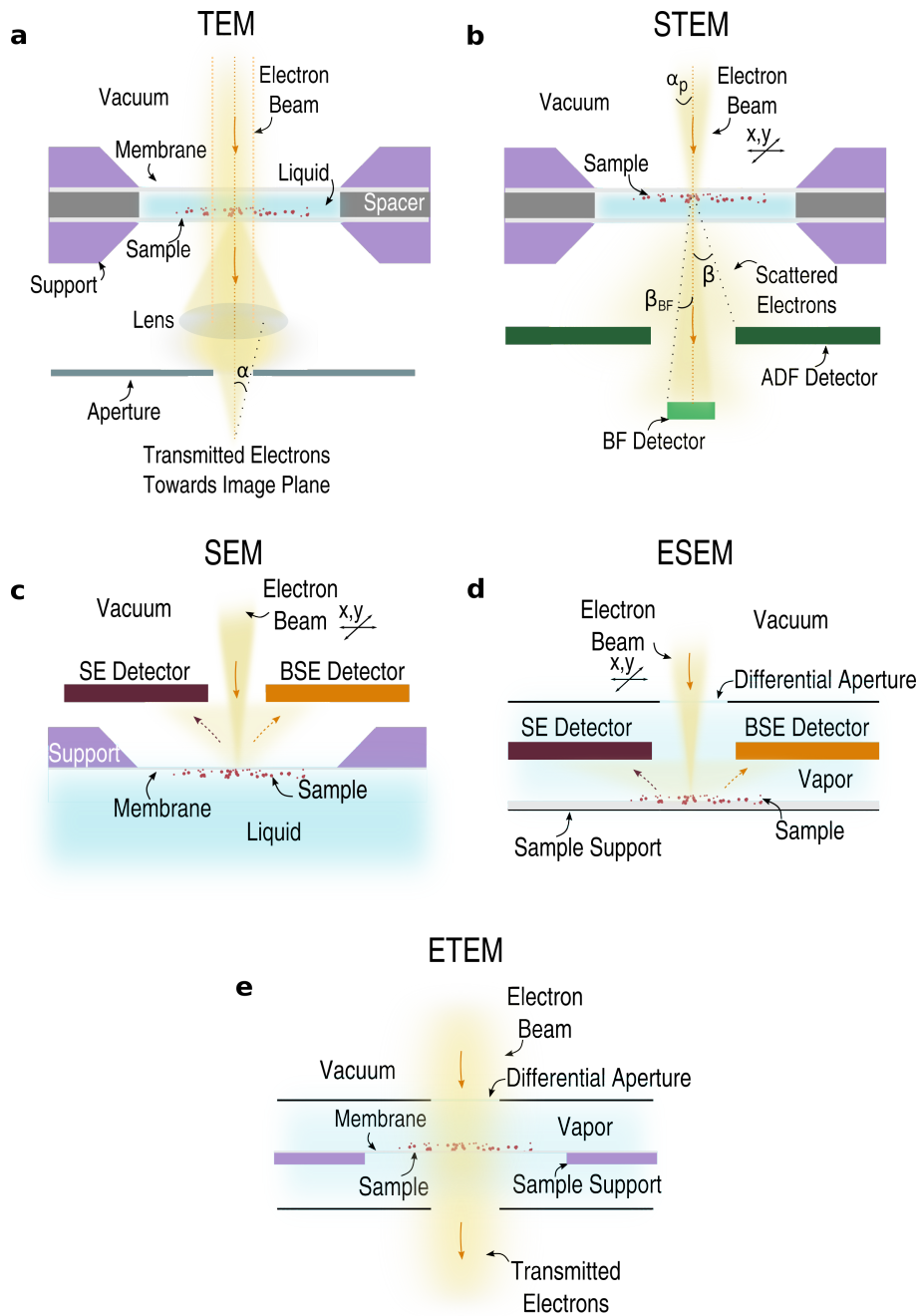
Figure 2.1: Electron Microscopy methods: a) Transmission electron microscopy (TEM) with the sample at the bottom window. The objective aperture adjusts the opening semi-angle towards the camera α. b) Scanning TEM (STEM) with the sample at the top window. α_p is the electron probe semi-angle. The image is detected either by the annular dark field (AFD) detector with an opening semi-angle β or the bright-field (BF) detector with an opening-semi-angle β_{BF}. c) Scanning electron microscopy (SEM) of the sample under electron transparent membrane, with a secondary electron (SE) detector and back-scattered electron (BSE) detector. d) Environmental SEM (ESEM) with the sample in a liquid and vapor environment. e) Environmental TEM (ETEM) with liquid and vapor and where the differential apertures separate the sample and vacuum.

convergent electron probe (α_p) that can scan across the sample (Figure 2.1b). The transmittance from one location on the sample is detected.[59] STEM images are formed by elastically scattered electrons larger than the opening semi-angle (β) of the annular dark field (ADF) detector or the opening semi-angle (β_{BF}) of the brightfield detector.[54] Here, the best resolution is when the sample is closer to the top window. This placement is because electron scattering and beam broadening or blurring increase as the sample is located deeper in the liquid layer.[42, 60, 61] Beam broadening is not the case for TEM as the larger beam will not be significantly broadened.[54] The lack of post-specimen optics with STEM allows thicker samples to be imaged.[58] This is why STEM was mostly used with the LPEM biological sample examples presented in Section 1.1.[54]

SEM uses a focused, convergent beam similar to STEM. This beam scans over the sample surface. However, the beam is between 500 eV and 30 keV, and the detectors collect secondary electrons and backscattered electrons.[22] Electron scattering and secondary electrons are discussed in Sections 3.2.1 and 4.2, respectively. Figure 2.1c depicts an SEM with a single membrane support, which allows the imaging of samples fully immersed in liquid. Environmental SEM (ESEM) is also used for imaging a sample's surface in a vapor environment. The differential apertures separate the sample from the vacuum (Figure 2.1d).[58]

Analytical modes have been applied to electron microscopes to characterize the elemental composition. Electron energy loss spectroscopy (EELS) can be used to probe the valence electron configuration of the sample. Here, a spectrometer analyzes the transmitted electron beam.[62, 63, 64] This method is also used to determine liquid layer thicknesses.[65] The elemental composition of a sample can be investigated with energy-dispersive x-ray spectrometry (EDX). Here an x-ray detector above the sample records the generated x-rays from the electron beam interacting with the inner shell electrons of atoms.[22, 66]

The environmental TEM (ETEM), or ESTEM, or an open environmental cell, uses differential pumping to maintain the sample chamber at a higher pressure (Figure 2.1d).

However, it is still impossible to reach atmospheric pressure with this method. That means most liquids will evaporate, and salts will precipitate.[1] So ETEM is predominantly used for gas-phase experiments.[67] Therefore, to facilitate TEM, STEM, and SEM imaging of aqueous environments, different thin-film liquid cell (LC) assemblies have been developed to encapsulate the sample.[58]

2.2.2   Configurations of Liquid Cells Used for Transmission Electron Microscopy

Herein I present a brief overview of the current liquid cell (LC) architectures. Overall, two main branches of LCs exist: static and flow. Within these branches, the window material, fabrication, assembly process, and whether commercial or self-made, are varied. Figure 2.2 depicts some standard LC assemblies.
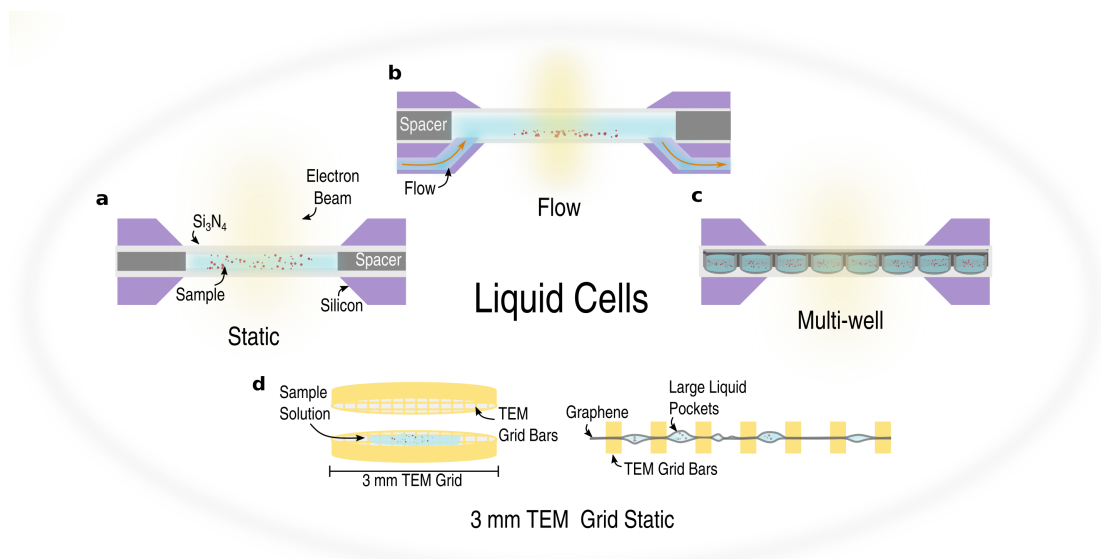
Figure 2.2: Schematic depicting the common LCs. a) static LCs with silicon nitride membrane; b) silicone nitride membrane with microfluidics; c) multi-window silicon nitride membrane; d) graphene liquid cell.

Historically static LCs consist of two frames made from silicon, contain a spacer of a set height, and an electron transparent window. The sample specimen solution is sandwiched between the two windows and imaged (Figure 2.2a). The dimensions of the static LCs with silicon nitride windows vary from 3 mm discs suitable for a conventional TEM specimen

holder to rectangles requiring their own TEM holder. If a conventional TEM specimen holder is used, the LCs are bound together. This is either during the fabrication of the LCs or after the LC assembly. Whereas with the dedicated LC holder, the two LC chips are not bonded to one another but aligned and secured inside the holder with o-rings. The fabrication of silicon nitride windows is not within the scope of this thesis. However, preparation generally requires detailed dry thermal oxidation of silicon, chemical vapor deposition, photolithography, etching, wafer bonding, and cleaning steps. [68, 69, 70] To allow for flow and exchange of sample solutions, tubing is added to the holder's arm, and LC chips with microfluidic flow channels are fabricated (Figure 2.2c). In addition to flow capabilities, electrical contacts for heating experiments and to investigate electrochemical processes can be implemented.[14, 48, 71, 72] As an alternative to preparing LC chips in-house, there are commercial options from: Protochips Inc, Humminbird Scientific, and DENSsolutions. In 2014, Dukes *et al.* prepared silicon nitride microchips with integrated microwells to circumvent window bulging.[73] Due to the generation of gas bubbles and window dimensions, window bulging is a central issue of LPEM and is presented in more detail in Section 2.2.5.

In 2012, graphene emerged as an alternative to silicon nitride LCs (Figure 2.2 d and c).[74] Here two graphene sheets suspended on 3 mm TEM grids encapsulate the small droplet of specimen solution. The two films adhere by van der Waals forces and create pockets of specimen solution. Graphene LCs are used to investigate small amounts of liquid and biological specimens to a high resolution, up to 0.1 nm. [25, 45, 74, 75, 76, 77, 78, 79, 80, 81, 82, 83] Thin (1 - 10 nm) monolayer to multilayer graphene[84, 85] is electron transparent [86], mechanically stable [87], exhibits good conductivity [88], and is not permeable to water.[75, 89] The low atomic number (Z = 6) of carbon compared to silicon (Z=14) and nitride (Z=7) atoms reduce the electron scattering and improve resolution. In addition to graphene, it has been found that graphene oxide and carbon films on 3 mm TEM grids also produce LCs.[35, 90, 91, 92, 93] Here, the liquid pockets are less than 200 nm. Graphene has also been used to encapsulate specimens cultured

on silicon nitride chips, whereby allowing for larger biological specimens to be imaged.[94] Furthermore, due to the uncontrollable liquid thickness and low reproducibility, graphene has been combined with various micro-well designs.[95, 96]

Besides selecting the window configuration, three factors are limiting LPEM: image contrast, image resolution, and adverse beam effects from scattering. The latter is covered in Section 3.2.2. In general, a decreased resolution is caused by an increase in multiple scattering events, which are determined by the liquid layer and properties of the window material.[22]

2.2.3 Contrast

Contrast is essential for good TEM images. The minimum contrast of an object detected by the microscope must have a signal 3-5 times larger than the background noise as described by the Rose criterion.[97] Within TEM, there are two main contributors to contrast: amplitude and phase contrast. The intensity difference between the object (I_2) and background (I_1) can be used for the amplitude contrast (C):

$$C = \frac{I_2 - I_1}{I_1} = \frac{\Delta I}{I_1} = 1 - e^{-Q\Delta t} \qquad (2.1)$$

where Q is the total elastic scattering cross-section and Δt is a change in the sample thickness.[98] With thick or high atomic number samples altering the electron-matter interactions, amplitude contrast can be considered mass-thickness or Z- contrast. Lowering the electron energy and smaller objective apertures results in improved contrast.[57]

Phase contrast arises from the interference of scattered and unscattered electron waves. For high resolution TEM, phase contrast is used. With liquid layers greater than 0.17 μm, phase contrast is not possible due to multiple scattering events.[54] The extent to which electrons undergo a phase shift depends on the material's thickness, lattice defects, or composition. At the interface between these phases, phase contrast images are generated. Phase shifts increase with atomic number and decrease with electron energy.[99] Although still with limitations, phase plates have been used to increase phase contrast.[100, 101, 102]

Within the scope of this work, phase plates are not used.

2.2.4 Resolution

With a light microscope, the resolution is diffraction-limited and defined as the minimum distance in which two objects are separable:

$$\delta = \frac{0.61\lambda}{\mu \sin \beta} \tag{2.2}$$

where λ is the wavelength, μ is the refractive index, β is the semi-angle of collection of the magnifying lens.[7, 103] This is roughly 300 nm for a light microscope.[104]

With LPEM, the parallel electron beam interacts with the specimen solution that is confined between two transparent windows (Section 2.2.2). Increased sample/liquid thickness increases inelastic scattering, resulting in increased spherical and chromatic aberrations, limiting resolution.[58, 105]

Spherical aberrations (C_s) are from the lens magnetic field and occur when off-axis electrons are bent stronger towards the optical axis. This limits achievable resolution at higher magnifications due to the distortion in the imaging plane. C_s is dominant for thinner samples, such as graphene LCs. C_s can be corrected by diverging the off-axis rays to converge and spatially overlap.[106, 107] Here optimizing, the objective lens angle (α, Figure 2.1a) results in a point resolution (d_s),

$$d_s = C_s \alpha^3 \tag{2.3}$$

typically C_s coefficient is in the range of 1-2 mm. Typical spatial resolution for corrected and uncorrected 200 keV TEM are 0.08 nm and 0.24, respectively.[7, 108]

Chromatic aberrations (C_c) are due to the energy spread of the electrons (ΔE) or low beam energy (E_{kin}). For thin samples, C_c's effects on image resolution are smaller than C_s. Therefore, to decrease C_c, thin samples are preferred. The chromatic blur (d_c) is described as:

$$d_c = \alpha_s C_c \frac{\Delta E}{2 E_{kin}} \qquad (2.4)$$

this takes into consideration the semi-opening angle (α_s), chromatic aberration coefficient (C_c), and the energy distribution of the beam (ΔE) and beam energy (E_{kin}). The energy distribution of transmitted electrons (ΔE) is given by:

$$\Delta E = \frac{N_A e^4 Z \rho d_{liquid}}{2 \pi \varepsilon_0^2 W m_0^2 V^2} \qquad (2.5)$$

with Avogadro's number (N_A), elementary charge (e), atomic number (Z), density (ρ), liquid layer thickness (d_{liquid}), permittivity of space (ε_0), atomic weight (W), mass (m_0), and the velocity of electrons (V). In the case of TEM, the highest resolution is obtained when the sample is placed on the bottom window. Combining Equations 2.5, 2.4, and assuming Z of water to be 4.7, the TEM resolution (d_{TEM}) is calculated:

$$d_{TEM} = 6 \cdot 10^{12} \cdot \frac{\alpha_s C_c d_{liquid}}{E_{kin}^2} \qquad (2.6)$$

Therefore, based on Equation 2.6, the liquid layer thickness influences resolution and the applied electron dose. Additionally, astigmatism can hinder the resolution when the introduced apertures are not cleaned or centered on the axis. This results in a disruption in the magnetic field and beam deflection.

de Jonge calculated that the electron dose limited resolution and how it scales, $D^{=1/4}$, with increasing dose. Therefore the resolution can be increased by: increasing the applied dose, decreasing the liquid layer, decreasing window thickness, or changing window material (silicon nitride to graphene).[54]

2.2.5   Window Bulging

Due to the pressure difference between the hermetically sealed LC and the high vacuum inside of the TEM, window bulging can occur (Figure 2.3).

For example, Woeh *et al.* described bulging to change the thickness of the liquid by up to 100%.[30] In general, window bulging increases with thinner windows (Figure 2.3a,b)
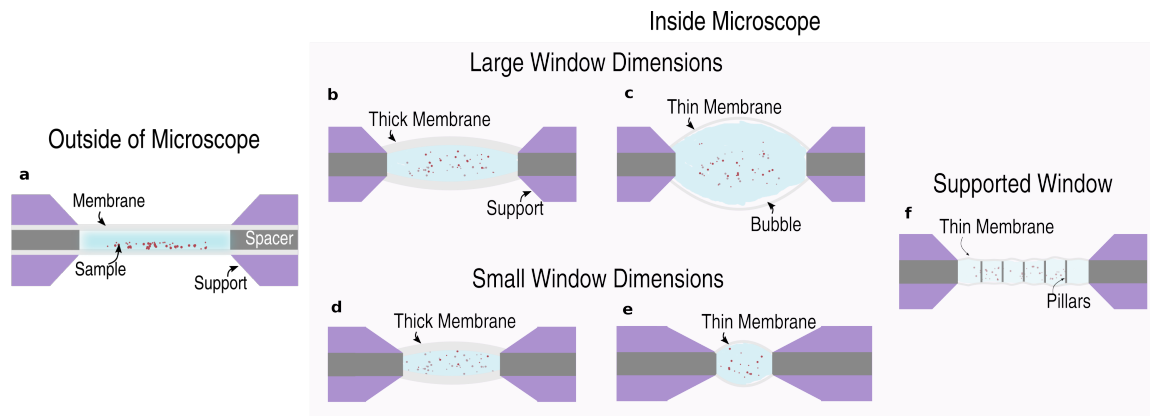
Figure 2.3: Schematic depicting window bulging. The window outside of the microscope (a) vs. inside the microscope (b-f). Influence of larger window dimensions with thick (b) and thin (c) membranes, smaller window dimensions with the thick (d) and thin (e) membranes, and membranes with supported windows (f)

and decreases with smaller window dimensions (Figure 2.3c,d).[30] As highlighted in the previous section (2.2.4), the liquid thickness directly influences the resolution; therefore, the window thickness and dimension are adjusted to control the bulging and improve resolution.[24, 95] Additionally, it is possible to modify the LC to include micro-wells or pillars. These structures improve window stability and decrease bulging (Figure 2.3e). [30, 73, 95, 109, 110]

The window bulging can also result in gas bubbles within the LC. Although the regions with bubbles exhibit decreased scattering and improved resolution, it increases the likelihood of the window bursting inside the TEM. However, as the thought of improved resolution sometimes outweighs the potential bursting of a window, some have purposefully created bubbles to thin the liquid layer and improve resolution.[111] However, this comes at the expense of exposing the sample to a dose that produces enough radiolytic species (H_2 and O_2) for bubble generation (Section 3.2).[30, 111, 112] Improving the wettability of the windows is another way to decrease possible bubble formation and in-homogeneous liquid layers and fluid fronts.[30] This is easily achieved through a plasma cleaning the LCs before assembly.[113]

2.3 Controlled Liquid Layer with the Environmental Liquid Cell

As described in the fundamentals section (2.2.4), the liquid layer directly influences the obtainable resolution. Herein, the environmental liquid cell (ELC) is introduced. This design builds upon the static ELC presented by Inayoshi *et al.* with liquid flow cell technology, thus merging the high resolution and contrast potential of ETEM with the ease of use and high reproducibility of Si_3N_4-technology via the simple addition of a 10 μm polyimide (Kapton) spacer.[10, 17] The efficacy of this concept is demonstrated through the hydration of Poly-N-isopropyl-acrylamide (PNIPAM) nanogels (NGs) and characterization of the controllable liquid and window thicknesses.

2.3.1 Experimental

2.3.1.1 Sample Preparation

Gold nanoparticles were purchased from Sigma Aldrich GmbH. An aqueous suspension of polystyrene nanoparticles of size 0.1 μm was purchased from Sigma Aldrich.

2.3.1.2 Nanogel Synthesis

Poly-N-isopropyl-acrylamide (PNIPAM) nanogels (NGs) were synthesized via a well-established precipitation polymerization.[114] N-isopropyl-acrylamide (NIPAM, 100 mg), bis-acrylamide (7.8 mg), and sodium dodecyl sulfate (2 mg) were dissolved in Milli-Q-water (5 mL), and purged with argon for 1 h. The solution was then heated to 70 $^\circ$C and subsequently started upon the addition ofpPotassium persulfate (2 mg in 1 mL water). The polymerization was stirred for 4 h at 70 $^\circ$C. The product was purified by dialysis in water for 5 days. The product was lyophilized and stored in the fridge. ^{1}H-NMR (400 MHz,

D$_2$O); δ: 1.19 (s, 6 H, isopropyl groups of NIPAM), 1.62 (br, 2 H, polymer backbone), 2.15 (br, 1 H, polymer backbone), 3.92 (br, 1 H, isopropyl group NIPAM). The resultant nanogels were dispersed in water at 1 mg/mL.
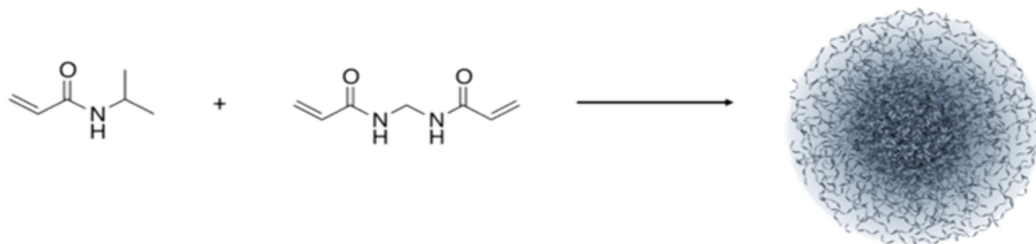
Figure 2.4: Synthesis of PNIPAM NGs from N-isopropyl-acrylamide (NIPAM) and N,N'-methylenebisacrylamide (BIS)

Poly-N-isopropyl-acrylamide (PNIPAM) nanogels (NGs) with a silica nanoparticle in their core were prepared following a previously reported methodology.[115] Briefly, 90 nm size silica nanoparticles were synthesized using the Stöber method and then modified with 3-(trimethoxysilyl) propyl methacrylate (TPM) (5.3982 x 10^{-18} g TPM per silica nanoparticle) by stirring the silica nanoparticles together with the silane for 12 h at r.t. and then refluxing the mixture for 1 h. The modified silica nanoparticles were centrifuged (6000 rpm) three times and re-dispersed in denatured ethanol. Modified silica nanoparticles (size: 90 nm) (10 mg), NIPAM (100 mg), BIS (7.8 mg) and sodium dodecyl sulfate (2 mg) were dispersed in Milli-Q-water (5 mL), purged with argon for 1 h and then heated to 70 °C. The reaction was initiated by adding a potassium persulfate solution (3 mg in 1 mL water). The particles were centrifuged (6500 rpm, 1 h) three times and re-dispersed in fresh Milli-Q-water. ^{1}H-NMR (400 MHz, D$_2$O); δ: 1.14 (s, 6 H, isopropyl groups of NIPAM), 1.60 (br, 2 H, polymer backbone), 2.02 (br, 1 H, polymer backbone), 3.91 (br, 1 H, isopropyl group NIPAM).
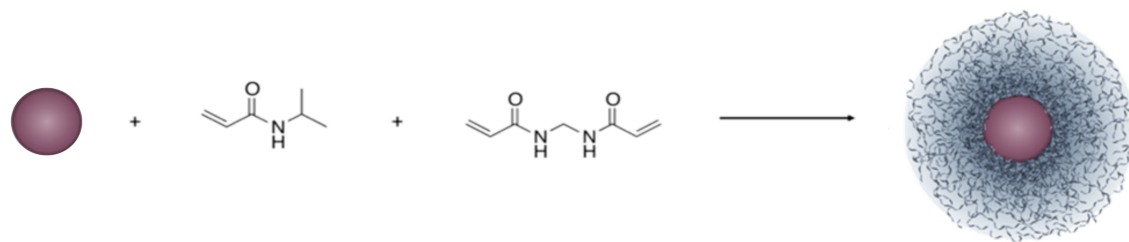
Figure 2.5: Synthesis of PNIPAM NGs with silica nanoparticles from modified silica nanoparticles, N-isopropyl-acrylamide (NIPAM) and N,N'-methylenebisacrylamide (BIS)

2.3.1.3 Transmission Electron Microscopy

TEM was performed in the bright-field mode in a JEOL JEM-2100 operated at 200 keV, and fitted with a TVIPS TemCam F216 camera without an energy filter. All experiments were performed at room temperature (approximately 23 °C). The dose calibration was done using the camera image's absolute count values, which were calibrated from the phosphor screen current readout.

2.3.1.4 Data Analysis

The micrograph was assumed to be a noisy image of multiple particles of roughly similar shapes with no preferred orientation. The 2D Fourier transform (2DFT) of the images with its conjugate were multiplied to obtain the power spectrum of the micrographs. This was used to observe the average structure of the particles. The 2DFT has desirable properties such as insensitivity to particle locations. The noise contribution generally conforming to a power-law makes the power spectrum a useful data reduction and filtering tool. The spherical symmetry of the particles is preserved in the power spectrum, allowing further data reduction by computing the radial average of the 2D power spectrum. These components become additive, assuming the absence of correlations between signal and noise. An empty micrograph is used to estimate a spectral signal-to-noise ratio as a function of spatial frequency (ω). The additive nature of signal and noise was deduced from the following equation:

$$\phi(\omega) = \frac{|S(\omega)|^2}{|S(\omega)|^2 + |N(\omega)|^2} \tag{2.7}$$

where $\phi(\omega)$ is called an optimal filter.[116] The term $S(\omega)$ is the signal, $N(\omega)$ is the noise, and the two of these add up to give the measured signal $C(\omega)$. It is thus derived that the measured signal equals:

$$|C(\omega)|^2 = |S(\omega)|^2 + |N(\omega)|^2 \tag{2.8}$$

and implies that

$$|S(\omega)|^2 = |C(\omega)|^2 - |N(\omega)|^2 \tag{2.9}$$

and therefore signal-to-noise ratio based on spatial frequency (ω) is as given by the following equation:

$$\phi[\omega] = \frac{|C(\omega)|^2 - |N(\omega)|^2}{|N(\omega)|^2} \tag{2.10}$$

with the radial average of the Fourier transform of the micrograph with particles $(C[\omega])$ and the micrograph without particles $(N[\omega])$. As this quantity is computed on the whole image and not for individual particles of known or inferred shape, it does not represent a true signal-to-noise ratio. The true signal-to-noise ratio depends on the signal's degradation due to the water layer, which is not examined here. However, it can be used as a comparative measure of image quality, defining the total signal as the sum of the signal ratio.

2.3.1.5 *Objective Angle Calibration*

The diffraction pattern of aluminum was used as a reference for calibration of the objective angle.[117] Following the insertion of the objective aperture, the shadow image was recorded. It was found that the objective aperture coincided almost perfectly with the second Al diffraction ring (200). A more precise measurement from the radial function of the objective aperture cutoff yielded an effective cutoff d value of d=1.99 Å

Table 2.1: Parameters for Objective Angle Calibration

Miller Indices h k l	Lattice Spacing d (Å)	Intensity (I)	Lattice Constant a (Å)
200	2.024	47	4.018

using λ = 2.51 x 10^{-12}m,

$$\theta = \frac{\lambda}{2 \cdot d} \tag{2.11}$$

$$\theta = \frac{2.51x10^{-12}}{2 \cdot 1.99 \cdot 10^{-10}} \tag{2.12}$$

with θ = 6.3 mrad, an objective angle ($\alpha = 2\theta$) of 12.6 mrad was used for subsequent calculations.

2.3.2   The Environmental Liquid Cell Holder Setup

The two factors affecting the resolution in LPEM are excessive background scattering in the windows and bulging from Si_3N_4 windows leading to increased background scattering in the liquid (Fundamentals 2.2). Background scattering in the windows can be reduced by using thinner Si_3N_4 while bulging depends on its width and thickness (Fundamentals 2.2.5).[118] To reduce these effects, the aspect ratio of the previously reported nanofluidic cell window design was modified from 50×50×0.05 μm to 200×30×0.02 μm to reduce bulging (Figure 2.6).[17]

The window layout shown in Figure 2.6 was designed in-house, and Simpore, USA, manufactured liquid cell chips. A fully assembled nanofluidic cell consists of two silicon chips with a silicon nitride window, one with flow openings (bottom) and one without (top). A 150-micron deep trench connects the flow openings to the window area to reduce flow resistance. Two chips are placed in the Environmental Liquid Cell setup (Figure 2.7).

Figure 2.7A depicts the ELC setup. Here the ELC sample arm is connected to the humid flow control apparatus consisting of a humidity reservoir and vacuum pump. The
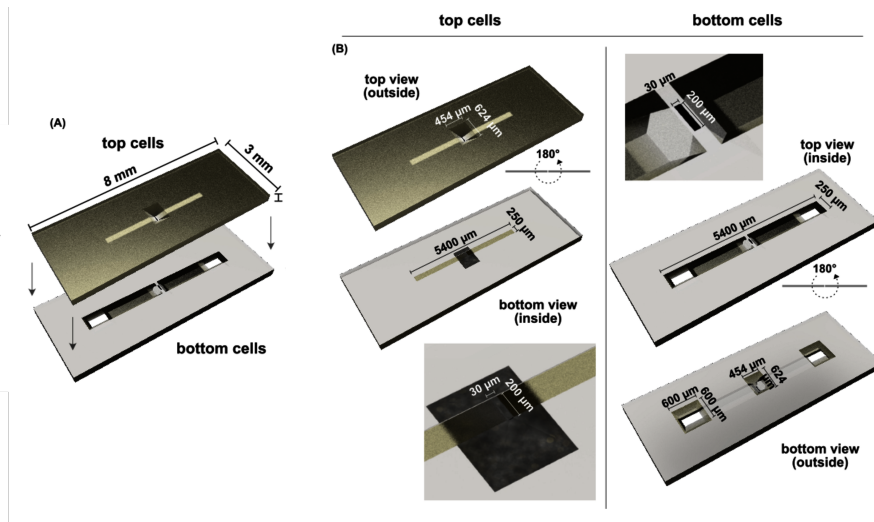
Figure 2.6: Environmental Liquid Cell Chips. A) Assembly of the top (static) and bottom (flow) liquid cell chips. B) The inner dimensions of the top and bottom chips. The viewing area for the electron microscope to pass through is 30 μm x 200 μm.
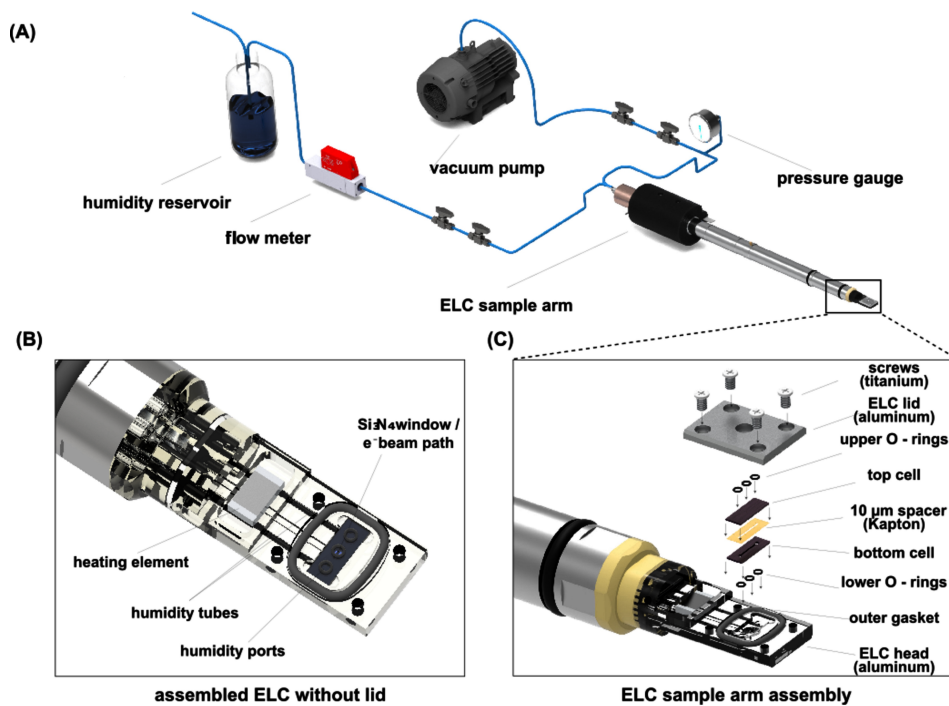
Figure 2.7: Environmental Liquid Cell setup. (A) Schematic of the ELC setup, which consists of a liquid cell specimen holder with an ELC inside. The inlet port of the holder is connected to a flowmeter and a humidity reservoir, while the outlet is connected to a vacuum pump. Two fine-tuning valves are connected on both sides to control the flow precisely, (B) Assembled ELC without lid showing heating element and humidity port and tubes. (C) An exploded view of the specimen holder with ELC.

aluminum headpiece of the ELC sample arm holds the 3 x 8 mm nanofluidic chip (Figure 2.6 and is equipped with a resistive heating element, two internally machined flow channels that act as inlet, and outlet humidity ports. A center port is where the Si_3N_4 window is positioned, and the electron beam passes. Two humidity tubes made from polyether ether ketone (PEEK) tubing (1/16 in. x 0.020 in.) run through the sample arm and connect to the humidity ports (Figure 2.7B). The temperature can be controlled from 4-100 °C with a connected water chiller, an essential requirement for many biological specimens. Fluoroelastomer (FPM) O-rings were placed on the three ports, and the surrounding periphery of the cavity wherein the chip assembly was mounted (8.5 x 0.8 mm). The aluminum lid has three grooves for FPM O-rings (0.97 x 0.33 mm) and four screw holes. The ELC assembled bottom was covered with the lid and secured with four titanium screws.

The bottom chips were glow-discharged (Balzers CTA 010, Balzers Union, Switzerland) for 30 seconds to render their surfaces hydrophilic, and the chips were then placed in the ELC sample arm (Figure 2.7C). The essential modification over the standard liquid cell assembly was the placement of a 10 μm thick Kapton-spacer between the silicon chips to allow airflow through the sample window area. Kapton-spacers were laser cut from 10 µm Kapton sheet into 3x 8 mm rectangles, with a 5.4x 0.5 mm cut-out in the center. The outer dimension and inner cut-out match the nanofluidic chip specifications. Laser cutting was conducted with a Protolaser U3 (LPKF, Hannover). The maximum power of the laser is 6 watts at a wavelength of 355 nm. After placing the Kapton-spacer on the bottom-chip, 0.5 μl of the sample was applied directly onto the Si_3N_4 window area with a pipette. Finally, the ELC was closed with a top-chip, all O-rings were aligned, and connections were sealed for vacuum compatibility (Figure 2.7C). On average, it took 10 minutes to assemble and align the ELC.

The humid flow control apparatus (Figure 2.7 A) produces a humid air stream in the ELC, engulfing the specimen and resulting in a liquid layer of a controllable thickness.[65] PEEK tubing connects the inlet port to a humidity reservoir and the outlet to a vacuum

pump. The pressure and humidity flow were observed with the connected vacuum gauge and a red-y smart meter GSM type (GSM-A9SA-BN00) flow meter. By adjusting the flow speed and pressure with the two fine-tuning valves, the liquid layer thickness on the bottom Si_3N_4-window was controlled via a combination of liquid displacement and condensation/evaporation effects. Typical operating pressures and flow speeds were in the 0.6-0.8 atm. and 0-5 ml/min range, respectively. Specimen solutions and reagents can be loaded either pre-assembly directly on the Si_3N_4-window or post-assembly via flow, thus opening the possibility of triggering in-situ reactions.

2.3.3 Hydration in the ELC with PNIPAM-BIS SiO$_2$@NGs

Core-shell nanoparticles are very interesting in biomedical applications, especially those involving inorganic nanoparticles in the core, as these can be used in various fields (e.g., sensing, diagnostics, drug delivery, etc.).[119] Silica nanoparticles are among the most studied inorganic nanoparticles as their synthesis and functionalization are well established, allowing the fabrication of particles with defined sizes, narrow polydispersity, and tailored material properties (e.g., porosity).[120] Recently, a poly(ethylene glycol) corona around silica nanoparticles was observed with LPEM.[121] The polymeric shell is of great importance for biomedical applications, as it can be used to either shield or increase the solubility/dispersibility of the inorganic nanoparticle. Moreover, depending on the employed polymer, more advanced features can be obtained. In some cases, the interplay between inorganic nanoparticles and polymers can be used as a trigger for the controlled release of therapeutics.[122, 123]

Herein, the controlled flow properties of the ELC are showcased with the hydration of PNIPAM NGs with a silica core (PNIPAM-BIS SiO$_2$@NGs). Time-lapse images were acquired at 0.35 ± 0.02 e$^-$/Å^2 per frame with an acquisition time of 100 ms. Following the first micrograph, water was injected, the airstream was used to thin it down, and a micrograph was recorded every two minutes (Figure 2.8). At 0 min, the dehydrated PNIPAM shell was collapsed around the periphery of the dark silica core. (Figure 2.8). After two minutes of hydration, the PNIPAM chains extended outward and were faintly

recognizable in the TEM micrographs. No major change was observed after four minutes.
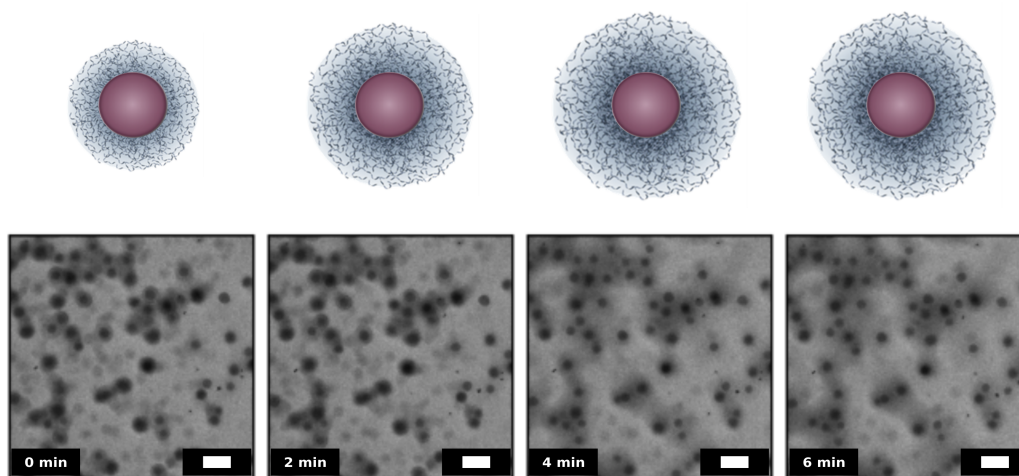
Figure 2.8: Swelling of PNIPAM-BIS SiO2@NGs, core-shell particles. Micrographs were recorded at a dose of 0.35 e$^-$/Å^2 and 2 minutes between each frame. At 0 minutes, the silica core was visible. The PNIPAM shell collapsed around the silica core. A core-shell appearance was present. After 2 minutes of hydrating the ELC, the PNIPAM chains were hydrated and extended outward from the silica core. The scale bar is 250 nm

Previous reports on the structure of PNIPAM-NGs reveal an inhomogeneous structure in which the crosslinking density is parabolically higher at the core than at the shell, giving a core-shell appearance.[114, 115, 124, 125, 126, 127] Considering this structure and the density of PNIPAM (1.149 g/cm^3) chains, it is realistic that we could not resolve the hairy outer structure of the NG. However, the PNIPAM-BIS SiO2@NGs serve as suitable proof for the hydration capabilities within the ELC.

2.3.4   Measurement of Window Thickness with Parallax

In order to cross-check the nominal thickness of the window fabricated by SimPore, parallax measurements were performed on the silicon nitride films. Here, the relative lateral shift of features at different heights is observed as a sample tilt function.[128] Due to the dimensions of the liquid cell holder, the degree of specimen rotation is limited to about 2°. Therefore, commercially available 3 mm format silicon nitride TEM grids with nominal thicknesses of 20 nm and 50 nm (SimPore; SIN100-A20Q33 and Pelco; 21508-10) were

examined in a Gatan 626 single tilt cryo transfer arm, operated at room temperature. The 20 nm silicon nitride films from SimPore are expected to be similar to the films of the custom-made ELC chips (Figure 2.6) since they have the same nominal thickness and are from the same manufacturer (SimPore).

Gold nanoparticles (Sigma Aldrich GmbH) of a nominal diameter of 10 nm were deposited on both sides of the silicon nitride films. They were then mounted into the holder and loaded into the JEOL JEM 2100 TEM. The eucentric height was determined by rotating the specimen and adjusting the z-position until such rotation resulted in minimal specimen motion, followed by focusing the image through adjustment of the objective lens current. Regions on the silicon nitride films containing AuNPs on either side of the film were selected, and micrographs at tilts of +20 $\pm$ 0.1° and -20 $\pm$ 0.1° were recorded at a magnification of 20.000. ImageJ was used for further analysis. The membrane thickness t was then determined via: [54, 60]

$$t = \frac{\Delta L}{sin\alpha} - 2r \tag{2.13}$$

where ΔL is the distance difference between a pair of particles (one on either side of the layer) corresponding to two images recorded at tilt angles of $+\alpha/2$ and $-\alpha/2$ (+20° and -20° in the present case). The distance between measured particle pairs is understood to be the distance component in the image plane in the direction normal to the sample rotation axis. The obtained thickness must be corrected by the term $2r$ as shown in Equation 2.13, assuming spherical particles of radius r are placed on the surface of the layer to be measured. Experimentally, r was determined by the average diameter of five particles in each region. Four regions with a minimum of four particle pairs were averaged for each window.

The calculated parallax thicknesses (Table 2.2) are in good agreement with the nominal thickness advertised by the manufacturer.

Table 2.2: Average Thickness as Determined by Parallax Measurements

Nominal thickness from manufacturer (nm)	Parallax average thickness (nm)
20 nm	19.66 ± 2.14
50 nm	40.34 ± 2.35

2.3.5 Thickness Characterization

Although parallax showed to be a suitable method for calculating the window thickness, with the setup, it is not applicable for liquid thickness. Therefore to determine the thickness of a layer (water or even silicon nitride) in place of Electron Energy Loss Spectroscopy (EELS), a previously published method tested in scanning TEM (STEM) was used here for TEM.[60, 129] The current of the transmitted electron beam passing the objective aperture was measured when the sample was in the beam (Int) and compared with the case of no sample in the beam (Int_{open}). Due to electron scattering, a fraction of the beam was scattered by angles larger than the opening angle of the objective aperture and thus not detected, thereby lowering Int. For the range of measured sample thicknesses, multiple scattering at this angular magnitude is negligible, so the following ratio applies:[6, 60]

$$\frac{Int}{Int_{open}} = exp\left\{\frac{-t}{L(\theta)}\right\} \tag{2.14}$$

where t is the thickness of the sample layer. The effective mean free path L (θ) for scattering to an angle of θ or greater is given by:

$$L(\theta) = \frac{W}{\sigma(\theta)\rho N_A} \tag{2.15}$$

Here ρ and W are the sample layer's density and atomic weights, and N_A is the Avogadro's number. The cross-section ($\sigma(\theta)$) for scattering to an angle of θ or greater is the sum of inelastic and elastic contributions, which for Si_3N_4 are given by:[6, 130]

$$\sigma_{SiN,el} = (1 + E/E_o)^2(3/7f_N^2 + 4/7f_{Si}^2) \tag{2.16}$$

$$\sigma_{SiN,inel} = \frac{4(1 + E?E_o)^2}{a_H^2(Q^2 + Q_0^2)^2}(3/7S_N + 4/7S_{Si}) \tag{2.17}$$

where $a_H = 0.529 \times 10^{-10}$ m (Bohr radius), $\lambda = 2.51 \times 10^{-12}$ m (electron wavelength at 200 keV), $E_0 = 511$ keV (electron rest mass-energy), E = 200 keV (accelerating voltage of the TEM used). Elastic and inelastic scattering factors for nitrogen and silicon are denoted by f_N, S_N, f_{Si}, and S_{si}, respectively, and were taken from the literature.[130, 131, 132] The momentum transfer Q = $2\pi\sigma/\lambda$ is determined by the characteristic value

$$Q_E = \frac{2/\pi}{\lambda} \frac{13.5Z}{2E} \frac{E + E_0}{E + 2E_0} \tag{2.18}$$

where Z = 10.6 (the effective atomic number for Si_3N_4). Note that the scattering cross-sections and the mean free path are dependent on the collection semi-angle θ and the electron energy. The collection semi-angle of the objective aperture used in the present study is given by $\theta = 12.6$ mrad as determined by directly imaging the objective aperture in diffraction mode. The detector camera length was calibrated using diffraction rings from a polycrystalline aluminum film. The scattering cross-section in the case of water was directly taken from Wang *et al.*[130] The scattering cross-section and mean free path (MFP) of Si_3N_4 and water showing total ($\theta = 0$) and effective ($\theta = 12.6$ mrad) elastic and inelastic scattering are shown in Table 2.3.

Table 2.3: Elastic and Inelastic Scattering Cross-sections

Collection Semi-angle (mrad)	$\sigma_{SiN,el}$	$\sigma_{SiN,inel}$ (x 10^{-5} nm^2)	$\sigma_{water,el}$	$\sigma_{water,inel}$	Total MFP Si_3N_4 (nm)	Total MFP Water (nm)
0	10.9	15.1	6.7	13.0	40	152
12.6	4.71	0.79	3.3	0.91	190	718

The transmission intensity ratio Int/Int_0 is experimentally well approximated (in case of layer thicknesses less than the mean free path) by measuring the ratio of the total

integrated intensity of images recorded with (Int) and without (Int_0) the objective lens aperture in place. This method is preferable to Int/Int_{open} (Equation 2.14) that compares; with the objective aperture in place, the intensities of images with (Int) and without a sample (Int_{open}) in the beam path. Measuring Int/Int_{open} in an assembled LC would generally require the ability to temporarily withdraw the specimen from the beam path or a highly stable beam whose intensity could be calibrated before each measurement run. Neither of these requirements are met in the current system, as typically the measured beam intensity drifts are 8% per half hour. Therefore, the pairs of images were recorded within a short period of time (less than 10 seconds) to minimize the effect of electron beam intensity drift and fluctuations.

To account for the finite number of electrons scattered beyond the objective lens acceptance angle; which results in a small difference between the actual (no sample in the beam path, Int_{open}) and measured (no objective aperture in the beam path) value of Int_0, a comparison between the transmission intensity at 10 different regions on intact windows with and without an objective aperture inserted were measured (Int_{avg}). Additionally, rapid translation from intact (Si_3N_4 covered) regions to broke/open areas (about 10 seconds) occurred (Int_{open}). The average transmission ratio (Int/Int_{avg}) was divided by the open/true ratio (Int/Int_{open}) to get the adjusted ratio (Int/Int_0). The values for the respective transmission intensity ratios are shown in Table 2.4.

Table 2.4: Transmission Intensity Ratios

Nominal Thickness (nm)	Average Ratio (Int/Int_{avg})	Open Ratio (Int/Int_{open})	Adjusted Ratio (Int/Int_0)
20	0.918 ± 0.001	0.997 ± 0.002	0.921 ± 0.001
50	0.831 ± 0.001	0.986 ± 0.001	0.842 ± 0.001

Particularly in the case of thin layers, the effect between the Int/Int_{avg} and Int/Int_{open} is small. The adjusted ratios (Int/Int_0) were applied to the Reimer and Wentzel models. The Wentzel Atomic model approximates the potential with a single exponential function.

The Reimer molecular model uses the published scattering factors from Wang, which were calculated using configuration interaction wavefunctions.[6, 130, 131, 133] The following parameters were set for the thickness calculation: beam energy 200 keV; Si_3N_4 density =3200 kg/m^3; atomic weight= 0.02 kg/mol; effective atomic number= 10.6; objective aperture= 12.6 mrad. The results and comparison to the parallax values are shown in Table 2.5.

Table 2.5: Si_3N_4 Thicknesses Based on the Reimer and Atomic Models

Nominal (nm)	Parallax (nm)	Intensity Ratio (Int/Int$_0$)	Reimer (nm)	Atomic (nm)
20 nm	19.66 ± 2.14	0.920 ± 0.001	12.6	15.6
50 nm	40.34 ± 2.35	0.840 ± 0.001	26.4	32.6

The transmission intensity ratio method based on the Reimer model deviates from the parallax thickness measurement by 36%, whereas it is 21% in the case of the Atomic model.[7, 128, 134] Since the log intensity ratio method employed here relies on several assumptions regarding material parameters and electron scattering models, a significant difference in the thus determined thickness to the actual geometric thickness is to be expected. Other authors have also found such differences.[60, 129, 134]

2.3.6   Computed Thickness from a Monte Carlo Simulation

Monte Carlo simulations were run of electron propagation through the liquid cell geometry in CASINO 3.3, with cross-sections calculated using ELSEPA.[135, 136] These simulations act as another way to relate the found effective transmissivity Int/Int_0 to a water layer thickness (Section 2.3.5). A 10% error of raw simulation results is assumed in the computation of all specified outcomes due to uncertainty of the aperture angle and the physical scattering model, as well as stochastic noise and tolerances of the window thickness. For further processing, the simulation results were loaded into a Python-based Jupyter notebook, where curve-fitting to obtain effective mean free paths (equation 2.14)

interpolated for arbitrary window and water thicknesses, and error propagation for the final values is performed.

The obtained values for effective mean free paths of electrons in the windows l_0 and the water L_0 are significantly larger than the physical mean free paths for electron scattering within the respective medium. This is due to multiple scattering that becomes prevalent at large layer thicknesses and leads to electrons being scattered back into angles below the aperture cutoff. For the same reason, a small positive dependence of the effective mean free path inside the water L_0 on the window thickness $t(l)$ is found, which is well described by an empirical relation shown below (Figure 2.9). The transmission ratio as a function of water thickness L for a given window thickness $t(l)$ can be described by an effective Lambert-Beer law with high accuracy:

$$Int/Int_0 = \cdot exp\left(-t(l)/L_0(l)\right) \tag{2.19}$$

$$t(l) = exp\left(-2l/l_0\right) \tag{2.20}$$

$$L_0(l) = L_0^{(0)}(1 + (l/l_0')^2)^{1/2} \tag{2.21}$$

where $t(l) = 0.895$ accounts for scattering inside the pair of 12.0 nm thick windows, and L_0=869$\pm$ 11 nm, l_0=216 $\pm$ 4 nm, l_0'=155$\pm$ 59 nm determined from a least-squares fit over all the simulated transmittance data.

Figure 2.9 shows the effective transmission ratio (Int/Int$_0$) versus the liquid layer thickness, determined from Monte Carlo simulation results. Shaded areas indicate $\pm$ 3σ ranges of the fit result.

The validity of this simulation was cross-checked by computing the transmission ratio through silicon nitride membranes (using the nominal thickness) and inferring from that a computed transmission thickness. These values were compared to the measured values and are presented in Table 2.6. Overall, there is excellent agreement between computed
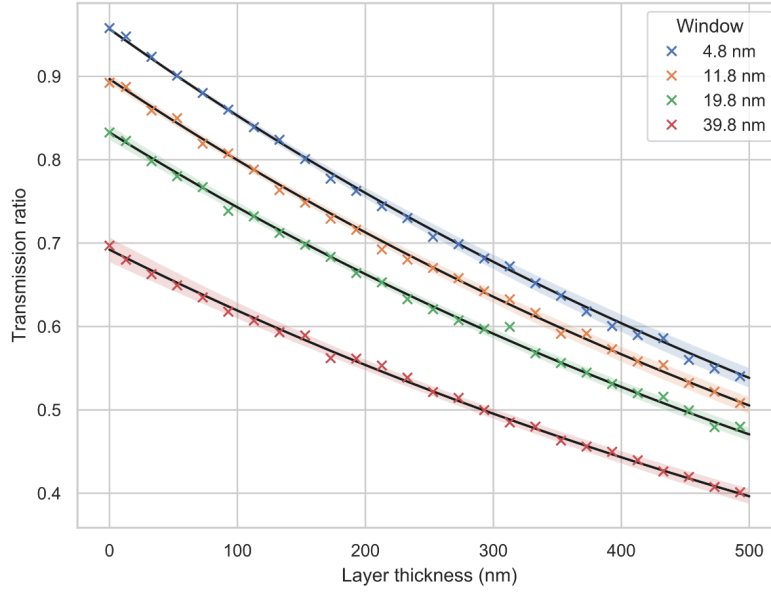
Figure 2.9: Transmission ratio (Int / Int_0) as a function of water layer thickness t for varying window thicknesses

and experimentally determined values. Therefore based on the assumption that the Monte

Carlo simulation is correct, this method is considered to be a way to estimate the thickness.

Table 2.6: Measured and Computed Window Thicknesses and Transmission Ratios

| | Method | Nominal Window | |
		20 nm	50 nm
Measured	Transmission Ratio (Int/Int_0)	0.920 ± 0.001	0.840 ± 0.001
	Reimer Model (nm)	12.6	26.4
	Atomic Model (nm)	15.6	32.6
	Parallax (nm)	19.66 ± 2.14	40.34 ± 2.35
Monte Carlo Simulation	Computed Thickness (nm)	18.5 ± 0.4	40.0 ± 0.8
	Computed Transmission Ratio (Int/Int_0)	0.91 ± 0.01	0.83 ± 0.01

The computed transmission is inferred from the measured thickness, and vice versa

2.3.7 Control of Spatial Resolution and Liquid Layer Thickness with the ELC

Gold nanoparticles (AuNPs) can easily withstand 1000 $e^-/Å^2$.[25, 31] Therefore AuNPs

(10 nm diameter) were selected as a benchmark for investigating the spatial resolution

with respect to the water layer thickness and suitability of the ELC. A total dose of 5 $\pm$ 0.4 e$^-$/Å^2 was used with an exposure time of 2 seconds. Additionally, to demonstrate that the signal to noise is a function of electron dose, the experiment was repeated with a higher total electron dose of 27 $\pm$ 2 e$^-$/Å^2 with 2 s exposure time. The error in the electron dose value was calculated from the standard deviation of measured electron doses over 40 minutes.

The liquid layer thickness was calculated using equation (2.14), with the mean free path of water for scattering to an angle θ = 12.6 mrad or greater taken as 718 nm according to Table 2.3. Additionally, transmission intensities (Int/Int$_0$) were used with the Monte Carlo Simulation (Section 2.3.6, Figure 2.9) to get the computed liquid thickness. Before adjusting the liquid layer, the intensity ratio of the AuNP solution was 0.62. Setting the flow rate to 1 ml/min and the pressure to 400 mbar resulted in an intensity ratio of 0.79.

The resolution parameter was obtained by measuring the intensity distribution across the edge of the particle (AuNP), and the width x 0.5 between the points at which the step reaches 0.25 and 0.75 of its total intensity; therefore, the edge width of the AuNPs was used to characterize the dependence of image resolution on the liquid layer thickness.[6, 17, 65]

Assuming the AuNPs exhibit a perfectly sharp boundary and the images are taken in-focus, the average edge width of six selected AuNPs was calculated from an error function fit of the respective line profiles generated by averaging the signal over a width of 3 pixels. The assumed error function has the form erf$((x-\mu)/(\sigma\sqrt{2}))$, where μ is the position of the edge and σ is the width in the measurement. The standard deviation in the mean value is shown as the error in the resolution estimation. Representative micrographs and line profiles of AuNPs are shown in Figure 2.10 (A, B). Whereas Table 2.7 contains the thickness values calculated from equation 2.14 and the Monte Carlo Simulation (Section 2.3.6).

The thickness results in Table 2.7 show good agreement between the two methods. For both cases, A to B and C to D, the thinning of the liquid resulted in a decrease of edge with resolution. Additionally, these results exemplify the influence dose has on resolution,
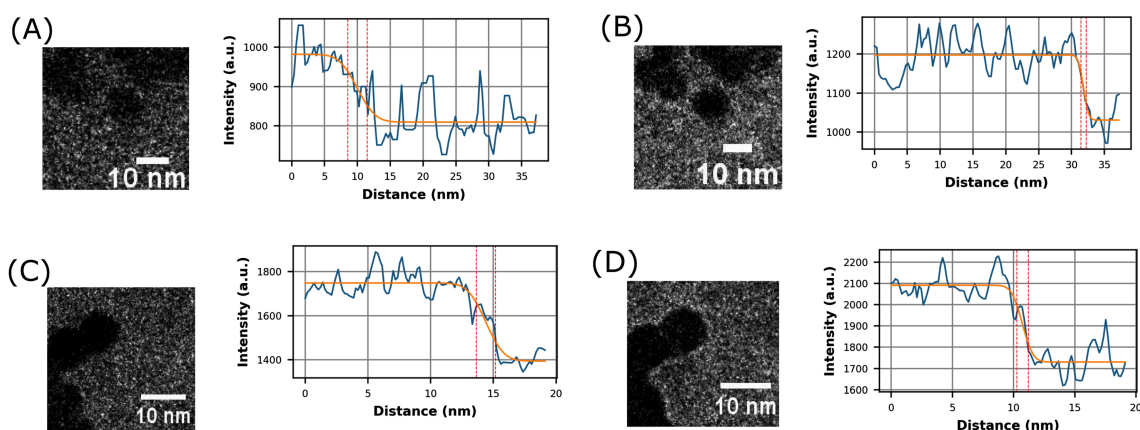
Figure 2.10: AuNPs at two different electron doses and with different liquid thicknesses. Water layer thickness optimization at two thicknesses. The water layer was thinned from 340 ± 71 nm (A) to 160 ± 34 nm (B) via the control of the vacuum and humid air source, and in a similar experiment with a higher electron dose, was thinned from 240 ± 50 nm (C) to 160 ± 34 nm (D). The micrographs show a representative AuNP and a line profile (blue line) across the AuNP shown in the micrograph with an error function fit (orange line). 6 AuNPs are averaged, and the error in the resolution is determined from the standard deviation of the mean value of 25-75% edge width resolution of these 6 AuNPs. The thinning of the liquid layer (A to B) improves the resolution from 1.7 ± 0.8 nm to 0.8 ± 006 nm, and from 0.9 ± 0.5 nm to 0.7 ± 0.2 nm (C to D), respectively.

Table 2.7: Comparison of Liquid Thickness and Edge Width Resolution from AuNP in Figure 2.10

AuNP Region	Dose $(e^-/\text{Å}^2)$	Calculated[1] (nm)	Computed[2] (nm)	Edge Width Resolution (nm)
A	5 ± 0.4	340 ± 71	315 ± 16	1.7 ± 0.8
B	5 ± 0.4	160 ± 34	107 ± 16	0.8 ± 0.01
C	27 ± 2	240 ± 50	202 ± 11	0.9 ± 0.5
D	27 ± 2	160 ± 34	103 ± 11	0.7 ± 0.2

1: Thickness calculated from Equation 2.14
2: Thickness computed from the Monte Carlo Simulation

with the higher dose (C and D) exhibiting a lower edge with resolution.

2.3.8   Beam Induced Degradation of Nanogels in the ELC

Beam induced effects are rampant within LPEM. This is due to the radiolysis of water into hydrated electrons (e^-_{aq}), hydrogen radicals ($H^·$), hydroxyl radicals ($OH^·$), and hydrogen gas (H_2).[137] This section uses poly(N-isopropylacrylamide) (PNIPAM) nanogels

(NGs) to introduce the topic of beam sensitivity of low-contrast specimens in the hydrated ELC. Radiolysis is presented in more detail in Section 3.

PNIPAM NGs are soft colloidal particles often used for drug delivery applications.[138, 139] The softness, degree of swelling, and optical properties are tailored by the chemical structure and crosslinking density.[114] To this end, I investigated the influence of irradiation dose on the chain scission of the PNIPAM polymers. An image series was acquired with an acquisition time of 200 ms and a dose of 0.70 ± 0.06 e$^-$/Å^2 per frame (Figure 2.11). No movement or aggregation of the NGs was observed during image acquisition, owing to the fact that the NGs are positioned on the hydrophilic bottom chip. However, a clear decay in the NGs' total signal with an increasing cumulative dose is observed (Figure 2.11).
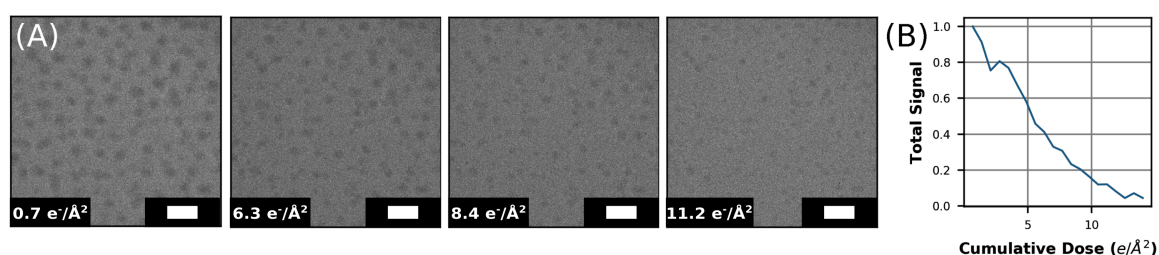
Figure 2.11: PNIPAM NGs in the ELC with increasing cumulative dose. (a) Micrographs of PNIPAM NGs in the ELC, recorded at 0.70 e$^-$/Å^2 to observe beam-induced radiolysis of the NGs. The NGs gradually fade with increasing cumulative dose. Scale bar 250 nm (b) Total signal normalized to one. The total signal decayed by 10% per unit of dose, and following a cumulative dose of 5.4 e$^-$/Å^2 half of the signal was lost.

The images display a 7% drop in the total signal, which is a comparative measure of image quality and defined as the sum of the signal to noise, as introduced in Section 2.3.1.4 with Equation 2.10. The total signal drops to half in successive frames and after a cumulative dose of 5.4 e$^-$/Å^2. The observation of the fading, etching, and dissolution of particles in liquid-phase EM has been described as the result of beam-induced radiolysis.[140, 141] The dissolution of the particles was not considered in these previous liquid cell experiments as they reported negligible electron-induced heating, and the imaging temperature (20°C) was below both the lower critical solution temperature (33 °C) and

glass transition temperature of PNIPAM NGs. [111, 142, 143]

2.3.9 Summary

Within this section, a standard liquid flow cell setup was modified into an ELC via the addition of a 10-μm-thick Kapton-spacer, a humid flow control apparatus, and decreased window dimensions. With standard LPEM techniques, the bulging of the silicon nitride window limits the viewing area for high resolution to regions close to the edges. Though to a lesser degree, this is also true for pressure-controlled setups that flatten the window to make the entire window available for imaging; however, this prevents the flow of liquids.[65] In the ELC, bulging is irrelevant since a liquid film of constant thickness forms and follows the contours of the bulging windows, thereby freeing up the entire available window area for potential high-resolution imaging. Adjusting the z-position of the specimen holder and focusing on the thin liquid layer at the bottom ensures improved resolution. The ELC enabled in-liquid imaging of varying mass-thickness samples at total doses not exceeding 30 e$^-$/Å^2.

The Si$_3$N$_4$ window thickness was calculated by parallax and from the transmission intensity with the Reimer and Atomic Models. The spatial resolution improved with the decreasing liquid layer calculated from the transmission intensity. A Monte Carlo simulation was performed to corroborate the measured and calculated window and liquid thicknesses. The computed window thicknesses from the simulation were comparable to the parallax values and closer to the nominal window. From the simulation, the computed thicknesses were comparable to the parallax values and closer to the nominal window thickness than the Reimer and Atomic models.

This ability to image structural dynamics on hundreds of ms timescales and longer, within electron dose limits, is complemented by the ability of the ELC to flow in and exchange reagents to trigger structural dynamics, or biological processes, as demonstrated via the in situ hydration of PNIPAM NGs with a silica core. These results are in themselves an improvement over previously reported environmental cell designs. Additionally, the PNIPAM NG results introduced beam induced damage and highlighted the importance of

having a chemically simple sample to investigate the damage. Finally, the results introduced beam induced damage within the ELC. The direct mechanism by which the PNIPAM NGs fade is complex. Therefore in the subsequent sections and chapters, the growth of gold nanoparticles (AuNP) is used as a probe for radiolysis and a hydrated environment.

2.4 Universal (3 mm) and Confined Micro-wells Liquid Cells

2.4.1 Universal 3 mm Liquid Cells

Although the ELC allows for a controlled and tailored liquid layer thickness, it requires an expensive setup that includes a microscope specific holder and LC chips. To circumvent this and ensure LPEM is accessible to more research laboratories, I prepared LCs with 3 mm TEM grids. Within the LC community, 3 mm TEM grids are used predominantly with graphene coated grids. These LCs have offered an improved resolution, contrast, and it is theorized reduced electron beam-induced damage. [10, 18, 19, 20, 24] The preparation of graphene LCs is quite tedious; therefore, I selected commercially available carbon TEM grids (S160 mesh 400 TEM grids from PLANO) due to their growing interest within the LC community.[35, 93]

Polyvinyl formal (Formvar), $\left[C_3H_6O_2 \right]_n$ is a polymeric film used within the TEM community as a stabilizing support for carbon coated TEM grids.[144] This is partly due to its ability to withstand preparation procedures (e.g., negative staining), resistance to electron beam irradiation, thin (allowing electrons to pass through), and homogeneous smoothness.[145] However, besides the publication from Ren *et al.* in 2020 in which they used a Formvar sandwich to observe irradiated NaCl crystals, formvar as a window material for LCs have not been explored.[146] Therefore this section aims to test the feasibility of LCs composed of formvar and carbon windows.

2.4.2 Experimental Preparation of Formvar Films

Formvar films for TEM applications are prepared from a mixture of formvar and a volatile solvent (e.g., chloroform, 1,2-dichloroethane (DCE)). As a homogeneous film is required for LC assembly, the concentration of formvar in the DCE solution was varied

from 0.1 % to 1 %. The standard method to prepare the films is by dipping a glass slide into a formvar + solvent solution, drawing it out, and drying it at room temperature. Once dried (∼ 6 hours), the edges are scorned with a razor blade, and the slide is dipped into a glass beaker. The formvar film floats on the water surface, and the TEM grids are placed onto it. Filter paper (Whatmann 90 mm) is used for fishing the TEM grids from the liquid. The formvar coated grids on filter paper are allowed to dry at room temperature.[145] As mentioned by Davison *et al.*, removing the film from the glass slide was difficult, and possible contamination of the glass slide resulted in defects in the film.[145]

Therefore, I based the formvar TEM grid preparation on the drop method as described by Both *et al.* and Davison *et al.* [145, 147] Herein 1) drop of 0.1%, 0.3%, or 1% solution of formvar dissolved in DCE ($C_2Cl_2H_4$) was drop-cast onto the water in a glass dish (diameter 9 cm) using a glass pipette. The formvar solution spread on top of the water surface. The film is easily observed by the interference (almost opalescent) colors of the evaporating solvent. For the drop method, DCE is preferred over chloroform (CCl_3H) as the evaporation rate is too rapid, and the drop cannot spread over the water surface.[147] 2) Glow discharged, 400 mesh TEM copper grids (purchased from Plano GmbH) were placed on top of the floating formvar film. 3) To remove the TEM grids, the back-side of the floating TEM grids were touched with a piece of Parafilm cut to the dimensions of the floating grids. As the Parafilm clings to the formvar grids, all grids can be easily removed. The grids were left to dry for 30 minutes before subsequent use.[145]

Next, the average film thickness was calculated from the transmission intensity ratio (Int/Int_0) as introduced in Section 2.3.5 with Equation 2.14. Here, the thickness is based on water's scattering properties (Table 2.3). Parallax was not used, although it could have been employed to calculate the film thicknesses. The average intensity ratio and corresponding thicknesses in Table 2.8 are from 5 regions.

Although the 0.1% formvar in DCE resulted in the thinnest film, it was not homogeneous. Therefore a 0.3 % formvar, DCE solution was used for subsequent formvar LC assemblies.

Table 2.8: Film Thickness

Formvar in DCE (%)	Intensity Ratio (I/I_0)	Thickness (nm)
1	0.960	29 ± 5
0.3	0.963	27 ± 2
0.1	0.972	20 ± 4

2.4.3 Liquid Cell Fabrication

A 20 mM solution of chloroauric acid in water was used as the test sample for formvar and carbon LCs to ensure the LC was not dry. $HAuCl_4$ reduces down and forms gold nanoparticles in the presence of the electron beam. Therefore, successful LC assemblies should exhibit AuNP growth or reduction.[3, 25, 30, 148, 149, 150] The fundamentals of the reduction of $HAuCl_4$ and particle nucleation are discussed in Section 3.2.3. Here, a 0.3 μl drop of the 20 mM $HAuCl_4$ solution was dropped onto a glow discharged TEM grid, and another grid was placed on top to create an assembled LC. Figure 2.12 depicts representative micrographs from a successful formvar LC assembly with the $HAuCl_4$ solution.

In Figure 2.12, the top row (a-c) showcases overview images of the assembled LC, and the bottom row (d-f) zoomed-in regions highlight hydrated regions and small AuNPs. Similar results of small pockets of liquid were also observed for carbon LCs. Equation 2.14 was used to calculate the average liquid layer of 3 regions containing AuNPs. Liquid layers of 190 nm ±11 and 187 nm ± 8 were found for formvar and carbon LC assemblies. Representation of 3 mm LCs is often presented as aligned grid bars and multiple liquid pockets, as sketched in Figure 2.13.

In reality (c), the grid bars do not align, and there are few liquid pockets. There are small liquid pockets and many dry regions between two grid bars (d). Nonetheless, I have demonstrated that the formvar and carbon 3 mm TEM grids are suitable LC windows within this section. However, the in-homogeneous liquid thicknesses and sporadic liquid pockets make a detailed investigation of samples with this type of LC assembly difficult
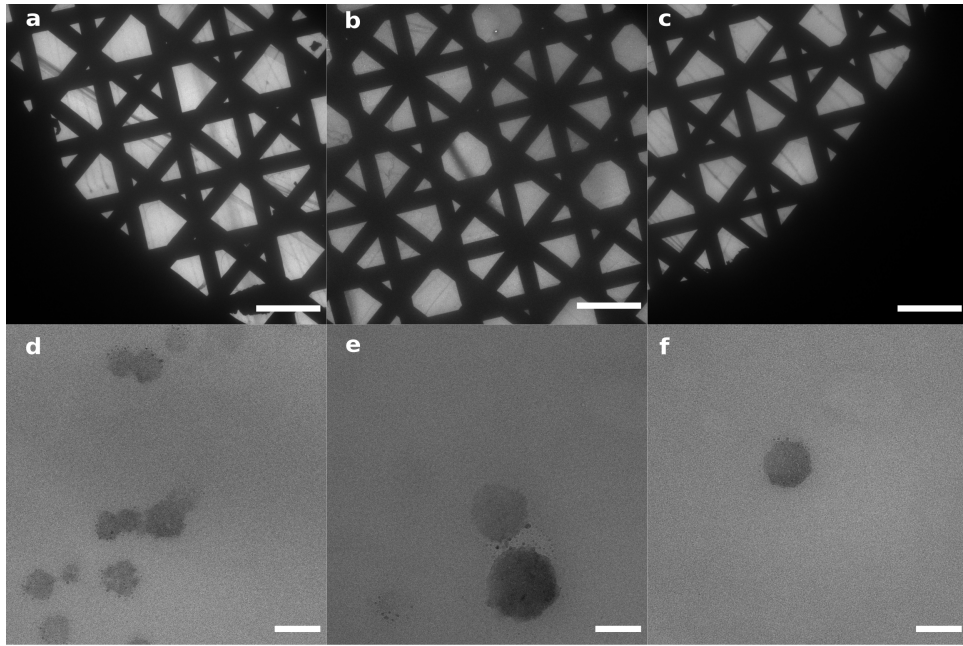
Figure 2.12: Representative micrographs from a formvar LC assembly with HAuCl$_4$ solution. a-c low magnification overview images with a scale bar of 100 μm, d-f higher magnification images with scale bars of 100 nm.
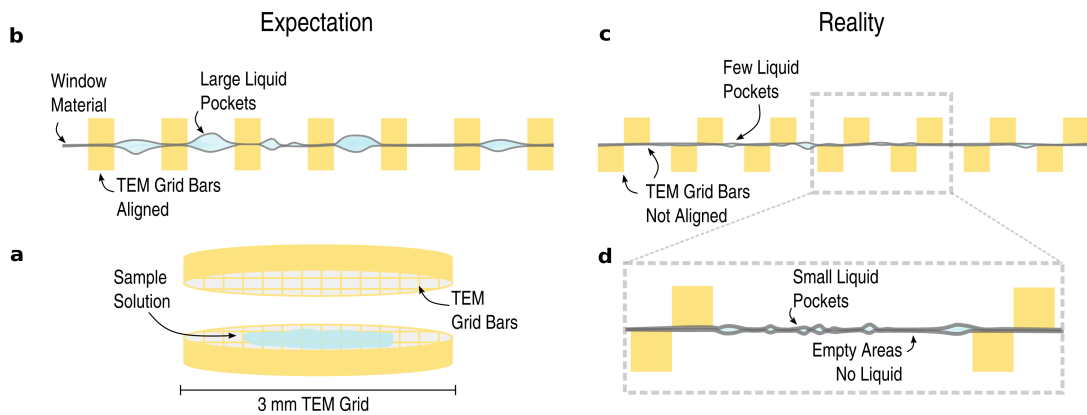
Figure 2.13: Schematic of 3 mm TEM grid LCs (a), (b) what is expected with assembled LCs vs. what is really achieved (c) with a zoomed-in region on (d).

and not reproducible. Therefore, the next sections build upon the formvar and carbon 3 mm TEM grids presented here and investigates the incorporation of confined micro-wells via nano-fabrication of elliptical windows and anodic aluminum oxide (AAO) films to circumvent these issues.

2.5 Confined Micro-well Liquid Cells

2.5.1 Elliptical Multi-windows

As introduced in the thesis of Dr.Sana Azim, elliptical multi-window chips were fabricated by an external company to decrease the window bulging and ensure a controlled liquid layer.[24] The design consisted of multiple elliptical Si_3N_4 windows 10 nm in thickness and varying dimensions. The idea was for the top and bottom windows to result in overlapping ellipses, decreasing the window bulging.[151] Representative images of the received chips from the external supplier are shown in Figure 2.14.
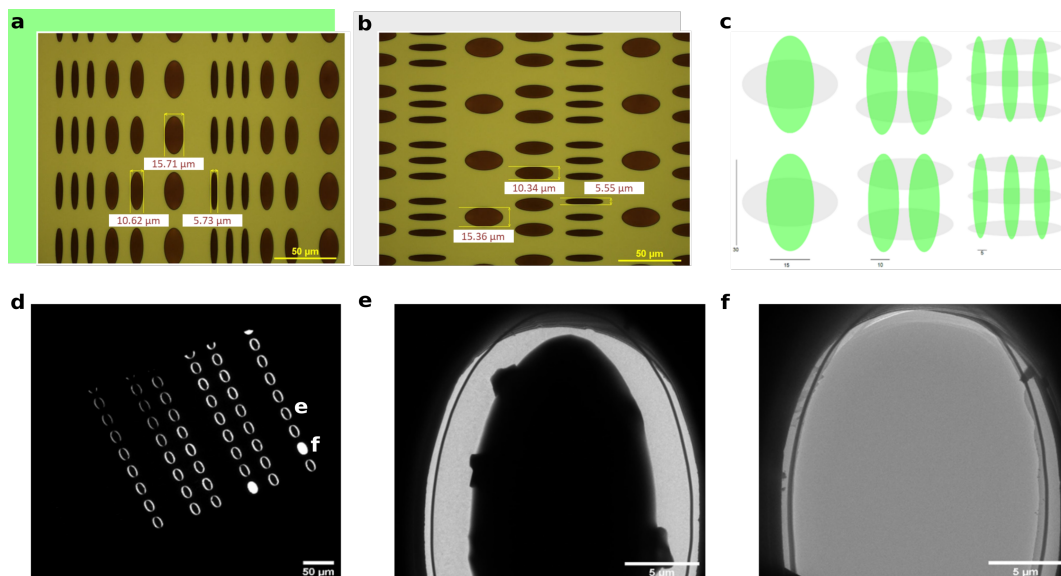
Figure 2.14: The fabricated multiwell chips. a & b) Optical microscope images of the top and bottom chips, c) schematic showing the overlap of the top (green ellipses) with bottom (gray ellipses) chips, d) TEM micrograph of one multiwell chip, e & f) zoomed-in regions showcasing filled in well and well with no window material, e and f respectively.

(a) and (b) are the top and bottom LC chips with rotated elliptical windows, and (c) is a schematic showing how the top (a, green ellipses) and bottom (b, gray ellipses) windows would overlap in an assembled liquid cell. However, upon investigation in the TEM (d-f), it became apparent the 10 nm Si_3N_4 windows were either filled with debris (e) or broken (f), whereby making these LCs unusable.

Therefore I looked for an alternative to circumvent the difficult nano-fabrication steps required for Si_3N_4 multiwindows.

2.5.2   Experimental Preparation of AAO Liquid Cells

Recently, Lim *et al.* introduced the use of anodic aluminum oxide (AAO) between films of graphene as a way to prepare ordered nano-chamber LCs with specific spacer height.[152] Similar to others who have fabricated graphene LCs, they transfer graphene to holey carbon TEM grids.[140, 152] Holey carbon TEM grids consist of a holey carbon film on a metal TEM grid. Routinely these are used to improve the stability of the thin film. Only the aligned holes covered with graphene result in assembled LCs. Whereby assemblies with these grids result in a decreased imaging area. Additionally, coating TEM grids with graphene is expensive from a time and financial perspective. Therefore, to create a universal multiwell liquid cell that is easy to fabricate and inexpensive, I investigated using the formvar TEM grids prepared in Section 2.4.1 and commercial carbon TEM grids as window support structures. Furthermore, as Si_3N_4 is a standard within the liquid cell community, I included it as an additional window material for AAO LCs.

2.5.2.1   Fabrication of AAO Windows

The AAO liquid cell fabrication was based on Lim *et al.*[152] The steps are shown in Figure 2.15.

1) A square sheet of AAO from the as-provided 15 x 15 mm membrane, cut with a razor blade on a glass slide with the AAO side up and poly(methyl methacrylate) (PMMA) side facing down. The sheet has inter-pore distances of 125 nm, pore diameters between 70-90 nm, and a thickness of 130 nm (UT125-079-130, from top membranes technology). 2) A 0.3 μl drop of ddH_2O was placed on the center of the 3 mm TEM grid (formvar or carbon coated S160 mesh 400 TEM grids from PLANO, introduced in section 2.4.1). 3) The grid touched the AAO sheet, leaving the PMMA on top. The liquid was allowed to evaporate. 4) The grid was flipped upside down and placed in a custom TEM grid holder that accommodates 12 grids (Figure 2.15 c). 5) This holder was placed in a glass
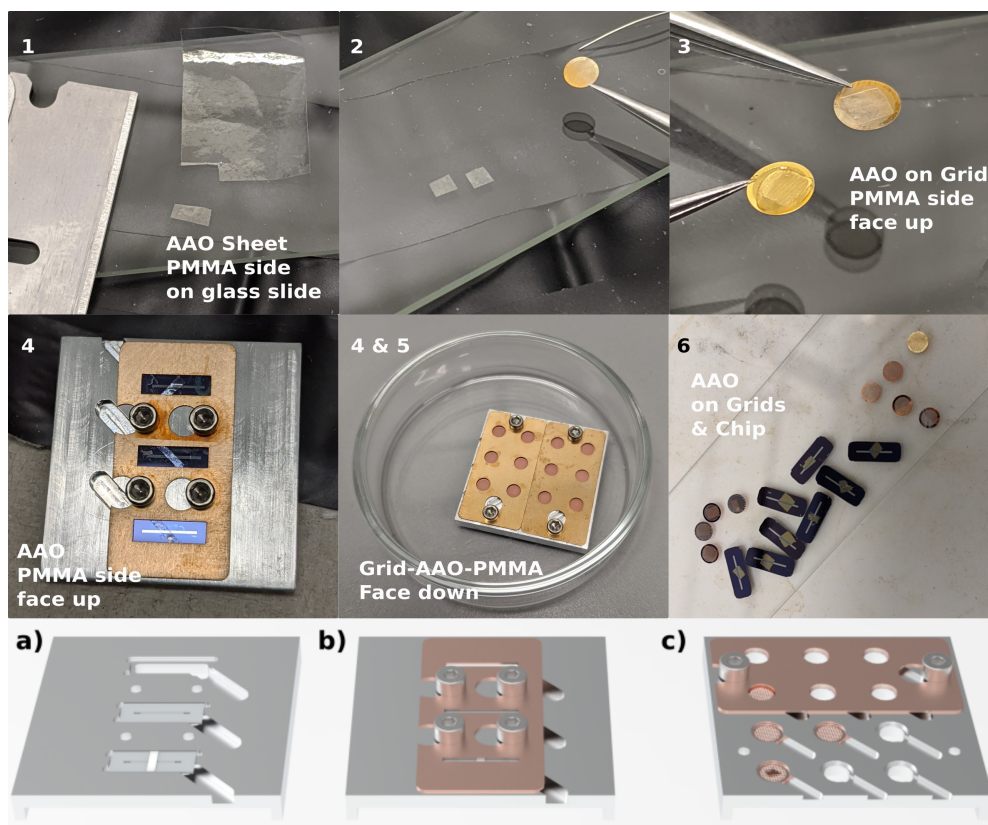
Figure 2.15: Steps for AAO fabrication on 3 mm TEM grids and 3 x 8 mm Si_3N_4 LC chips. 1) Cutting of AAO (PMMA side touching glass slide), 2) drop of ddH_2O placed on grid, 3) touch grid to AAO sheet, so PMMA side is face-up, 4) flip upside down and place in the holder, 5) placed in petri-dish with acetone, 6) dried TEM grids and Si_3N_4 LC chips with transferred AAO. Holder used for fabricating Si_3N_4, formvar and carbon AAO windows. a) holder with Si_3N_4 chip containing AAO face side up, b) holder with lid, c) holder for standard 3 mm TEM grids with AAO face side down.

petri-dish. Acetone (Sigma Aldrich) was added to dissolve the PMMA. The acetone was replaced two times over four hours. 6) After the acetone wash to remove the PMMA, the grids were left to dry at room temperature.

With the 3 x 8 mm Si_3N_4 static LC chips introduced in Section 2.3 with the ELC, a similar procedure was followed, except the nitride chips were glow discharged for 30 seconds prior to step 2. To account for the increased hydrophilicity and liquid spreading, 0.5 μl drop of ddH_2O was placed on the center of the nitride chip (step 2). The chip was placed face-side up in a custom liquid cell chip holder (Figure 2.15 a). The top clamp acted to secure the AAO to the nitride chip (Figure 2.15b).

The liquid cell chip and grid holder in Figure 2.15 improved the reproducibility between

runs as the original procedure presented by Lim *et al.* requires tweezers to hold the TEM grids in the acetone.[152] Regardless of the window material, with the use of these holders, the transfer of AAO to window material had an 80% success rate.

2.5.2.2 Calculation of Liquid Thickness for AAO Liquid Cells

In the case of the assembled AAO liquid cell, the original intensity ratio (Equation 2.14) method applicable for large area homogeneous samples does not apply since large-angle scattered electrons would add a significant background, altering the signal. A two aperture approach was introduced to mitigate this effect wherein the intensity ratio of two images was recorded. Basing off of Equation 2.14

$$\frac{Int_1}{Int_0} = exp(-t/\ell_1) \tag{2.22}$$

and introducing

$$\frac{Int_2}{Int_0} = exp(-t/\ell_2) \tag{2.23}$$

where ℓ_2 and ℓ_1 are the mean free path of electron scattering to angles beyond 8.75 mrad (522 nm) and 12.6 mrad (718 nm) in water, respectively, Int_2 and Int_1 are the mean intensity for the ℓ_2 and ℓ_1 images, and Int_0 is the mean intensity with no aperture. Therefore

$$r_{total} = \left(\frac{Int_1}{Int_2}\right)_{total} = \frac{exp(-t/\ell_1)}{exp(-t/\ell_2)} \tag{2.24}$$

or

$$r_{total} = exp\left(-t\left(\frac{1}{\ell_1} - \frac{1}{\ell_2}\right)\right) \tag{2.25}$$

and

$$\ln r_{total} = t_{total}\left(\frac{1}{\ell_2} - \frac{1}{\ell_1}\right) \tag{2.26}$$

the two different objective apertures are compared, allowing for an intensity ratio map with a sub-frame resolution to be constructed. The total thickness formula for this case becomes

$$t_{total} = \frac{ln\left(r_{total}\right)}{(1/\ell_2) - (1/\ell_1)} \tag{2.27}$$

To subtract the window thickness, r_{win} was introduced:

$$r_{win} = \left(\frac{Int_1}{Int_2}\right)_{window} \tag{2.28}$$

which takes the average, Int_1/Int_2 intensities for two windows.

Therefore

$$r_{win} = exp\left(t_{win}\left(\frac{1}{l_2} - \frac{1}{l_1}\right)_{win}\right) \tag{2.29}$$

and

$$r_{liquid} = exp\left(t_{liquid}\left(\frac{1}{l_2} - \frac{1}{l_1}\right)_{liquid}\right) \tag{2.30}$$

as

$$r_{total} = r_{win} \cdot r_{liquid} \tag{2.31}$$

or

$$r_{liquid} = \frac{r_{total}}{r_{win}} = exp\left(t_{liquid}\left(\frac{1}{l_2} - \frac{1}{l_1}\right)_{liquid}\right) \tag{2.32}$$

then

$$ln(r_{total}) - ln(r_{win}) = t_{liquid}\left(\frac{1}{l_2} - \frac{1}{l_1}\right)_{liquid} \tag{2.33}$$

making the final equation for liquid layer calculation:

$$t_{liquid} = \frac{ln\,(r_{total}) - ln\,(r_{win})}{(1/\ell_2) - (1/\ell_1)} \tag{2.34}$$

The window thickness intensity values for Formvar, Si_3N_4 and Carbon are shown in Table 2.9.

Table 2.9: Int_1/ Int_2 for Two Windows

window	Int_1/Int_2
Formvar	1.017 ± 0.003
Si_3N_4	1.053 ± 0.002
Carbon	1.011 ± 0.002

The workflow used to determine the mean liquid thickness within the AAO wells is shown in Figure 2.16.
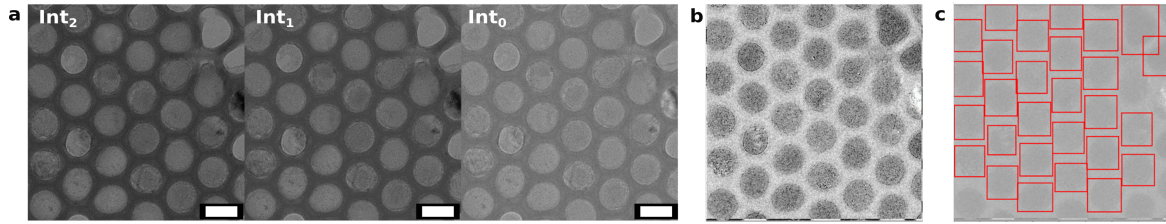
Figure 2.16: Workflow for mean liquid thickness determination. a) Int_2, Int_1, Int_0 carbon AAO LC micrographs with a scale bar of 100 nm. b) aligned Int_2, Int_1. c) Marked AAO wells used for liquid thickness determination.

The Int_2, Int_1, and Int_0 micrographs (a) were aligned to correct for drift (b). In the case of the two aperture approach, Int_2 and Int_1 are aligned and for one aperture, Int_1 and Int_0. The intensity of each AAO well was marked and used to calculate the mean liquid thickness.

2.5.3   Assembled AAO Liquid Cells

Similar to the static LCs prepared in Section 2.4.3, a 0.3 μl drop of the 20 mM $HAuCl_4$ solution was sandwiched between the two windows. A minimum of 30 minutes passed from

the time the sample was assembled until imaging. This resulted in a proper seal and filling of the AAO wells. A representative micrograph from a formvar LC assembly is shown in Figure 2.17.
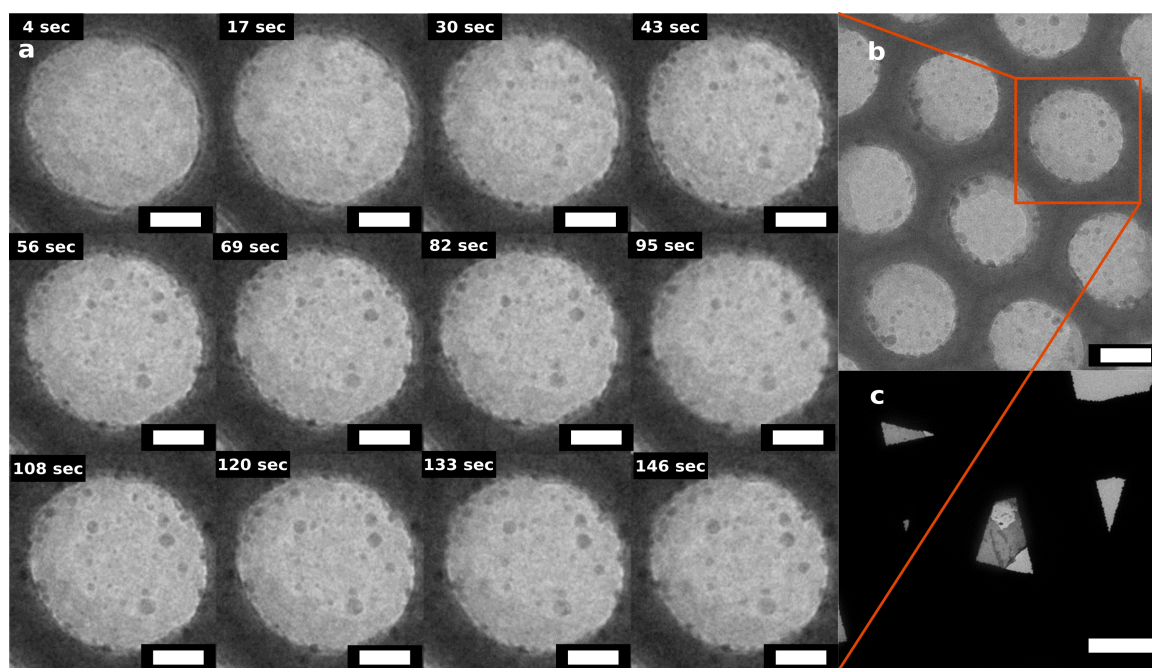
Figure 2.17: Micrographs from a formvar AAO LC assembly containing 20 mM of $HAuCl_4$ solution imaged at 3 e$^-$/Å^{2}s. a) montage showcasing AuNP growth within one AAO well, scalebar set to 25 nm, b) multiple AAO wells after 146 seconds of irradiation, scale bar set to 50 μm, c) low magnification region showing the TEM grid bars, scale bar 25 μm.

Here a dose rate of 3 e$^-$/Å^{2}s was used for imaging the growth of AuNPs (a). The AuNPs are clearly visible after 17 seconds. Figure 2.17 b shows multiple wells containing AuNPs after 146 seconds. As the AAO sheet is not cut to the full dimensions of the 3 mm TEM grid, there are regions without AAO. However, AAO and non-AAO regions are clearly distinguishable, as shown in c. As the beam alignment and finding a suitable imaging region both expose the sample to unwanted beam effects, the fact that the AAO is easy to locate already minimizes adverse beam effects with this assembly. Furthermore, due to the AAO acting as a spacer, the liquid layer was under 150 nm for the initial formvar, carbon, and Si_3N_4 LC assemblies. Therefore, when it comes to using AAO LCs, as depicted in

Figure 2.18, the AAO sheet (a) on the TEM grid (b) results in an LC assembly where the un-even alignment of the TEM bars (c) and sporadic pockets of liquid as depicted in Figure 2.13 are no longer present due to the confined micro-wells of the AAO (Figure 2.18d).
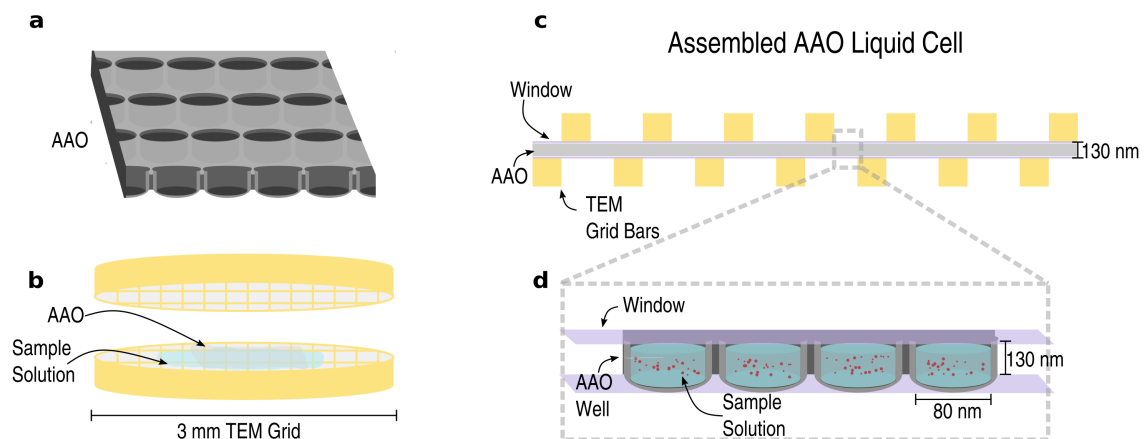
Figure 2.18: Schematic of assembled AAO Liquid Cell depicting AAO sheet (a), the AAO on a 3 mm TEM grid (b), assembled view (c), zoomed in region between grid bars (d).

The results from this section highlight alternatives to tedious nano-fabrication steps used to make standard LCs or advanced LC configurations by using 3 mm TEM grids as a support structure. The results show that formvar and carbon are suitable window materials for static LCs (Section 2.4.3), how adding an AAO sheet improves the available viewing region and liquid layer stability through the confined microwells.

2.6 Conclusion

This chapter highlighted novel LC configurations as a way to tackle three issues facing the LPEM community: 1) uncontrollable liquid layer, 2) window bulging, and 3) accessibility. This was achieved by developing the ELC (Section 2.3) and 3 mm AAO LCs with formvar, carbon, and Si_3N_4 windows (Section 2.5.3). By adjusting the flow and pressure valves of the ELC, the liquid layer was easily tailored for viewing AuNPs and the hydration of PNIPAM NGs containing a silica core. In a normal LC flow cell, the windows' bulging allows imaging to occur at the window periphery. The ELC circumvents this by adding the 10 μm Kapton spacer and focusing on the bottom window containing the thin liquid

layer. These modifications allow the imaging of the whole 200 x 30 x 0.02 μm window. Section 2.3 introduced ways to determine thickness with parallax measurements, the ratio of image intensities, and a computed values from a Monte Carlo simulation. The thickness methods presented are in lieu of EELS, which was not available for this work. The fact that these methods gave thickness values within reason of one another shows the scope of ways to calculate thicknesses. Although the ELC Section 2.3 addressed the two issues, it required a special holder and LC chips and therefore is not accessible to the larger LPEM community.

The aim of Section 2.4 satisfies the issue of accessibility by introducing LCs on a 3 mm TEM grid. A 0.3 % solution of formvar in DCE prepared by the drop method resulted in thin and homogeneous films. For the first time, I demonstrated that formvar films could be used for static LCs exhibiting an average liquid thickness of 190 $\pm$ 11 nm. Additionally, this liquid thickness is close to the 187 $\pm$ 8 nm observed with carbon static 3 mm LCs. However, window bulging is not an issue with these configurations, the sporadic pockets of liquid result in a decent amount of time searching for a region with liquid. Luckily with the mean intensity, it is possible to gauge a region's liquid thickness; however, it still requires exposing the region, subjecting the sample region to excess radical species. A way to avoid this would be to have a way to strategically confine the liquid either by a set height between the two windows or small confined regions where the diffusion of radical species becomes less important.

Therefore, the implementation of confined micro-wells (Section 2.5) for LC designs was investigated. First, I investigated elliptical windows that relied on traditional nano-fabrication and lithography techniques. The difficulties of manufacturing thin-windowed nanofluidic chips resulted in LC chips unfit for LC assemblies. Therefore, AAO films were selected as a way to add a spacer and micro-wells. Up to now, the use of AAO films was only investigated with graphene LCs. However, due to the success of static LC assemblies with formvar and carbon windows, I have determined how to fabricate AAO LCs with formvar, carbon, and Si$_3$N$_4$ windows. With the addition of the AAO, the two aperture

approach to calculate the liquid thickness was introduced. This method is based on the ELC liquid thickness calculations. The novel AAO LCs had liquid thickness under 150 nm. Similar to the static LCs, the observation of AuNP growth was used as a gauge if the LC was filed or empty. The AAO LC assemblies resulted in thin liquid layers and clear particle growth. This affirms the use of formvar and carbon and, Si_3N_4 as suitable LC window materials. Therefore, with the AAO to a 3 mm TEM grid, I could stifle three main issues of LCs. However, the results presented in this section for both the ELC and AAO LCs highlight the importance of characterizing beam induced radiolysis and ways of mitigation. I address this in the next Chapter 3.

3. Characterizing Radiolysis via Gold Nanoparticle Growth

3.1 Motivation & Synopsis

The previous chapter addressed the issues of the uncontrolled liquid layer, window bulging, and accessibility by introducing a new technique: the environmental liquid cell (ELC). This was followed by fabricating a novel formvar LC window and preparing AAO LCs from formvar, carbon, and Si_3N_4 windows. This chapter focuses on the beam's interaction with the liquid, specifically by using AuNP growth to probe radical species. The first part discusses the fundamentals of scattering (elastic and inelastic) and radiolysis within LPEM. Then, I introduce the mechanism of gold nanoparticle nucleation and growth.

The second part presents experimental results with the formvar, carbon, and Si_3N_4 AAO LCs introduced in the previous chapter (2.5). Additionally, I included a carbon coated Si_3N_4 window for possible scavenging effects. I establish two ways to pick and track the AuNP growth and probe the impact three dose rates have on the growth dynamics of AuNPs. The fundamentals and results from this chapter serve as a basis for the systematic investigation of secondary electrons (SE) emission and return presented in Chapter 4.

3.2 Fundamentals of the Electron Beam Interacting with Aqueous Solutions and Samples

3.2.1 Elastic and Inelastic Scattering

There are two main ways primary electrons interact with atoms and result in radiation damage: elastic and inelastic scattering.[1, 153]

Within elastic scattering, the total kinetic energy is conserved via the transfer of energy from the primary electron to the nucleus (N), and there is no energy change in the scattering electrons and the generation of back scattered electrons (BSE). In contrast, inelastic scattering is when the primary electron interacts with the atom's electron shell,
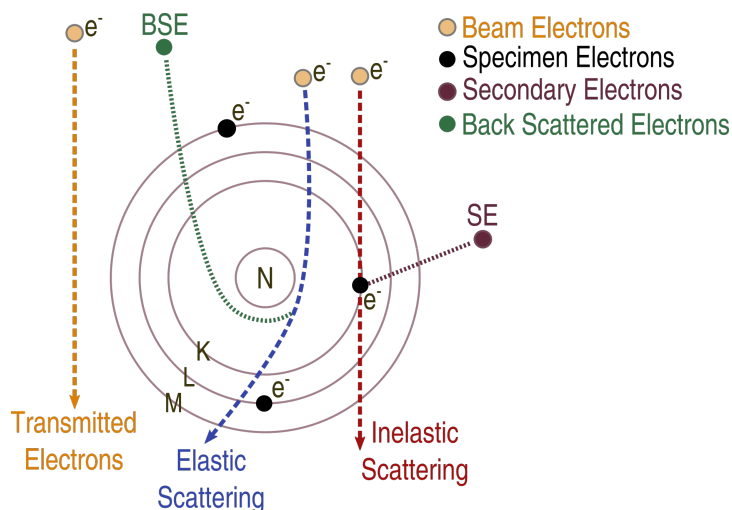
Figure 3.1: Description of how the electron beam interacts with a sample's nucleus (N) and electron cloud of electron shells (K,L,M). Electrons are either transmitted, elastically/inelastically scattered resulting in back scattered electrons (BSE) and secondary electrons (SE), respectively.

which causes energy loss and secondary electron (SE) emission (Figure 3.1).
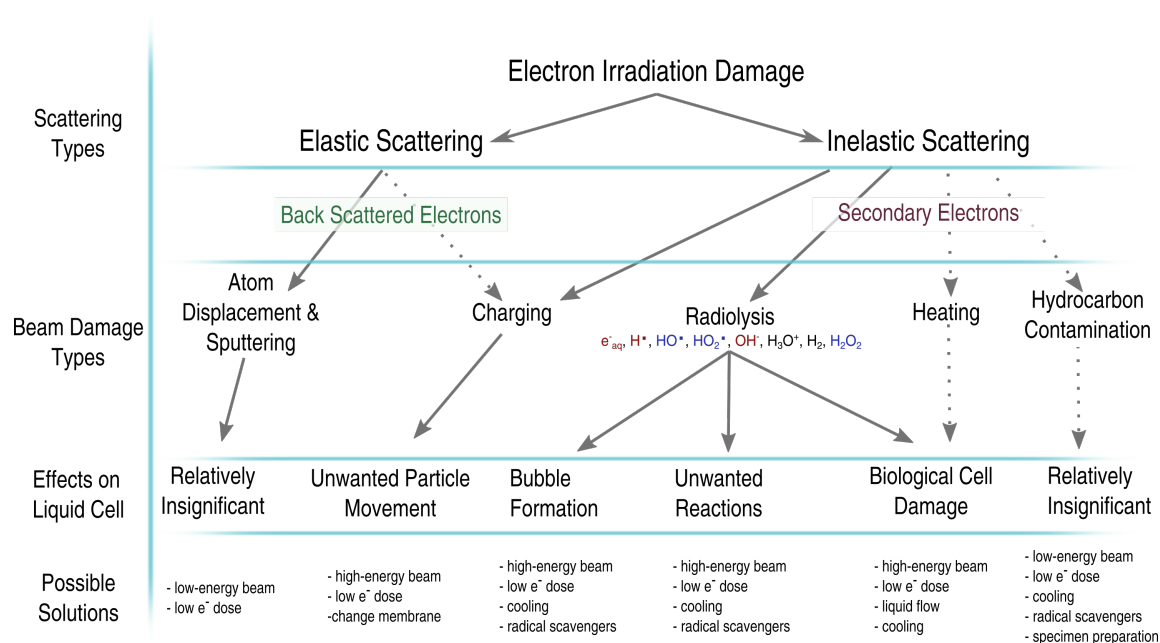
Figure 3.2: Types of electron beam damage and the influence on LPEM. Insignificant contribution is shown with dashed lines. Adapted with permission from ACS Energy Lett. 2018, 3, 6, 1269–1278. Copyright 2018 American Chemical Society. [1].

Elastic scattering can lead to high angle elastic electron scattering, which causes atomic

displacement of the nuclei or sputtering of surface atoms from the sample (Figure 3.2). This is not the main factor contributing to damage within LPEM. However, it could be mitigated through lower beam energy or dose.[154]

Electrostatic charging of poorly conducting windows and samples is another type of beam damage caused by elastic scattering and the secondary electrons (SE) generated from inelastic scattering events.[154] Charging from SE is described in more detail in Section 4.2. Although negligible with LPEM, it is essential to mention that inelastic scattering can result in heating and hydrocarbon contamination.[7, 153, 154]

Radiolysis is the most reported inelastic scattering event within LPEM. Bubble formation, unwanted secondary reactions, and biological damage can all occur here.[154] Traditionally, radiolysis is mitigated in two ways: 1) adding radical scavengers/sensitizers to the sample solution [56, 148, 155, 156, 157]; 2) changing the imaging parameters, for example, lowering the accelerating voltage, beam current, or dose rate.[153, 154, 155] However, the ELC results from Section 2.2.4 showed that resolution depends on the dose. Therefore for LPEM experiments, a trade-off between resolution and radiolysis needs to be considered.

3.2.2 Radiolysis of Water

Radiolysis is defined as the process of ionizing radiation from inelastic scattering that results in the decomposition of aqueous molecules.[56, 137] There are three main timescales for radiolysis: 1) physical stage (1 fs), 2) physio-chemical stage (10^{-15}-10^{-12}s), and 3) chemical stage (10^{-12}-10^{-6}s). These are outlined in Figure 3.3a.

Within the physical stage, spurs consisting of excited water molecules (H_2O^*), ionized water molecules (H_2O^+), and sub-excitations electrons (e^-) are generated.[111] This leads to the physico-chemical stage where dissociative relaxation:

$$H_2O^* \rightarrow HO^{\cdot} + H^{\cdot} \tag{3.1}$$

ion-molecule reaction:

52
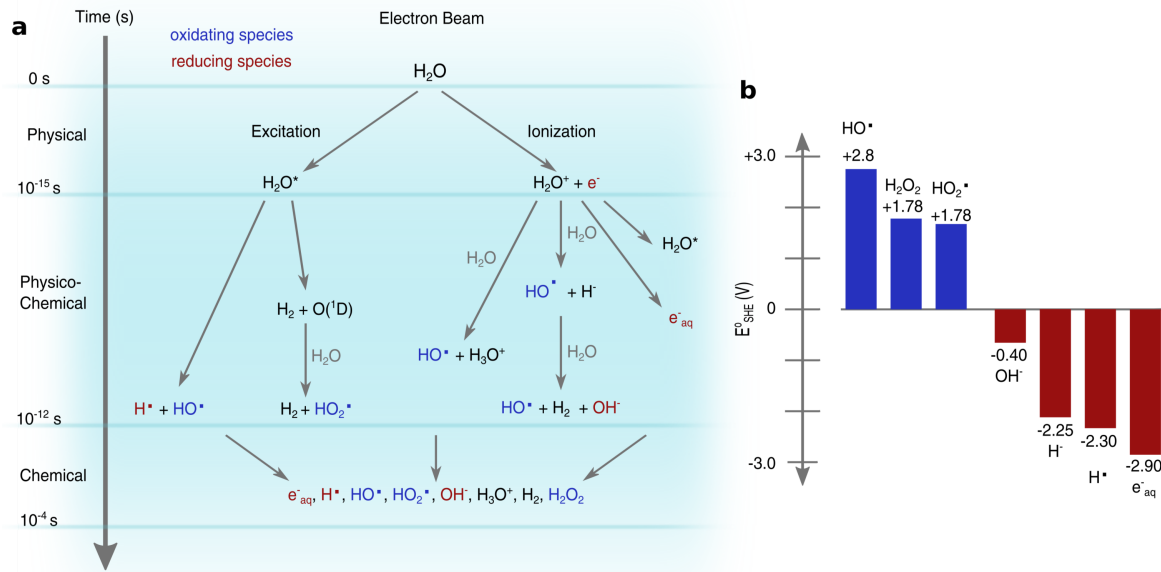
Figure 3.3: The three timescales of the radiolysis of water. (a) physical stage (1 fs), physio-chemical stage (10^{-15}-10^{-12}s) and chemical stage (10^{-12}-10^{-6}s). (b) standard potentials of products generated.[2]

$$H_2O^+ \; + \; H_2O \rightarrow H_3O^+ \; + \; HO^{\cdot} \tag{3.2}$$

and autoionization of excited states, thermalization of solvated/subexcitation electrons:

$$e^- \rightarrow e_{aq}^- \tag{3.3}$$
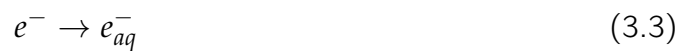
occurs. The chemical stage is where the species diffuse and react with molecules in the solution. Therefore in the case of pure water it predominantly decomposes to:

$$H_2O \longrightarrow e_{aq}^-, \; H^{\bullet}, \; OH^{\bullet}, \; H_2, \; H_2O_2, \; H_3O^+, \; HO_2^{\bullet} \tag{3.4}$$
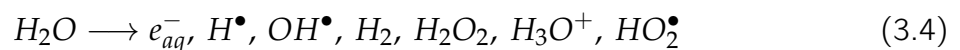
In total, 15 radiolytic species can form in water: hydrated electrons (e_{aq}^-), hydrogen radicals ($H^{\bullet}$), hydroxyl radicals ($OH^{\bullet}$), hydrogen (H_2), hydrogen peroxide (H_2O_2), hydroperoxyl radicals ($HO_2^{\bullet}$), hydroperoxyls (HO_2^-), protons (H^+), oxygen (O_2), superoxides ($O_2^{\bullet-}$), oxygen anions ($O^{\bullet-}$), ozone (O_3), hydrogen trioxy radicals ($HO_3^{\bullet}$), ozone anions ($O_3^{\bullet-}$), and hydroxide (OH^-).[56]

53

The main primary species are hydrated (solvated) electrons (e_{aq}^-), hydrogen radical ($H^\bullet$), hydroxyl radical ($OH^\bullet$), and hydrogen (H_2). The others are negligible.[3] Within roughly 1 μs after the start of the physical stage, the primary species are evenly distributed within the irradiation region.[3, 158] These species have either strong reducing or oxidizing standard potentials (Figure 3.3b).[2, 137] From the primary species, secondary chemical reactions take place. Within neat water, 79 subsequent reactions can proceed.[3, 159] Schneider *et al.* used a kinetic model to determine the concentration of radiolysis products at standard imaging conditions used in LPEM.[3] They simplify the model to consider neat water as a solvent because the concentration is substantially larger than the radiolysis products and the mass of water is constant throughout. They presented the influence increasing dose rates, aerated vs. deaerated liquid, pH, and heterogeneous vs. homogeneous illumination have on the concentration of primary species.

With dose rate (ψ) as:

$$\psi = \frac{S10^5 I}{\pi a^2} \quad (Gy/s) \tag{3.5}$$

which is defined as the amount of energy deposited per mass per time from ionizing radiation. The density-normalized stopping power in the medium is S = dE/dz (MeV cm^2/g/electron), I (A) is the beam current, and a (m) is the radius. A correction factor of 10^5 (m^2 electron Gy g/cm^2/MeV/C) is used to convert the value to SI units.[3, 25] For comparison, under normal imaging conditions for 100 keV electrons, 1 C/m^2 is roughly 0.23 MGy and 1 e$^-$/Å^2 is equivalent to 3.7 MGy.[154] Figure 3.4 shows the influence of radiolytic species as a function of time and with increasing dose rate.

In Figure 3.4a, the concentration of species plateaus after 10^{-3} seconds. Additionally, Schneider *et al.* found a power law influence on the concentration of radiolytic byproducts with dose rate (ψ)[3]

$$C_{ss,i} \sim \alpha_i \psi^{\beta_i} \tag{3.6}$$

by fitting the results in 3.3b, they found that increasing the dose rate increases the
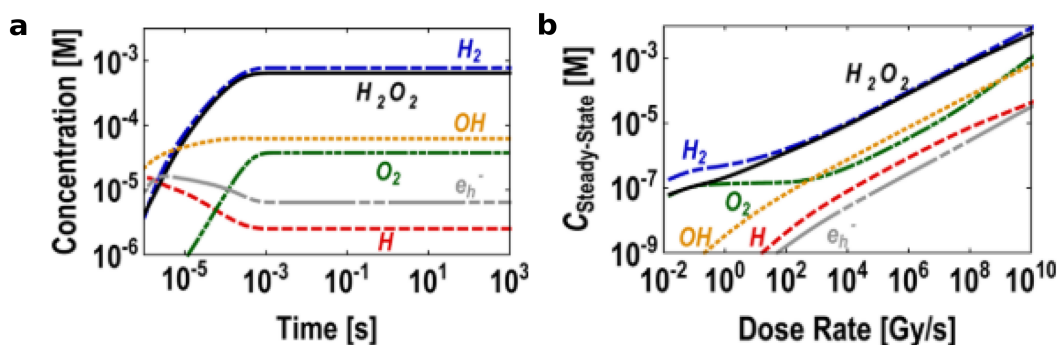
Figure 3.4: Simulated results from Schneider *et al.* a) Concentration of radiolytic species as a function of time in neat water irradiated at a dose rate of 7.5×10^7 (Gy/s). b) concentration of species with increasing dose rate. Figures reprinted with permission from J. Phys. Chem. C 2014, 118, 38, 22373–22382. Copyright 2014 American Chemical Society.[3]

radiolysis products sublinearly ($0.3 < \beta_i < 0.84$) and that they reach a steady-state after ~ 1 ms. Therefore doubling the dose rate causes less than a two-fold increase in the concentration of radiolytic species.[3]

Currently, there is no direct way to quantify the concentration of primary species within LPEM. Therefore, indirect ways to visualize the changes in solution chemistry have been carried out. In particular by observing the formation of gas bubbles from the generation of H_2 and O_2 or by nanoparticle growth and dissolution from e^-_{aq} and $OH^\bullet$, respectively. [3, 111, 160] The gold nanoparticles (AuNP) growth from a 20 mM $HAuCl_4$ solution is used in the remainder of this work.

3.2.3 Formation of Gold Nanoparticles (AuNP)

3.2.3.1 Reduction

The formation of AuNPs requires the reduction of Au^{3+} to Au^0. For the bulk synthesis of AuNP, citrate acid is used as the reductant.

$$Au^{3+} + C_6H_5O_7^{3-} \rightarrow Au^0 \tag{3.7}$$

However, as pointed out in Section 3.2, the interaction of water with the electron

beam results in oxidating and reducing primary radicals. These increase with dose rate and can undergo secondary reactions with the sample and the surrounding solution. Therefore with LPEM, the reduction can proceed by [161]

$$Au^{3+} + 3e_{aq}^- \rightarrow Au^0 \qquad E^0 = 1.5\ V \qquad (3.8)$$

$$Au^{3+} + 3H \rightarrow Au^0 \qquad (3.9)$$
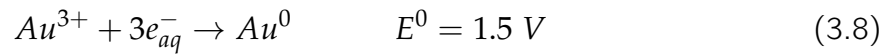
The e^-_{aq} is the main radiolytic species to partake in the reduction process. This is due to the strong reducing potential: $E^0(H^2O/e^-_{aq}) = -2.87$ V (Figure 3.3b).[25, 148, 161] With the presence of Cl$^-$ ions in the HAuCl$_3$ solution, a tetrachloro gold complex (AuCl$_4^-$) forms instead of the Au^{3+} ions in reaction 3.8. This is in part due to the lower standard redox potential.[31]

$$[AuCl_4]^- + 3e_{aq}^- \rightarrow Au + 4Cl^- \qquad E^0 = 1.0\ V \qquad (3.10)$$

Within reaction 3.10, three steps occur. First, the reduction of Au(III) to Au(II)

$$[Au^{III}Cl_4]^- + e_{aq}^- \rightarrow [Au^{II}Cl_4]^{2-} \qquad E^0 = 0.926\ V \qquad (3.11)$$

then the rapid disproportionation of Au(II) to Au(I) and Au(III) (rate constant of $5x10^8$ L/mol s). This is mediated through chloride complexes[25]

$$2[Au^{II}Cl_4]^{2-} \rightarrow [Au^{III}Cl_4]^- + [Au^{I}Cl_2]^- + 2\,Cl^- \qquad (3.12)$$
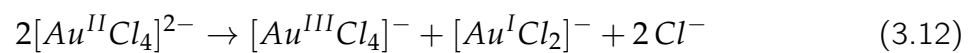
followed by the reduction with a solvated electron (e^-_{aq})[148]

$$[Au^{I}Cl_2]^- + e_{aq}^- \rightarrow Au^0 + 2Cl^- \qquad E^0 = 1.154\ V \qquad (3.13)$$

The generation of Au^0 is non-linear with time. This is due to the stability of $Au^{I}Cl_2^-$ generated in reaction 3.12. It is not reduced until a critical dose is reached and $Au^{III}Cl_4^-$

ions are consumed. Therefore, the Au(0) is not formed until the ratio of Au(I)/Au(III) is close to unity.[25]

3.2.3.2 Nucleation

Nucleation is the first step in AuNP growth. It can be described with classical nucleation theory (CNT). Here, the system thermodynamically wants to minimize its Gibbs free energy (or maximize the system's entropy).[95, 162] Two types of nucleation proceed: heterogeneous and homogeneous. Heterogeneous nucleation occurs at phase boundaries and impurities, with lower effective surface energies. These decrease the activation energy and are preferential sites for nucleation. Homogeneous nucleation requires a supercritical state for spontaneous and random nucleation. Here, nucleation and the subsequent growth occur when the system overcomes an energy barrier (activation energy, ΔG_c) and the critical radius (r_c) is reached. The energy on one nucleus depends on the surface energy (ΔD_s) and volume energy (ΔD_v) (Figure 3.5a). Growth is favored when the cluster is larger than r_c. With nano particle systems, both heterogeneous and homogeneous nucleation occur in concession or in parallel.[4]
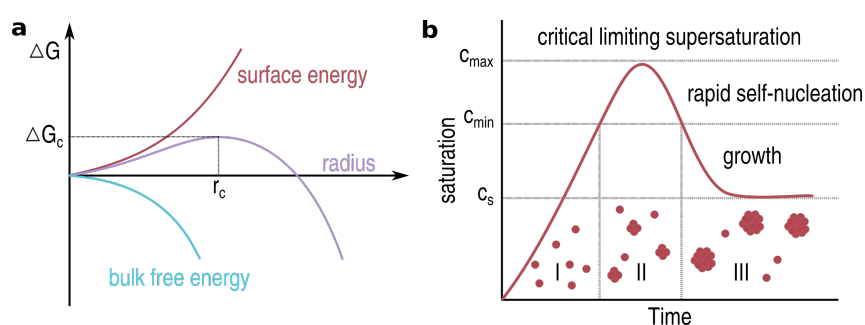
Figure 3.5: a) Cluster dependence on Gibbs free energy ΔG on the cluster radius (r). The curve shows the activation energy required (ΔG_c) for the critical size (r_c) of a stable particle. b) nucleation based on LaMer's theory showing the monomer concentration with time. Figures adapted from Ref [4] with permission from the Royal Society of Chemistry.

LaMer's nucleation builds upon CNT to describe burst nucleation in which clusters generated during homogeneous nucleation grow without further nucleation. With this

mechanism (Figure 3.5b), the concentration of monomer increases. At a certain time, the critical supersaturation level (C_s) is reached, and homogeneous nucleation is possible. At C_{min}, the activation energy is surpassed, resulting in self/burst-nucleation. This, in turn, leads to a lowering of C_s and a leveling of nucleation. This process results in a rapid self-nucleation stage (II) followed by constant growth (III).

3.2.3.3 Growth

In addition to LaMer's nucleation theory, growth has been modeled with the Lifshitz-Slyozov-Wagner (LSW) theory and used within the LPEM community to describe NP growth.[23, 25, 28, 30, 91, 163, 163, 164, 165, 166] Here the NP growth is described as diffusion limited or reaction limited growth. A spherical NP's growth rate with radius r_{sp} is described by [130, 167]

$$\frac{dr_{sp}}{dt} = \frac{2\sigma_s V_m^2 c}{RT\left(\frac{1}{d} + \frac{1}{k_d r_{sp}}\right)} \left(\frac{\frac{1}{r_c} - \frac{1}{r_{sp}}}{r_{sp}}\right) \tag{3.14}$$

Where r_c is the critical radius, σ_s is the surface free energy between cluster and solution, V_m is the molar volume, c is the monomer concentration in the bulk, R is the molar gas constant, k_d is the rate constant for deposition, and T is the temperature.

With diffusion limited growth, there is an abundance of reducing species. The reduction at the solid/liquid interface is greater than the rate of diffusion, or the rate is dominated by the atoms diffusing to the surface.[161, 168] Therefore, the product $k_b r_{sp}$ is larger than diffusion coefficient D. It is possible to derive r_{sp} from Equation 3.14:[130, 167]

$$\frac{dr_{sp}}{dt} = \frac{2\sigma_s V_m^2 c}{RT} \left(\frac{r/r_c - 1}{r^2}\right) = K_D \left(\frac{r/r_c - 1}{r^2}\right) \tag{3.15}$$

K_D is a constant and if the total mass is assumed to be conserved, r/r_c is constant leading to

$$\frac{dr}{dt} = K_D \, constant/r^2 \tag{3.16}$$

$$r_{sp}^3 - r_0^3 = K_{diff}t\,; \; K_{diff} = \frac{8\sigma_s D V_m^2 c}{9RT} \tag{3.17}$$

the radius of the particle at the beginning is denoted as r_0. With diffusion limited growth, the radius grows proportional to the cubic root of the time.

Reaction limited growth is when growth is limited by the solutes in the proximity diffusing to the solid/liquid interface; therefore D is larger than $k_b r_{sp}$.[161] The r_{sp} in the case of reaction limited can also be solved from Equation 3.14[130, 167]

$$r_{sp}^2 - r_0^2 = K_{reac}t\,; \; K_{reac} = \frac{2\sigma_s D V_m^2 c}{9RT} \tag{3.18}$$

Here the radius grows proportional to the square root of the time.[167] However, for the LSW theory to be applied to characterize particle growth, the following assumptions need to be met: 1) the particles are spherical; 2) the mass of the solute is conserved; 3) there is negligible aggregation. [169]

3.3 Experimental Preparation of LCs

3.3.1 Graphene Coating of Chips

Monolayer graphene "Easy Transfer" films from Graphena were used to coat the inside of a Si_3N_4 window. The protocol was adapted from Reference [170]. First, the graphene sample was placed in water to remove the polymer layer. The sacrificial layer/graphene floats on top of the liquid. Filter paper scoops the film out of the water. The film is cut to the desired dimensions with scissors, and the sheets are placed back into the water. Following a glow discharging step, the Si_3N_4 LC chips are introduced into the liquid at a 45° and scoop the floating film. The sacrificial layer/graphene/substrate is dried at room temperature for 30 minutes and annealed on a hot plate at 150 °C for 1h. The sacrificial layer is removed by dipping the layer/graphene/substrate into hot acetone (50 °C) and then iso-propyl alcohol, each for 1 h. A small stream of N_2 was used to dry the substrate.

3.3.2   AAO Liquid Cell Assembly

Herein formvar, carbon, Si_3N_4, and Si_3N_4-graphene AAO liquid cells were prepared as described in Section 2.4.1. In short, formvar films were fabricated from a 0.3 % solution of formvar in 1,2-dichloroethane and placed on 400 mesh TEM copper grids purchased from Plano GmbH. The AAO was placed on the graphene side of the Si_3N_4 chip. A 0.3 μl drop of 20 mM $HAuCl_4$ (purchased from Sigma Aldrich) dissolved in deionized (DI) water was applied to the AAO window. A detailed description of the assembly is found in Section 2.4.1.

3.4   Tracking AuNP Growth

3.4.1   Average AuNP Growth

The workflow used for particle analysis is shown in Figure 3.6.
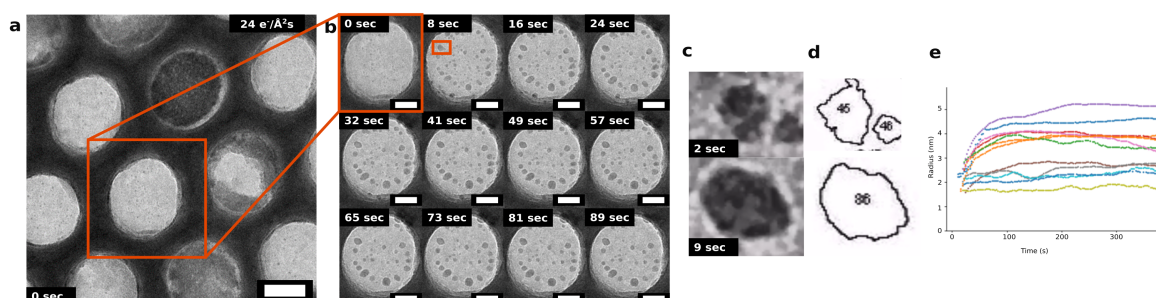
Figure 3.6: Workflow for average AuNP growth. a) aligned micrograph of formvar AAO LC with one well selected, scale bar 100 nm; d) growth of AuNPs within one AAO well and a marked particle; c) cropped particle d) corresponding thresholded and picked particle periphery; e) radius vs. time of the individual particles from c.

Fiji (ImageJ) was used to analyze the growth of AuNPs. One AAO well was cropped and aligned with the SIFT plugin (a). A minimum of 7 individual particles within the AAO well were cropped (c), median filtered (to two pixels), and thresholded. The particle size was analyzed with the analyze particle plugin with areas ranging from 2-90 nm^2, and circularity 0-1 (d). The resulting particle growth profiles were averaged together to get the increase in radius with increasing time or cumulative dose (e).

3.4.2 Total AuNP Growth

First, Fiji/ImageJ was used. The signal to noise decreases with decreasing dose rate. Therefore I averaged micrograph frames (Table 3.1), then aligned the frames with ImageJ Linear Stack Alignment with the SIFT plugin and inverted them in color.

Table 3.1: Averaging of Micrographs

Dose Rate ($e^-/Å^2s$)	Frames (#)	Cumulative Frame Dose ($e^-/Å^2frame$)	Time (s)
10	2	10.8	1.03
3	8	12.96	4.32
1	24	12.96	12.96

A python script based on "Custom Feature Detection: Bubble tracking in 2D foams" with trackpy was used to find and link the particle growth.[171] As I was only considering the particle growth within each AAO well, the first step involved thresholding the stack of micrographs for one movie and cropping the individual wells that were not touching the periphery of the imaging area. Picking of the AuNP involved initial thresholding of the individual AAO wells. The AuNPs were marked in each frame depending on whether the region area was greater or equal to 16 pixels. Trackpy was used to connect the particles between each frame. The tracked particles were discarded if they disappeared for two frames and were present in less than 20 frames to remove noise marked as a particle. This procedure was repeated for the individual wells from one movie to get the total AuNP growth. A representation of this workflow for carbon AAO LCs is shown in Figure 3.7

3.5 Nucleation of Gold Nanoparticles: With Different Dose Rates and Window Material

This section uses AuNP growth to highlight beam induced radiolysis. The influence of window charging and secondary electrons generation are in Chapter (4). The simulations from Schneider *et al.* in Section 3.2.2 state there is a dose rate dependence on the
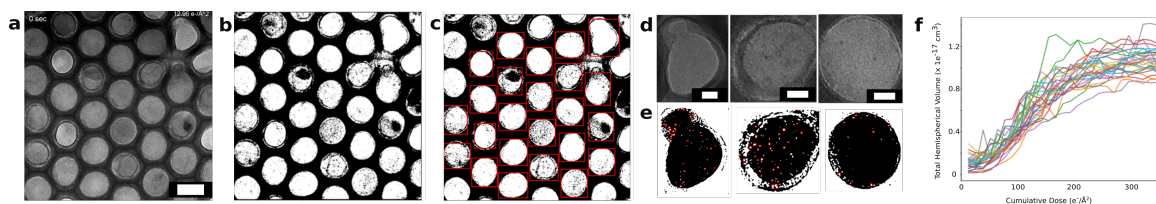
Figure 3.7: Workflow for semi-automatic particle picking. a) aligned micrograph of carbon AAO LC, scale bar 100 nm; d) thresholded image; c) marking the individual wells with a red box; d) cropped wells, scale bar 25 nm; e) thresholded wells with AuNPs marked in red; f) total hemispherical volume with an increasing cumulative dose of the particles with each line the total hemispherical volume within each AAO well.

concentration of radical species. Therefore I imaged the AuNP growth under three different dose rates (Figure 3.4). In addition to varying the dose rate, I used formvar, carbon, Si_3N_4, and Si_3N_4 coated graphene (Si_3N_4-C) AAO LC configurations. This is the first time these window combinations are used to investigate the influence dose rate has on AuNP growth.

First, I got a general overview of the AuNP growth by taking the average AuNP growth. Here 7 AuNP were selected, and the size and morphology were analyzed with a standard Fiji plugin. The results are shown in Figure 3.8.
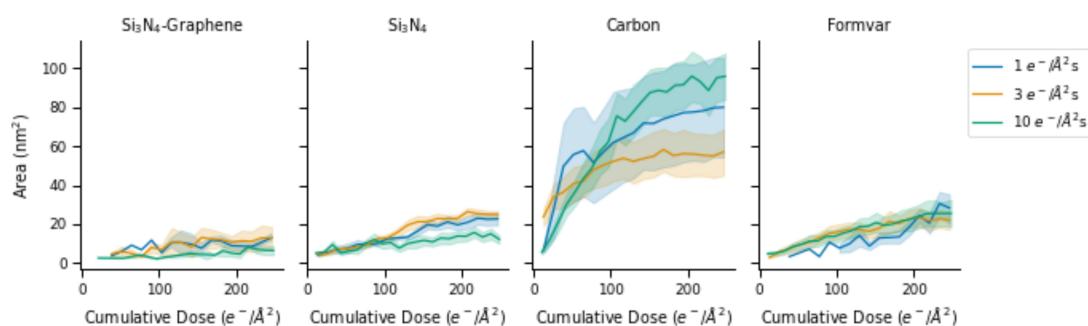
Figure 3.8: Growth of AuNP with increasing cumulative dose at the three dose rates and four window combinations. Average area of 7 AuNP particles.

In Figure 3.8a, carbon exhibits the largest AuNP growth. With this analysis method, the dose rate does not appear to influence the average AuNP area. Although manually picking and tracking particle growth to characterize growth dynamics is a reported method[25,

30, 95, 150, 165, 172], it could introduce user bias and misrepresent the complete picture of the growth dynamics. To circumvent this, I transitioned from the 7 particle method. I developed a semi-automated Python script that allowed for the analysis of the AuNP within the field of view (introduced in Section 3.4.2). This is used for the remainder of the work to track AuNP growth.

The results of the total AuNP growth for the four window materials normalized to the number of AAO wells and three dose rates are shown in Figure 3.9.
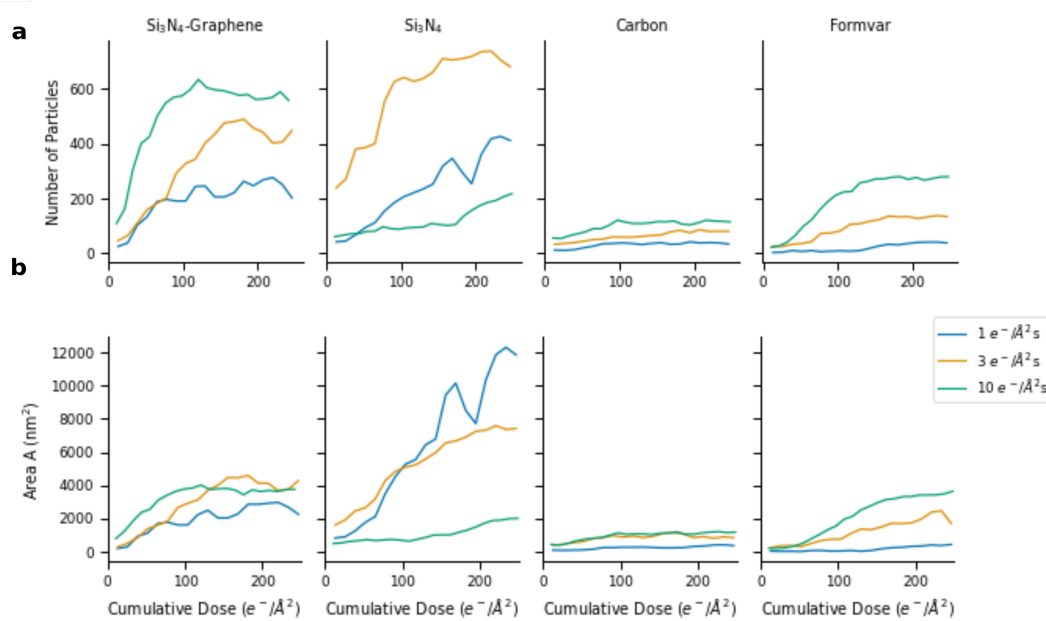
Figure 3.9: Total AuNP growth with increasing cumulative dose normalized for the number of AAO wells for the three dose rates and four window materials. a) total number of particles, b) total area of AuNP.

There is a fast increase in the number of particles in all cases, followed by a plateau (Figure 3.9a). The total area exhibits a similar trend (Figure 3.9b). This eludes aggregation, coalescence, or Ostwald ripening of particles was minimal to nonexistent.[173, 174] The concentration of $HAuCl_4$ solution was the same for all LC window configurations. Therefore the plateau is likely due to the system reaching a dynamic equilibrium rather than running out of precursor solution. Liquid layer calculations based on the procedure in Section

2.5.2.2 reveals liquid layer thicknesses of 135 $\pm$ 40, 104 $\pm$ 36, 34 $\pm$ 14, and 60 $\pm$ 10 for Si$_3$N$_4$-graphene, Si$_3$N$_4$, carbon, and formvar.

In general, increasing the dose rate directly influenced the total number and total area AuNP. Only Si$_3$N$_4$ with 10 e$^-$/Å^{2}s is the only outlier. Previously the 7 particle method revealed the largest growth for carbon (Figure 3.8a). Here carbon exhibited not only fewer particles but also lower area. The variation is likely due to these results considering the number of AAO wells in the viewing region. In the case of carbon, AuNPs were not in every AAO well. These variations highlight the importance of analyzing the whole region and not just 7 particles.

3.5.1 Sacrificial Scavenging of Window Materials

The fact that carbon exhibited the lowest total number and area of AuNP in Figure 3.9 could be due to the thin liquid layer or conductive/scavenging nature of the material.[18, 154, 175]

Coating graphene on the inside of the Si$_3$N$_4$ windows did not influence the number of particles and only caused a slight decrease in the total area. There are three possibilities for this: 1) the graphene coating was not homogeneous, and growth was recorded in pristine Si$_3$N$_4$ regions, resulting in similar growth. 2) Debris on the graphene film from the coating procedure created sites for AuNP nucleation, so the number of the particles stayed roughly the same. 3) Poor applicability of using graphene as a e$^-_{aq}$ scavenger.

It is difficult to rule one and two out as diffraction before each movie to ensure a graphene coating and surface analysis to observe the cleanliness of the window were not performed. However, results from electron spin resonance spectroscopy and spectrophotometric studies show that graphene scavenged hydroxyl radicals and that there is an electrophilic addition to conjugated C=C π bonds.[176, 177, 178, 179] Additionally oxygen-containing functionalities can be further oxidized.[175] Therefore in regions with the graphene coating, there should be bubble formation. Figure 3.10 contains representative micrographs from Si$_3$N$_4$, Si$_3$N$_4$-graphene, and carbon AAO LC assemblies imaged at a dose rate of 1 e$^-$/Å^{2}s.

Here, the Si$_3$N$_4$ (a) and carbon (c) assemblies did not result in bubble formation. In
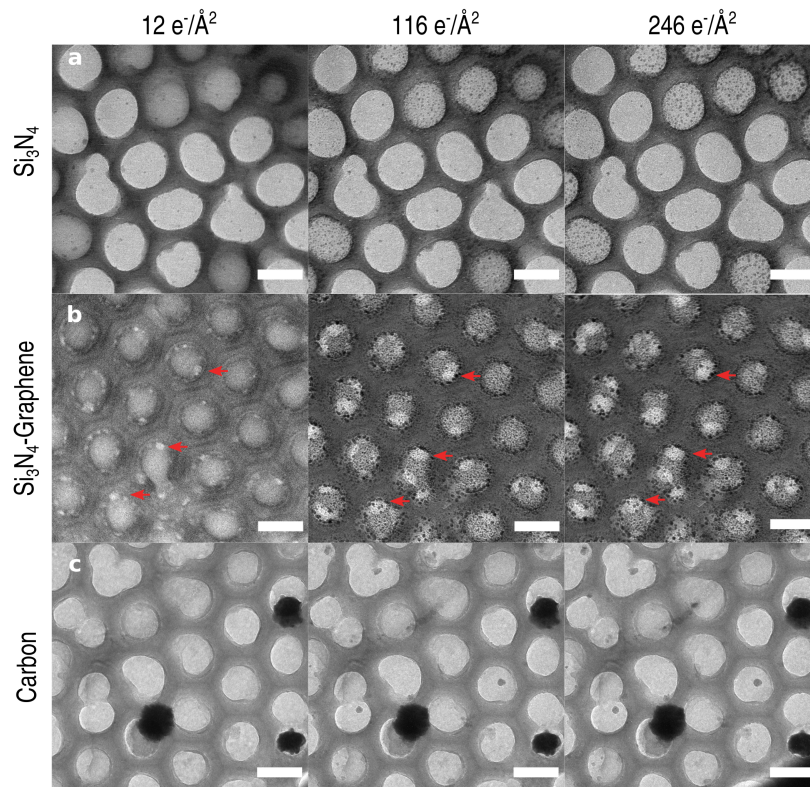
Figure 3.10: Averaged micrographs depicting AunP growth and bubble formation at a dose rate of 1 e$^-$/Å^{2}s with different window configurations. The micrographs here are an average of 24 frames, resulting in a cumulative frame dose of 12 e$^-$/Å^2. Red arrows point to some bubbles. The scale bar is 100 nm.

comparison, bubbles are present in the case of Si$_3$N$_4$-graphene (b). The thin liquid layer is a possible explanation for the lack of bubble generation in the conductive carbon window. Liquid layers for Si$_3$N$_4$-graphene and Si$_3$N$_4$ assemblies were approximately twice as thick as carbon and formvar. The thin liquid decreases the total growth and the generation of radical species.[25] Consequently, the experiment should be repeated in the case of the carbon AAO LC to determine if it was the liquid layer or the window properties preventing bubble formation. The apparent bubble growth inside the Si$_3$N$_4$-graphene AAO wells demonstrates 1) the graphene coating was successful; 2) The O$_2$ bubble generation to some degree scavenges e$^-_{aq}$, which is required for AuNP growth[3, 56, 95]; 3) graphene is not chemically inert as proposed by Cho *et al.*[175] 4) the AAO creates individually sealed micro-wells, as demonstrated by the bubbles only in the AAO well.

Accordingly, the graphene coating dramatically improves the electron dose tolerance

for biological samples as they are more prone to damage by oxidating species rather than reducing.[18, 175] Whereas, it does not make a significant difference for AuNP growth as the scavenging of e^-_{aq} only proceeds as a byproduct from the primary scavenging of hydroxyl radicals.

3.6 Kinetics of Gold Nanoparticle Growth

3.6.1 Power Law Dependency Between AuNP Growth and Dose Rate

Increasing the dose rate increases the concentration of radical species (Section 3.2).[3] Park *et al.* built upon the simulations by Schneider *et al.* to include Cl^- and H^+ and found a power law dependency between the concentration of e^-_{aq} and dose rate to be between 0.5 to 0.79 depending on the solution pH.[25] Here the primary mechanism for AuNP growth is assumed to be e^-_{aq} reducing Au^{3+} to Au^0 (Section 3.2.3). Therefore the concentration of e^-_{aq} is directly related to the AuNP growth rate.

To observe if the growth rates with different dose rates in Figure 3.9 followed the e^-_{aq} power law dependency, I took the linear fit and plotted the respective slopes vs. dose rate (Figure 3.11b).

The respective slopes vs. the dose rate resulted in an average growth rate of 0.84 $\pm$ 0.37 (Figure 3.11). The individual slopes for Si_3N_4-Graphene, Si_3N_4, Carbon, and Formvar are 0.85, 0.29, 0.32, 1.9, respectively. Although the individual growth rates are lower for Si_3N_4 and carbon, the average value is comparable to the power law dependency of AuNP growth with increasing dose rates, as also observed by Park *et al.* and Alloyeau *et al.* at much higher dose rates.[25, 165] As formvar and carbon had similar liquid thicknesses but different slopes, these results elude that the window material, not liquid layer thickness, is influencing the growth with respect to increasing dose rate.

3.6.2 Reaction and Diffusion Limited Growth: LSW Model

Next, I compared the AuNP growth to the Lifshitz-Slyozov-Wagner (LSW) model for particle growth by fitting the logarithmic relationship between particle radius and time. The slope corresponds to the growth exponent (β) which is defined from the LSW model
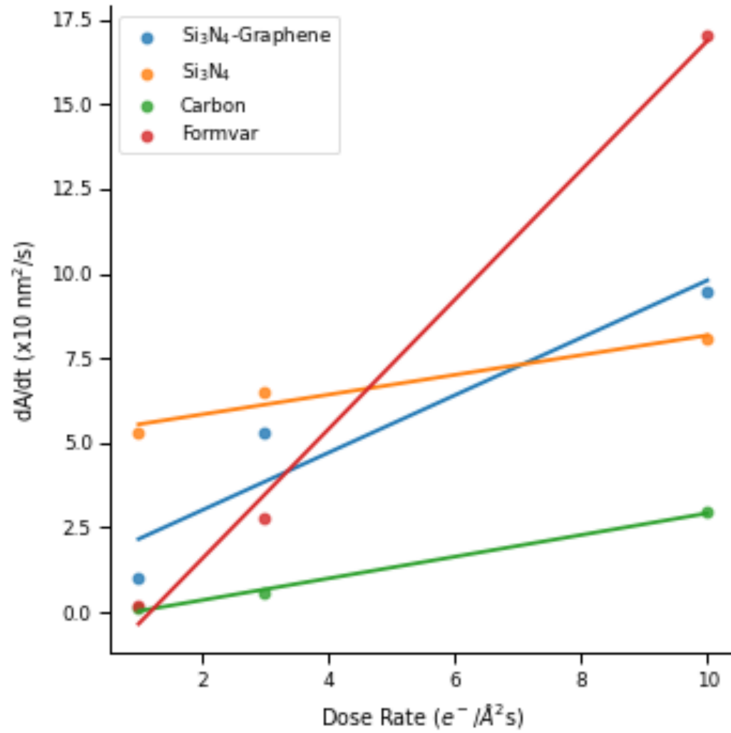
Figure 3.11: Steady-state concentration of primary radiolytic byproducts in aerated 20 mM $HAuCl_4$ solution with increasing beam current corresponding to a range from 2 - 200 $e^- Å^{-2} s^{-1}$.

as $R \sim (A/\pi)^{1/2}$, which depends on time (t), $R \sim Kt^{\beta}$ with K and β as the reaction rate constant and growth exponent, respectively (Figure 3.12).[172, 180]

The linear fits up to a cumulative dose of 250 $e^- Å^{-2}$ (Figure 3.12a) reveals an increase in the growth exponent with an increasing dose rate (Figure 3.12b). Interestingly, although Si_3N_4 at 10 $e^- Å^{-2}$s had the lowest total number and area of AuNP for the other dose rates (Figure 3.9), here it has the highest growth exponent. The LSW model, as introduced in Section 3.2.3.3, characterizes diffusion limited growth when $R \propto t^{1/3}$ and reaction limited when $R \propto t^{1/2}$.[30, 165, 181] In the Si_3N_4-Graphene, Si_3N_4, and Formvar windows reaction limited growth was observed for 10 $e^- Å^{-2} s^{-1}$, and diffusion limited growth for 3 $e^- Å^{-2} s^{-1}$. The increase in dose rate causes a higher concentration of e^-_{aq} in the liquid layer (Section 3.2.2). This brings the growth closer to reaction limited as there are sufficient reducing species at the solid/liquid interface. The spur density or concentration of reducing species is lower with the lower dose rates.[111, 150] Therefore, the reaction rate at the solid/liquid
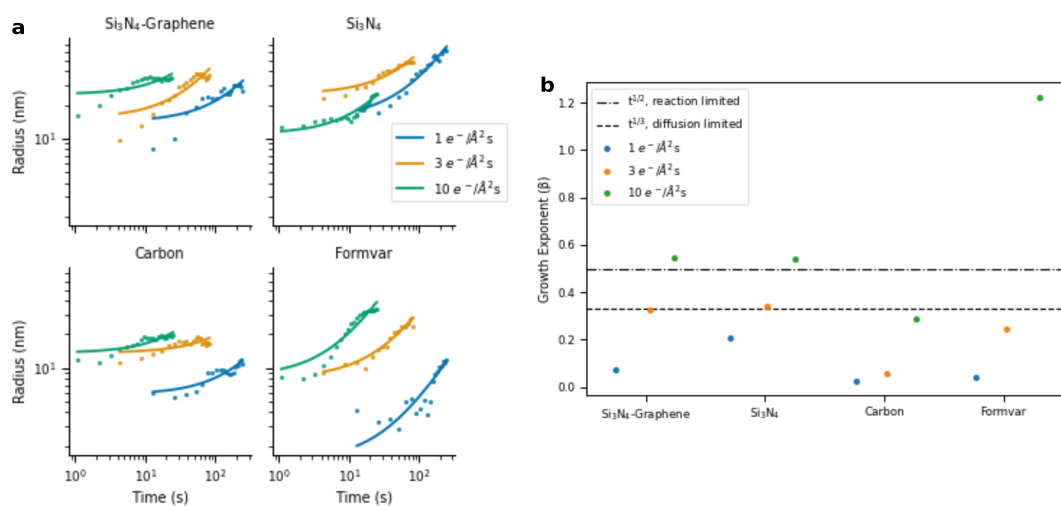
Figure 3.12: Fitting the growth to the LSW model. a) logarithmic plot of AuNP growth with linear fit to a cumulative dose of 250 e$^-$Å^{-2} b) corresponding time growth exponent (β) from the slope of the linear fit in a.

interface proceeds faster than the rate of atoms diffusing to the surface.

The carbon assembly was close to diffusion limited only for the highest dose rate. Woehl *et al.* and others also observed values up to three times lower than diffusion limited growth.[55, 95, 182, 183] Three possible explanations for this: 1) The growth occurred on the window (not in bulk), which makes the LSW model invalid.[30, 169] 2) The thin liquid layer increased the viscosity, slowing down the diffusion limited growth process.[95] If only the liquid layer was to play, formvar with a comparable liquid thickness should have had growth exponents similar to carbon. 3) Other mechanisms such as secondary electrons (SE) escape/return play an equal role in AuNP growth

3.7   Conclusion

This chapter introduced the essence of elastic and inelastic scattering, how this leads to radiolysis, and how the species can undergo secondary reactions. As AuNP growth was used as the probe, the reduction mechanism with e$^-_{aq}$ was introduced. I used formvar, carbon, and Si$_3$N$_4$ AAO LCs from Chapter 2 and introduced a Si$_3$N$_4$ coated graphene AAO LC for possible e$^-_{aq}$ scavenging.

First, I showed how user bias is introduced by manually picking and tracking AuNP

growth. I circumvented this by preparing a semi-automatic particle picking script. The total AuNP growth revealed, except for one outlier, an increase in both the total number and area of AuNP with increasing dose rate (1, 3, and 10 $e^-/\text{Å}^2$s). The LSW model showcased a similar trend. This chapter demonstrates how the dose rate can be used to tailor the growth of AuNP. I presented that adding a graphene layer to the inside of an insulating Si_3N_4 window results in bubble formation even at low dose rates. This suggests graphene scavenges hydroxyl radicals and the scavenging of e^-_{aq} proceeds as a byproduct from O_2 bubble generation. The results indicated the average growth rate with increasing dose rate followed a power law dependency similar to the concentration of e^-_{aq} as presented by Park *et al.*[25] However, additional work must be done to elucidate why Si_3N_4-graphene and formvar had higher values and Si_3N_4, and carbon windows had lower values. I found the liquid layer to influence the total number and area of AuNP but not the growth rate. This implies that the window properties play a role in the rate of AuNP growth.

Fundamental considerations suggest that the role of LC window material on radiolytic products should extend beyond their potential action as sacrificial radical scavengers. Considering secondary electrons are precursors of e^-_{aq} (Section 3.2.2), the generation and dynamics of the former will play an essential role in the radiochemistry occurring in an LC [25, 184]. Therefore in the next chapter, I present the influence of SE escape and return with formvar, carbon, and Si_3N_4 AAO multiwell LCs.

4. Unveiling the Leading Role of Secondary Electrons in LPEM

4.1 Motivation & Synopsis

The previous chapter introduced hydrated (aqueous) electrons (e^-_{aq}) as one of the most reactive and important radiolytic species, followed by their role in the formation of gold nanoparticles (AuNP). The results showed that the total AuNP number, area, and growth rate increased with dose rate. Applying graphene to the inside of the Si_3N_4 window majorly influenced bubble generation and minimally altered the growth and growth rates. A correlation between liquid thickness and growth rate was not made. As SEs are the precursors of e^-_{aq}, the generation of the former influences radiochemistry and subsequent AuNP growth.

While SE emission is commonly used as a surface-sensitive signal in scanning electron microscopy (SEM), it is rarely employed or investigated in TEM/STEM [185, 186]. Specimen charging, a direct result of SE emission, is a widely discussed phenomenon in TEM (also LPEM) and has been described and explained in detail [187, 188, 189]. The ratio of the number of SE leaving a surface to the number of incident primary electrons is in the range of a few percent. This causes significant SE effects at interfaces, particularly the window: vacuum or window: liquid boundaries.[190] These effects strongly depend on the relevant material properties and local potentials. Gupta *et al.* numerically investigated the effect of differences in SE emission properties on local chemistry at interfaces inside an LC in some detail, confirming that the concentration of important radical species such as e^-_{aq} can be significantly affected in the proximity of solid/liquid interfaces.[191] However,

experimental studies of such phenomena, including considerations of the role of SE currents emitted into the vacuum are lacking in the LPEM community.

This chapter presents a systematic comparative study of in situ electron beam induced radiolysis by observing AuNP growth dynamics for a selection of LC window materials to investigate the role the SE play within LPEM. Following a brief introduction of the fundamentals of SE generation, I characterize AuNP growth for LC windows introduced in the earlier chapter: Si_3N_4, amorphous carbon, and formvar. The entire LC structure is biased to investigate the SE emission's influence on AuNP growth. A model is introduced to describe the SE dynamics based on window properties and external bias. This model is validated with electric field calculations and particle tracking simulations. Finally, I present an electrical hookup and LC assembly that allows for gated AuNP growth.

4.2 Fundamentals of Secondary Electrons

With electron microscopy, the acceleration voltage of primary/incident electrons generates elastic and inelastic scattering events (Figure 3.2). These result in back scattered electrons (BSE) and secondary electrons (SE), respectively (Figure 4.1a).[191] Direct measurement of SE and BSE are not possible with TEM and STEM. However, with SEM, the SE and BSE are the main signals collected by an Everhart-Thornley (E-T) detector to produce an image. When a positive bias is applied to the sample screen, both SE and BSE are collected. A negative bias results in the repulsion of low energy (< 50 eV) SE and only the collection of BSE.[192]

In LPEM, a percentage of SE will become solvated electrons (e^-_{aq}) in the liquid, as presented in Section 3.2. SEs still have sufficient energy to overcome the material work function and can thus transmit through the liquid escaping into the vacuum. The typical emitted SE energy spectrum exhibits a strong peak in the 2-5 eV range, although conventionally, all emitted electrons below 50 eV are regarded as SE [185]. Due to their low energy, the mean free path (MFP)/escape depth of SE in a material is in the few nm range, with insulators (e.g., Si_3N_4) generally showing a larger MFP in the order of 10 nm as compared to conductors (e.g., carbon) with less than 5 nm [193].
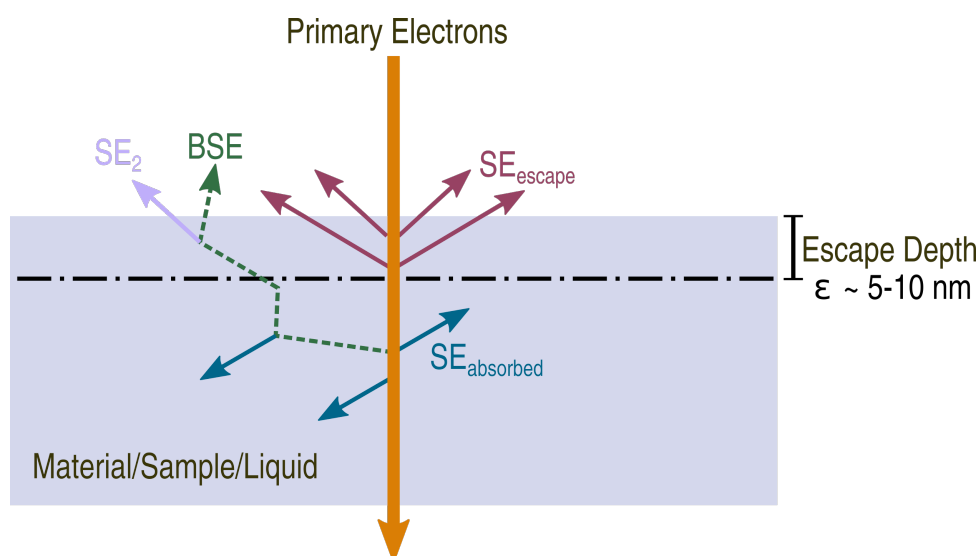
Figure 4.1: Generation of SE and BSE from the primary beam. This schematic shows three types of SE: SE that escape into the vacuum, SE that remain in the sample/substrate/liquid, and SE that are generated from BSE (SE_2).

With poorly conducting surfaces and samples, the ground electrons cannot maintain charge neutrality, and there is a buildup of positive charge within the sample.[194] Additionally, there is an electrostatic potential in the region of the SE.[195] As presented in Section 3.2.2, e^-_{aq} has a strong reducing potential and will preferentially react in solution rather than recombine with the holes in the positively charged window.[194] A thin oxide layer is present on liquid cell chips fabricated from silicon nitride windows. This layer subsequently allows electrons to travel from the solid to the liquid. This increases the dose at the solid-liquid interface and increases the window's positive charging.[137, 194, 196] Gupta *et al.* determined at the solid/liquid interface or between two materials that the exchange of SE and BSE (SEBSE) towards one another depends on the total SEBSE yield of each material and the material's stopping power. The dose flows from the material with a higher SEBSE towards the lower.[191] Cazaux calculated that an electric field of 10^{10} V/m is possible within insulating specimens.[197] This electric field spreads from the region of illumination to surrounding uncharged areas. This is why in the case of sample movement in LCs, nanoparticles move parallel to the optical axis, not perpendicular to it.[30, 197]

Although limited and relatively brief, ways to mitigate SE effects have been discussed outside and within the field of LPEM. For example, to alleviate the charging from SE escape in an insulating window, a thin conductive layer on both sides of the window would give a path for electron neutrality.[187, 197] Furthermore, performing an LPEM experiment with an electrolyte solution such as potassium chloride, sodium chloride, or gold chloride would offer some screening of the charge buildup through the negatively charged ions being attracted to the positively charged window.[194] Using a liquid cell with flow configurations (as described in Section 2.2.2) can mitigate the SE effects within the liquid.[198] However, this is only useful for non-mobile samples; otherwise, the sample could flow out of the field of view. Lowering the energy beam to decrease or prevent SE generation is not possible with conventional TEMs as it would require 50-150 eV, and that is too low for electrons to pass through a sample.[153] Increasing the energy resulting in a larger mean free path for scattering and a thinner sample, would cause the beam to easily transmit through the sample and decrease the secondary electron generation. Lowering the dose rate can also subside the charging.[199] Finally, switching from insulating silicon nitride to a conductive window such as graphene would mitigate the charging.[1, 18].

4.3 Experimental

4.3.1 Transmission Electron Microscopy

TEM was performed on a JEOL JEM-2100 operated at 200 keV. Bright-field micrographs were recorded at room temperature with a TVIPS TemCam F216 camera with no energy filter.

4.3.2 Fabrication of AAO Grids

The formvar TEM grid preparation was based on the procedure described by Both *et al.*[147] A detailed description of the preparation is found in Section 2.4.2. The AAO liquid cell fabrication was based on Lim *et al.* and introduced in Section 2.5.2.[152]

4.3.3 Carbon Coating of Chips

The Si_3N_4 chips were glow discharged for 30 seconds and placed in a Leica ACE60 carbon coater. A 5 nm layer of carbon was deposited to the backside of the AAO containing Si_3N_4 chips.

4.3.4 Liquid Cell Holder for AuNP Growth

The liquid cell holder described in Azim *et al.* was modified with new gaskets and an adapter to accommodate 3 mm TEM grids. [10] These modifications are depicted in Figure 4.2.
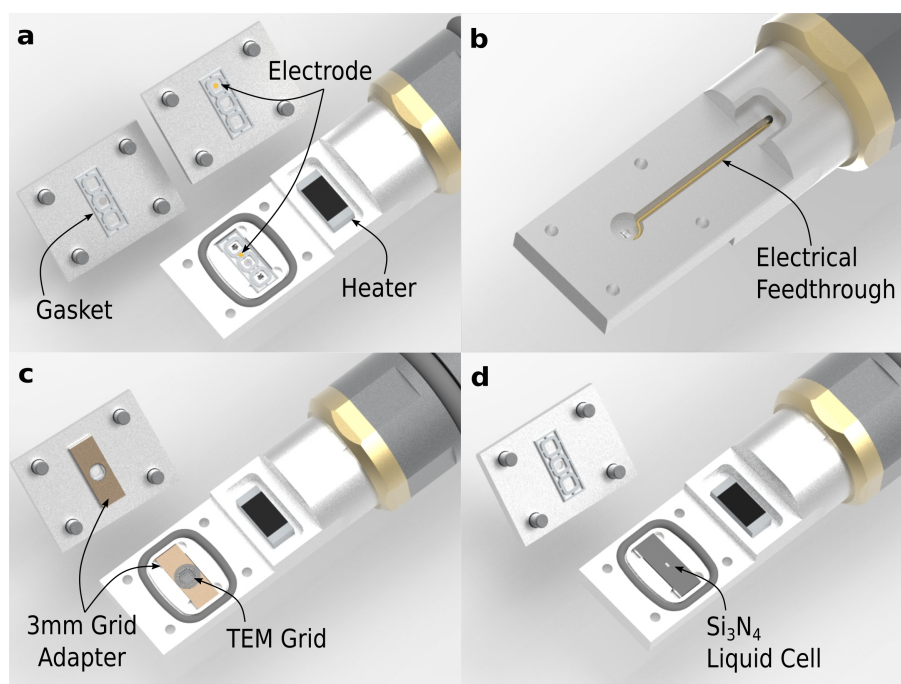
Figure 4.2: Modifications to liquid cell holder. a) gaskets on the lid and bottom with the electrode on the right lid and holder. b) backside of holder showing electrical feedthrough. c) adapter for 3 mm TEM grids. d) Si_3N_4 liquid cell.

Additionally, this holder was modified with an electrical feedthrough (Figure 4.2b) to include two electrodes, one in contact with the bottom liquid cell chip and the second connected to the outside holder through the lid (Figure 4.2a).

4.3.5 Liquid Cell Assembly

All assemblies took place outside of the liquid cell holder and used a 0.3 μl drop of 20 mM $HAuCl_4$ (chloroauric acid, $HAuCl_4$ (Sigma Aldrich) dissolved in deionized (DI) water). In the case of formvar and carbon, the $HAuCl_4$ solution was applied to an AAO containing TEM grid was held by tweezers, and a second TEM grid with a flat cut side was placed on top of the $HAuCl_4$ grid. The grids came together. The assembled grid was sandwiched between the two copper adapters in the liquid cell holder (Figure 4.2c). For the formvar and carbon TEM grids, the copper adapter conveniently ensured that the two windows were in contact with one another. For the Si_3N_4 liquid cell chips to be connected to the electrode, a small amount of silver paint was placed on the backside of the bottom chip. Silver paint was applied to the periphery of the assembled liquid cell to guarantee electrical contact between the chips.

4.3.6 Current Calibration

A correction factor similar to what was outlined in Azim *et al.* was determined to account for drift in the initial calibration of the current density readout on the phosphor viewing screen of the JEOL JEM2100 TEM.[10] The liquid cell holder was used as a Faraday cup by loading it with a 0.3 mm thick laser-cut copper chip with a 0.5 mm hole in the center so that the beam can be made either to pass through un-scattered or fully absorbed by the copper plate for current measurement. The generated electron beam was initially passed through the center, and the resulting phosphor screen current as displayed by the TEM was recorded. Note that the readout is displayed as a current density rather than a current, assuming homogeneous illumination of the entire phosphor screen. The corresponding current was calculated by multiplying this readout by the screen area $A_s = \pi r_s^2$, where $r_s = 8$ cm. The sample holder was then moved so that the copper plate fully absorbs the beam for precise current measurement. Biasing the copper plate at +20 V minimized the loss of secondary electrons, affecting the measurement. The absorbed current was measured with a Keithley 2614B sourcemeter, $I_{true} = I_{beam_{on}} - I_{beam_{off}}$. The beam current

was varied in the range of 1-110nA, and the correction factor $f = I_{screen}/I_{meas} = 0.74 \pm$ 0.03 was extracted from a linear fit to the plot of phosphor against Faraday cup currents with an R^2 value of 0.997. The correction factor was used to calculate the actual primary current from hereon.

4.3.7 Secondary Electron coefficient

To calculate the SE coefficient (δ_{SE}), the screen (I_p) and the secondary emission current (I_{emit}) as measured by the sourcemeter currents were recorded when biases of $\pm$ 20 and 0 V were applied to the windows or holder. δ_{SE} was calculated by

$$\delta_{SE} = \frac{I_{emit}}{I_p} \tag{4.1}$$

4.3.8 AuNP Growth Analysis

The recorded movies were first aligned with ImageJ Linear Stack Alignment with the SIFT plugin and inverted in color to analyze the total AuNP growth. Similar to Section 3.4.2, a Python script was used to find and track the particles within each AAO microwell. As the aim was to assess the overall AuNP growth in the movie, I did not discard windows with minimal to no AuNP growth. The total hemispherical volume of AuNPs was calculated by:

$$V = \sum \frac{2}{3}\pi R^3 \tag{4.2}$$

with R as the radius of the AuNP.

4.3.9 Liquid Thickness

Following the acquisition of the AuNP growth in a region, I used a variation of the intensity ratio method as described in Azim *et al.* and shown in Section 2.3.5 to record the liquid thickness. This method is used in lieu of having EELS. In the case of the assembled AAO liquid cell, the original intensity ratio (Equation 2.14) method applicable for large area homogeneous samples does not apply since large angle scattered electrons would

add a significant background, altering the signal. Thus the two aperture apparent liquid thickness approach introduced in in Section 2.5.2.2 with Equation 2.34 was used.

$$t_{liquid} = \frac{log\left(r_{total}\right) - log\left(r_{win}\right)}{(1/\ell_2) - (1/\ell_1)}$$ (2.34)

where ℓ_2 and ℓ_1 are the mean free paths of electron scattering to angles beyond 8.75 mrad (522 nm) and 12.6 mrad (718 nm) in water, respectively. r_{total} and r_{win} are the mean intensities Int_1/Int_2 for the ℓ_1 and ℓ_2 images for the total liquid cell and 2 windows, respectively.

4.3.10   SERF Simulation

The LC window and beam-induced charge layer were simulated as a central circular disc (primary beam area) at a positive potential surrounded by an annulus at a different potential. The value and magnitude depend on the different cases considered in Figure 4.5. The disc and annulus were assumed to be conductors. The thickness and distance to the grounded plane, disc, and annulus are 10 nm, and outer radii are 1 μm and 50 μm, respectively. These are floating above and not in electrical contact with a conductive ground plate representing the liquid sample. For Si_3N_4 and carbon, a central disc potential of 2 V and 1 V were assumed, assuming that the insulating Si_3N_4 layer has a larger electrical breakthrough voltage than carbon. The corresponding assumed breakdown field strengths are in the order of 10^6 V/cm, which is realistic for thin film insulators, Si_3N_4 in particular.[200] The outer annulus region potential was in the range of -1 V to +1 V and -0.5 V to +0.5 V for Si_3N_4 and carbon, respectively.

An additional field of 0.04, 0, and -0.04 MV/m for positive, zero, and negative bias, respectively, was applied to account for external bias effects. The electric fields for the 6 different scenarios using the Poisson Superfish set of codes [201] were calculated. The electric fields were then fed into a particle tracking simulation using the ASTRA code [202] to predict the SEEF and SERF dynamics based on the model. The SE emission distribution was assumed to be spatially uniform over the central disc emission region

(radius 1 μm) with a transverse normalized emittance of 1 μrad·mm. A total of 100.000 particles were used for the simulations for good statistics. The energy distribution was assumed to be of the form [185]

$$\frac{dN_{SE}}{dE_{SE}} \propto \frac{1}{E_p} \frac{E_{SE}}{(E_{SE} + \phi_w)^4} \tag{4.3}$$

where the left hand side of the equation is the secondary electron distribution, E_p, E_{SE}, and ϕ_w are the primary electron energy, secondary electron energy and work function, respectively. The peak of this distribution is given by $E_{p,SE} = \phi_w/3$. An emission peak $E_{p,SE}$ at 3 eV, and cut-off at 50 eV were assumed. This distribution is considered a reasonable average of known SE emission energy spectra of various materials, although this equation applies only to metals [185].

4.3.11 Structural Similarity Index Measurement (SSIM) Calculation

Before and after recording the AuNP growth movie for 2 minutes with a beam diameter of 1.4 microns and camera pixel size of 0.34 nm, micrographs in focus and at a 4 micron defocus were acquired at a pixel size of 1.25 nm (10 K). These lower magnification micrographs are used to observe changes in the periphery of where the AuNP movie was acquired. A python script was used to calculate the SSIM value (from scikit-image). First, the micrographs were aligned to account for beam and stage drift. These images were used as is with skimage.metrics.structural_similarity. A representative area image showing the movie region was used as a mask for only the beam or the periphery.

4.4 Influence of Window Material on AuNP Growth

AuNP growth dynamics was chosen as the model system as it has been extensively investigated.[3, 25, 30, 148, 149, 150] As presented in Section 3.2.3, the formation of AuNPs requires a transfer of charge from the bulk radiolytic species to the $HAuCl_4$ precursor solution. The reduction of Au^{3+} predominantly occurs with e^-_{aq} due to its significant reduction potential (-2.9 V) compared to other reducing species such as hydrogen (H·) and hydroxide (OH$^-$) radicals at +1.8 and -2.3 V, respectively (Section 3.2.2). [155] Detailed

calculations by Schneider *et al.* suggest a dose rate dependence on the steady state concentration of these species.[3] The aim is to employ the AuNP growth as a reporter event for the influence of the window material and SE emission on radiolytic species at a constant dose rate.

To observe the nucleation and growth of AuNPs, I used the anodic aluminum oxide (AAO) support structures. The previous chapters demonstrate that this structure promotes even liquid distribution of the desired thickness over large fields of view by acting as a spacer support. In addition, they create individually-isolated liquid cells that are ideal for mitigating the migration of radiolytic species.[3, 111, 137, 203]

As for window materials, Si_3N_4 is the most commonly utilized window material in LC research and, therefore, an essential component of the study. Carbon, a commonly used substrate in conventional TEM, has been selected here as a cost-effective and easier to handle proxy for the more widely employed graphene LC approaches due to a growing interest in this window material.[35, 93] Si_3N_4 and carbon represent two major classes of materials, insulator and conductor, which exhibit different SE dynamics behavior through the alternate current flow and charge accumulation properties. Similar to the previous chapters, formvar (polyvinyl formal) was again included to showcase its versatility as a LC window.

Movies were recorded at a fixed dose rate of 24 $e^-/Å^2$s with an exposure time of 0.5 s per frame and a magnification corresponding to a camera pixel size of 0.34 nm. This was repeated and averaged for three regions in each assembled liquid cell. Each region contains roughly 20 AAO wells entirely in the field of view. These were selected for further analysis, while the partially cut-off wells on the edges were neglected. The growth of AuNPs in each of the selected wells was analyzed and averaged across the three regions. Following the image acquisition, additional images were recorded to estimate the apparent scattering liquid layer thickness following a procedure adapted from Azim *et al.* and introduced in Section 2.5.2.2 in which the mean image intensity at two objective apertures was recorded.[10] Representative TEM micrographs showcasing the AuNP growth are

depicted in Figure 4.3a.
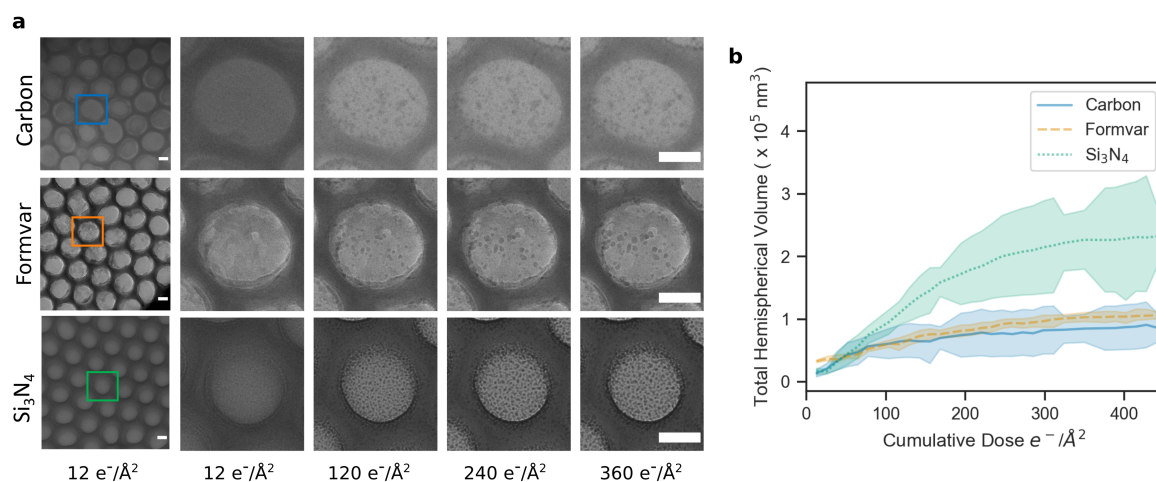
Figure 4.3: AuNP growth in assembled AAO liquid cells with Carbon, Formvar, and Si_3N_4 windows, in which no bias is applied. a) An overview of the imaging area at a cumulative dose of 12 e$^-$/Å^2 is shown in the left column, scale bar 50 nm. The AuNP growth in one AAO well, is highlighted with the colored box. The scale bar of the individual AAO well is 50 nm. b) Average total hemispherical volume of three regions with increased cumulative dose. Shaded regions represent the standard error of the mean.

From the micrographs in Figure 4.3a AuNP growth depends on the window material. In particular, Si_3N_4 exhibited particles of uniform size, whereas a broader size distribution was observed for the carbon and formvar windows. Similar to the previous chapter, bubble formation was not observed for carbon, Si_3N_4, and formvar windows (Figure 3.10). The total hemispherical AuNP volume present in the viewing region was calculated to compare the growth with the three window materials.[204] The results are shown in Figure 4.3b. It is apparent that the growth rate of total hemispherical volume with increasing dose is more significant for Si_3N_4 than carbon and formvar, which exhibit similar growth.

I observed instances of preferred growth at the AAO pore peripheries, possibly due to preferential in-scattering of SE at the Al_2O_3:liquid boundary.[191] The consistently observed high growth rate is followed by a plateau, likely due to dynamic equilibrium. Considering that minimal growth was observed between the individual wells, I regard the AAO as individually sealed liquid-cells.

Two parameters in the bulk liquid that could influence AuNP growth are the concentration of precursor solution and liquid thickness.[205, 206] The 20 mM $HAuCl_4$ solution was the same for all window assemblies. Wang *et al.* and Park *et al.* observed morphological differences when the liquid layer was thin ($<$ 250 nm) or thick ($>$ 1 µm).[25, 207] In Figure 4.3a, no morphological differences such as rods and spurs were observed. Furthermore, for the three liquid cell assemblies, the average liquid thickness of the AAO wells was 97 $\pm$ 18, 157 $\pm$ 4 nm, and 81 $\pm$ 8 nm for Si_3N_4, carbon, and formvar, respectively. I note that the variation of growth rates between individual wells is significantly lower for formvar. I hypothesize that this is related to higher homogeneity and material properties.

4.5 Electrical Bias Dependent Growth

The previous section established an apparent influence of the window material on the total hemispherical volume of Au. Scholz *et al.* reported how different escape depths of conductive and insulating materials directly influence the SE emission.[208] To investigate the influence that the SE emission, locally composed of SE escape flux (SEEF) and SE return flux (SERF), has on the radiolytic reduction of Au^{3+}, I applied a bias of -20 V, 0 V, and +20 V to the specimen relative to the holder held at ground potential. A schematic of the setup is shown in Figure 4.4a. The AuNP growth for no bias, negative bias, and positive bias are shown in Figure 4.4b. Table 4.1 contains the rate of growth up to a cumulative dose of 250 e$^-$/Å^2 as determined by a linear fit of Figure 4.4b

Table 4.1: Rate of Growth for Biased Windows

	-20 V	0 V	+20 V
Carbon	3.17	3.47	6.32
Formvar	4.20	5.03	5.49
Si_3N_4	11.60	12.13	12.93

When no bias is applied to the window materials (Figure 4.3b and Figure 4.4b, green line), the total hemispherical volume is the greatest for the insulating Si_3N_4 windows. In
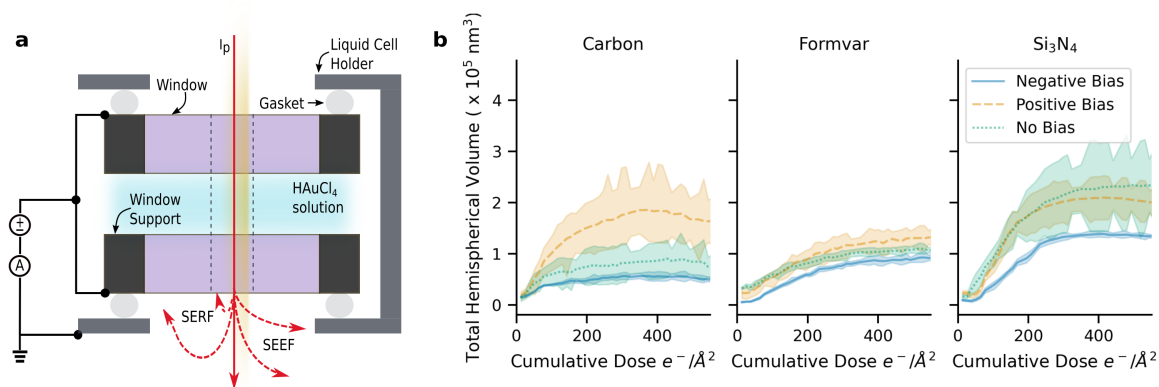
Figure 4.4: a) Schematic of the liquid cell holder with the ability to bias the window. b) Influence of bias on AuNPs total hemispherical volume for the three window materials: carbon, formvar, and Si_3N_4 when no bias and $\pm$ 20V were applied. Shaded regions represent the standard error of the mean between three runs.

contrast, the formvar and carbon grids exhibit a similar growth with increasing cumulative dose.

When I applied a bias of -20 V to the windows, there was a decrease in the growth and growth rate for carbon, Si_3N_4 and formvar (Figure 4.4b, blue line and Table 4.1). Remarkably at -20 V, the variation between runs for all windows decreased drastically. SERF, therefore not only increases AuNP growth but also significantly affects the spatial and temporal variation. A bias of +20 V resulted in a major increase in growth for the carbon windows (Figure 4.4b, orange line). For the Si_3N_4 and formvar windows, the +20 V bias did not significantly affect the total hemispherical volume. Overall it increased the rate of growth (Table 4.1). Furthermore, the positive bias resulted in increased inconsistent growth between runs.

The two aperture method measured the liquid thickness instead of EELS. The liquid thickness and standard error of the mean of the three regions are shown in table 4.2

I found a comparable average liquid thickness for the respective window materials for the no biased and biased runs. This eliminates the possibility that differences in thickness could account for different growth. The fact that the carbon LC assembly with the thickest liquid layer did not produce the greatest volume suggests that the window properties rather

Table 4.2: Average Liquid Thickness(nm) and Standard Error of Mean

Window	0 V	-20 V	20 V
Carbon	157 ± 4	154 ± 1	163 ± 12
Formvar	81 ± 8	92 ± 1	89 ± 5
Si_3N_4	97 ± 18	122 ± 6	108 ± 12

than the liquid thickness are instrumental to the AuNP growth.

4.5.1   SE Escape Coefficient

The current was measured following the biased movie acquisition to investigate if SEEF and/or SERF are attributable to the different growth profiles observed in Figure 4.4. The results of δ_{SE} are shown in Table 4.3.

Table 4.3: Secondary Electron Coefficient (δ_{SE})

	Carbon	Formvar	Si_3N_4
Bias (V)	δ_{SE}	δ_{SE}	δ_{SE}
0	25.2	0.4	1.6
-20	26.0	0.7	1.5
20	1.7	0.8	1.6

Higher δ_{SE} values correspond to more SEEF escaping towards the vacuum or being captured by the holder. The most prominent difference in AuNP growth with the application of a bias in Figure 4.4 was in the case of a carbon window, which is also reflected in the δ_{SE} values. With the application of a positive bias, the δ_{SE} value decreases by an order of magnitude, whereas a negative bias marginally increases δ_{SE}.

The δ_{SE} values for formvar and Si_3N_4 did not substantially vary with bias. This could be attributed to the insulating nature of these two windows. Although the formvar window was supported on a 3 mm copper TEM grid and silver paint was applied to the backside of the Si_3N_4, it is possible that not all of the SEEF was measured with this setup.

In insulating materials, it has been shown that the inelastic scattering of the primary beam results in δ_{SE} emission and charging of the window material.[154] Therefore I went

a step further to validate that the δ_{SE} of insulating materials can be influenced with an applied bias by measuring the δ_{SE} of one window without AAO. Again the window was biased, and the holder was grounded. The results are shown in Table 4.4. Initially, I could only measure the secondary emission current (I_{emit}) as measured by the sourcemeter with the conductive carbon window. A 5 nm layer of carbon was deposited onto the Si_3N_4 and the formvar window was coated with a monolayer of graphene to increase the conductivity of the insulating windows.

Table 4.4: The δ_{SE} for One Window.

Bias	Carbon	Si_3N_4	Si_3N_4-Carbon	Formvar-Graphene
0 V	0.15	0	0.81	0.79
-20 V	1.39	0	2.13	1.88
20 V	0.09	0	0.12	0.05

Adding a conductive layer to the insulating materials allowed for the δ_{SE} calculation (Equation 4.1). In all cases, the δ_{SE} was the greatest with a negative bias and the lowest when a positive bias was applied to the window. This shows that the window material and bias influence δ_{SE}.

4.5.2 Description of the Model

In order to understand the bias dependence of SE emission (Table 4.3) and Au growth from Figure 4.4b, a model was developed (Figure 4.5) that describes the SE dynamics based on the window properties and external bias. Due to the current window thicknesses being larger than the SE escape depths, the influence of window thicknesses is not considered.[193]

Since primary beam current (I_p) exposure results in positive window charging due to SE emission, the illuminated region is always positively charged. [154, 187, 188, 189, 209] The global specimen pre-exposure from beam alignments causes the surrounding annular region to initially exhibit a positive charge. Charging also occurs for nominally conductive
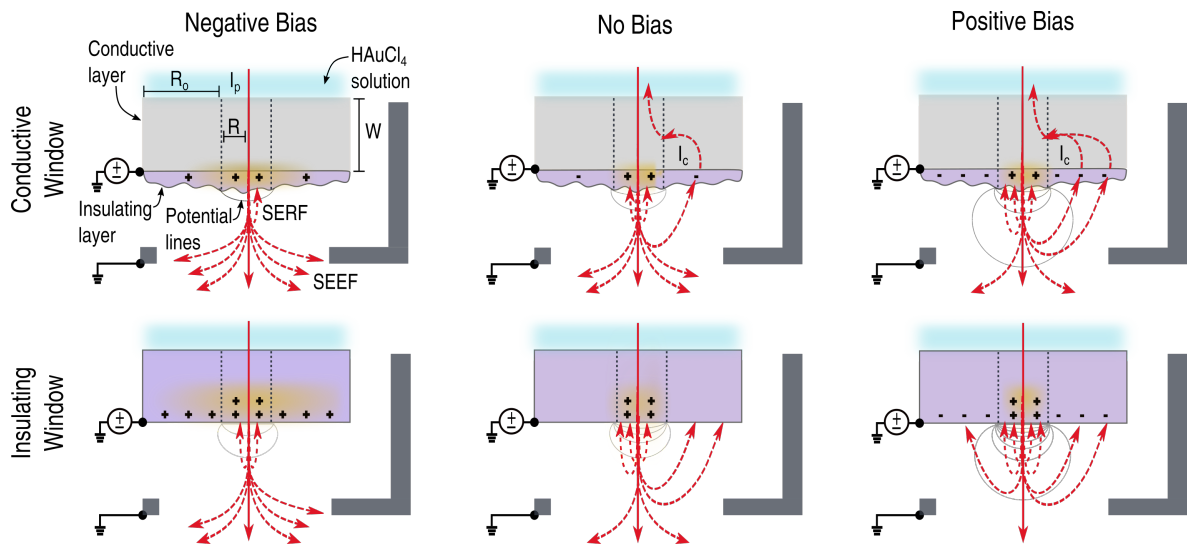
Figure 4.5: Schematic of the SE return flux (SERF), escape flux (SEEF), and potential lines in the conductive (gray) and insulating (purple) window materials in the case when a negative bias (left column), zero bias (middle column) and positive bias (right column) is applied to the LC assembly and the outside holder is set to ground and based off of the simulation parameters: beam radius (R) of 1 μm, annulus (R_o) of 50 μm, window height (W) of 10 nm. Also shown is the radial conduction (I_c) from the returning electrons.

materials such as carbon due to the buildup of an insulating contamination layer on the surface.[210] In the case of carbon, this causes a slightly positive and negative charging inside and outside the illuminated region, respectively.[195, 211, 212] Si_3N_4 is qualitatively similar to carbon in terms of charging effects; the difference lies mainly in the magnitude. The combined charge states of the center and annular region result in an electric field that affects the SEEF and SERF.

In a negative bias, both conductive and insulating windows exhibit very little SERF in the annular region. Thus, the initial positive charge is preserved, damping the retention electric field due to the highly charged center. This results in increased SEEF and a decrease in solvated electrons. Due to more charging in the insulating window, the SEEF is larger with the conductive window, as shown in Table 4.3. This model explains not only the reduced growth but also the low variation between runs with negative bias in Figure 4.4 as the effect of SERF electrons, which are highly sensitive to locally changing surface properties, are suppressed.

In case of no bias, some SERF is attracted to the positively charged annular region,

resulting in partial or complete neutralization. As a result, the retention electric field in the center region is no longer damped, resulting in reduced SEEF. Additionally, in the case of the conductive window, some SERF from the annular region is conducted back to the center through radial currents (I_c) in the window material[188, 213], resulting in more AuNP growth (Figure 4.4 Carbon).

In turn, a positive bias leads to an even larger SERF in the annular region and negative charging; this, in turn, leads to an enhancement of the center electric field and further reduction of SEEF as measured by δ_{SE}(Table 4.3), and concomitant enhanced AuNP growth. The enhanced radial return current in the conductive window and the more efficient distribution of external bias potential could explain the relatively large growth enhancement seen for the positively biased carbon LC in Figure 4.4. Considering this, applying positive and negative biases would significantly influence a highly conductive graphene window.

Loh *et al.* and Tan *et al.* reported an increase in $AuCl_4^-$ concentration at positively charged Si_3N_4 surfaces.[148, 214] This concentration gradient of precursor ions leads to increased growth at the window-liquid interface.[148, 205, 206, 214] Mehdi *et al.* attributed this to an increasing electric field at the window: liquid interface.[215] Therefore for the conductive and insulating window materials presented here, it is proposed that the difference in growth observed in Figure 4.4 is due to different charging properties, SEEF, and SERF.

4.5.3 Simulating the Surface Electric Field and SERF

In order to quantify the predictions of the model, electric field calculations and particle tracking simulations were performed. Briefly, the SE emission (SEE) region was modeled as a circular patch with a 1 μm radius held at a constant positive potential, surrounded by a large annular region with a varying charge depending on the different cases 1 a-c and 2 a-c in Figure 4.6

Figure 4.6 1 a-c and 2 a-c depict the simulated SERF for negative (a), zero (b), and positive (c) bias. The potential magnitude in the center (irradiated) region and surrounding annulus was set larger in the case of the insulating window compared with the conductive
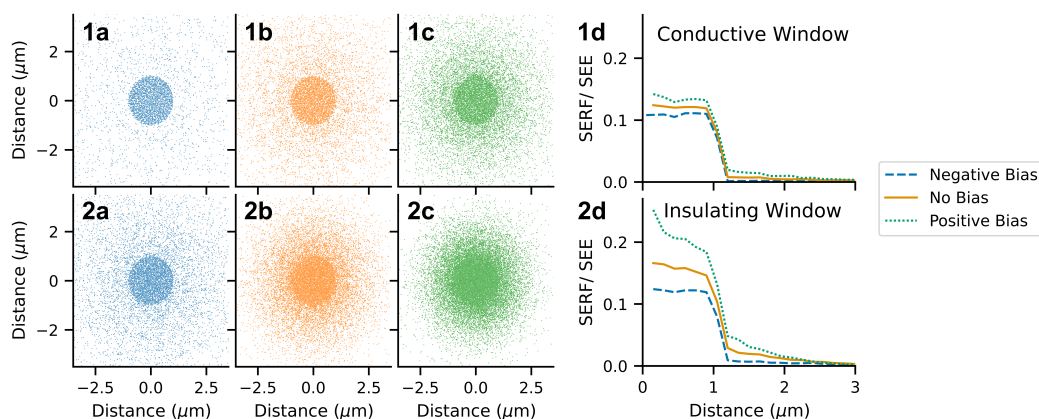
Figure 4.6: Simulated SERF for conductive (1) and insulating windows (2). a-c depict the simulated SERF for negative, zero, and positive bias, respectively. 1d and 2d are the corresponding radial histograms from the center to 3 μm for conductive and insulating windows, showcasing the ratio of SERF to SEE particle density.

one. Setting the annulus potential negative, zero, and positive, corresponding to positive, zero, and negative annulus bias, yields the SERF scatter plots in Figure 4.6 a-c. SERF is significantly higher in all insulating window regions than in conductive window. Also, an increasing positive bias increases SERF in both the center and annulus regions. The radially averaged histograms (Figure 4.6d) depict the fraction of SERF from the total initial SE emission current density (SEE) at the plane of emission (SERF/SEE). A significant proportion between 0.1 - 0.25 occurs in the central region for all cases, with an increase in SERF with increasing positive bias in both the center and annular region up to 3 μm. The simulated potential maps are represented in the SERF/SEEF schematic (Figure 4.5). The depth of the electron retaining potential increases with increasing positive bias and is also deeper for the insulating window than the conductive one, with a corresponding effect on the SERF. The simulations are thus in line with the window material and bias dependent AuNP growth results, assuming 1) that SERF increases the concentration of solvated electrons in the liquid layer and 2) that the radial currents (I_c) increase with conductivity (Figure 4.5).

4.5.4 SE Return Flux (SERF) Outside of the Beam

The model relies on the balance between SEEF and SERF, with both occurring inside the beam and only SERF outside the region of illumination. The previous δ_{SE} measurements show that both the SEEF (Table 4.3) and AuNP growth (Figure 4.4 B) vary between window material and applied bias. However, due to the design of the liquid cell holder, direct measurement of SERF inside and outside of the beam was not possible.

Images with lower magnification (larger field of view) at 1.25 nm pixel size (10.000 nominal magnification) were acquired before and after recording the AuNP growth for two minutes at high magnification (pixel size of 0.34 nm, 40.000 nominal magnification) at a dose rate of 24 e$^-$/Å^2. After the movie acquisition, a high magnification image was acquired of AAO wells both inside and outside of the originally illuminated area. This procedure was to qualitatively investigate SERF outside of the beam. Representative micrographs for Carbon and Si$_3$N$_4$ are shown in Figure 4.7.
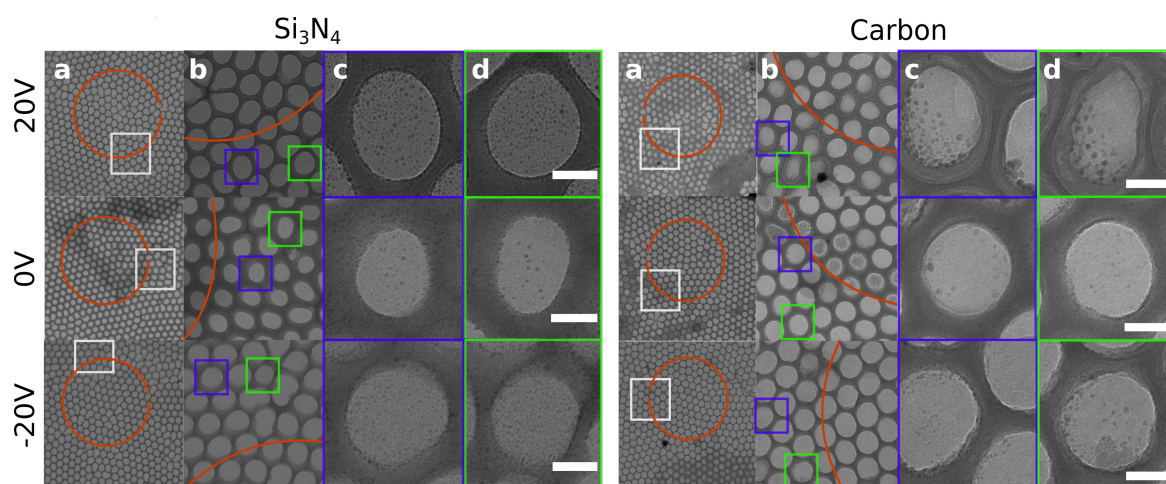
Figure 4.7: a)AuNP growth after two minutes of irradiation in an Si$_3$N$_4$ and Carbon liquid cell. The red circle represents the periphery of the beam. The white box represents the region inside and outside of the beam. Micrographs of the respective regions are shown in column b, while representative AAO wells are displayed in columns c and d. The scale bar represents 50 nm in all instances.

Column a, depicts the periphery of the beam (red line) and a region selected to showcase

AAO wells inside and outside the beam (white box). A high magnification image of this region is shown in column b. Representative AAO wells are shown in columns C and D to highlight the growth outside the beam. Growth is observed outside the irradiated region with both window materials and all biases (red circle). Furthermore, in the case of Si_3N_4, the polydispersity of the particle size increases outside of the irradiated area.

The resolution of the lower magnification (1.25 nm pixel size) before and after images did not allow for individual particle picking as previously carried out. Therefore to determine if particle growth occurred further beyond the beam, a Structural Similarity Index Measurement (SSIM) was calculated based on the luminance, contrast, and structure of the before and after images. This was repeated for three regions.[216] The averaged values ranging from 0 to 1 were calculated, with 1 corresponding to no change between the two images. [217] The SSIM results are shown in Table 4.5.

Table 4.5: SSIM Values for Carbon and Si_3N_4 In-focus Images

	(V)	Beam	Periphery	Whole Area
Carbon	0	0.783 ± 0.019	0.288 ± 0.018	0.058 ± 0.011
	-20	0.771 ± 0.006	0.290 ± 0.010	0.053 ± 0.008
	20	0.772 ± 0.013	0.275 ± 0.020	0.041 ± 0.012
Si_3N_4	0	0.710 ± 0.003	0.368 ± 0.007	0.052 ± 0.007
	-20	0.701 ± 0.002	0.373 ± 0.005	0.043 ± 0.001
	20	0.731 ± 0.015	0.336 ± 0.021	0.042 ± 0.002

Following two minutes of irradiation at 24 e$^-$/Å^{2}s a bias of 20 V resulted in the most change in the periphery, followed by 0 V and -20 V for the Si_3N_4 and Carbon windows. Growth outside the region of illumination has been observed for Ag nanoparticles and metal-organic frameworks (MOFs) between two Si_3N_4 windows.[38, 160] In these cases, the growth was attributed to the diffusion of radical species. As the simulations (Figure 4.6) show SERF/SEE beyond the beam and the AAO are considered to act as individually sealed micro-wells, it is proposed SERF plays a more significant role than diffusion. Therefore these results serve as a qualitative basis that the proposed model that AuNP growth

increases with SERF and bias is plausible.

4.6 Gated AuNP Growth

The previous section verified the sample bias dependence of AuNP growth, and a model was presented that predicts bias dependent variation of SEEF and SERF that agrees qualitatively with observed emission currents and AuNP growth. However, there was no direct measurement of the proposed electrostatic fields resulting from charge buildup. To provide additional proof for the correlated modulation of AuNP growth and SEEF/SERF, I implemented a setup allowing for a more direct study, as illustrated in Figure 4.8. Instead of the bias modulation of long range SE emission escaping in the vacuum, this structure allows for active control of large electric fields within the Si_3N_4 window itself through a 5 nm carbon layer deposited on the vacuum-facing side of the window.[187] A standard 3 mm carbon TEM grid was used to seal the assembly at the top side. The entire assembly was biased at 10 V relative to the ground to minimize the SEEF on both the carbon and the C-Si_3N_4 side. Electric field modulations in the Si_3N_4 layer were achieved by applying a bias of 10 ± 1 V (9 V, 10 V, and 11 V) to the carbon coating resulting in the biases of $V_A = V_B$, $V_A < V_B$, and $V_A > V_B$, respectively. As before, I measured the AuNP growth, liquid thickness and calculated the total hemispherical volume. Figure 4.9 depicts the results.
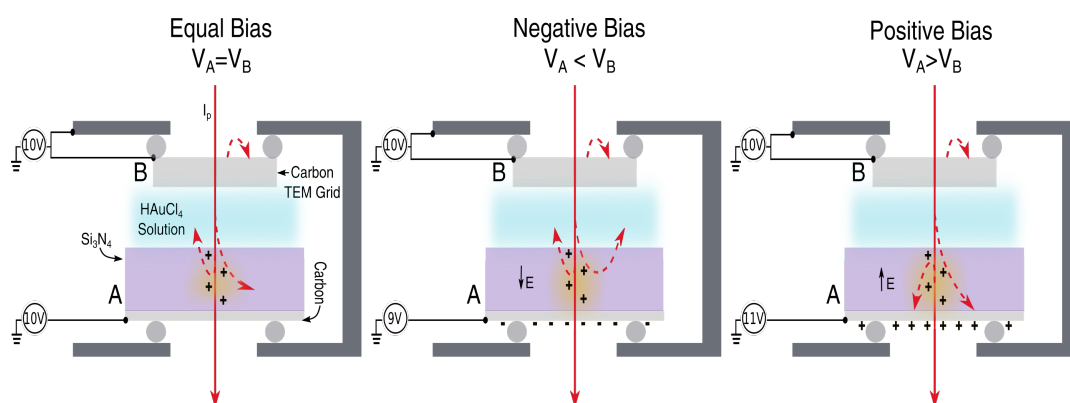
Figure 4.8: AuNP growth from biased gating. Electrical hookup for modulating AuNP growth for the different biases and schematic of suggested SE electron paths in response to different applied gating voltages.
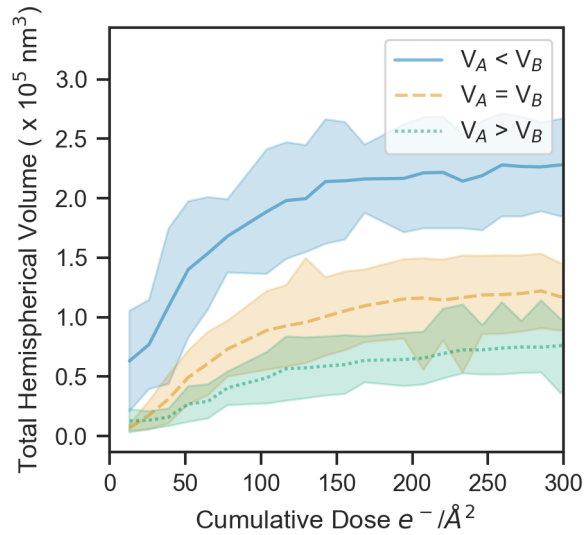
Figure 4.9: Total hemispherical volume with an increased cumulative dose for AuNP grown by modulating the bias applied to the C-Si$_3$N$_4$ window. The carbon TEM grid and holder were kept at 10 V, whereas the C-Si$_3$N$_4$ window was either equally biased, negatively or positively biased towards carbon or $V_A = V_B$, $V_A < V_B$, and $V_A > V_B$, respectively.

The average liquid thickness within the AAO wells was 166 $\pm$ 13, 166 $\pm$ 11, and 180 $\pm$ 6 for $V_A = V_B$, $V_A < V_B$, and $V_A > V_B$, respectively. This again ensures that the observed trends are not due to liquid layer fluctuations. Relative to $V_A = V_B$, setting $V_A < V_B$ and $V_A > V_B$ increased and decreased growth, respectively. This implies modulation of the SEEF and SERF at the liquid: Si$_3$N$_4$ boundary. Consider the equal bias case (Figure 4.8); SE emission in the Si$_3$N$_4$ layer leads to electron depletion and positive charging until an equilibrium between SE flux from liquid to Si$_3$N$_4$ and vice versa is reached. Applying a relative negative bias at the carbon gate electrode results in an additional electric field in the Si$_3$N$_4$, directing a portion of SE generated in the Si$_3$N$_4$ layer into the liquid layer. Similarly, some SE injected from the liquid layer into the Si$_3$N$_4$ are directed back into the liquid layer, leading to an increased reduction of Au^{3+} ions. For the positive bias case, SE generated in the Si$_3$N$_4$ are less likely to be injected into the liquid layer due to the applied electric field attracting electrons to the carbon gate electrode. Also, SE injected from the liquid layer into the Si$_3$N$_4$ are less likely to return. The Au growth curves in Figure 4.9 clearly show the expected differences subject to the applied biases.

Previously the SEEF was measured by the SE current (I_{SE}) leaving the window and going into the vacuum was measured. With this setup, the aim was to determine the SE generated from the bulk (I_L). A schematic of the electrical circuit is in Figure 4.10.
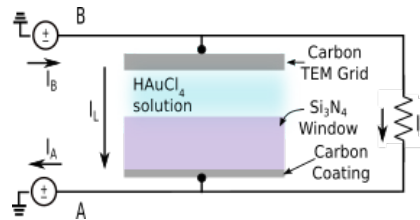
Figure 4.10: Equivalent electrical circuit diagram of the gated growth assembly. I_B, I_A, I_L, I_S are the measured currents of sourcemeter B, sourcemeter A, SE current across the illuminated C-Si$_3$N$_4$ window area, and current through the assembly leakage resistance, respectively.

As the assembly acts as a closed gate, it is possible to calculate the SE currents from the bulk liquid (I_L) through,

$$I_L = I_{L_B} + I_{L_A} \tag{4.4}$$

with I_{L_B} and I_{L_A} as the SE currents from the bulk due to the carbon and C-Si$_3$N$_4$ windows, respectively. These values are calculated from the measured SE current when the beam was on and off,

$$I_B = I_{L_B} + I_{S_B} \tag{4.5}$$

and

$$I_A = I_{L_A} + I_{S_A} \tag{4.6}$$

where I_A or I_B and I_{S_A} or I_{S_B} are the SE current with and without the beam, respectively.

I_L values of -0.51, -1.41, and 0.84 were calculated for $V_A = V_B$, $V_A < V_B$ and $V_A > V_B$, respectively.

The calculated I_L still highlights an increase and decrease in SE leaving the bulk when V_A

$> V_B$ and $V_A < V_B$, respectively. This follows the proposed SE schematic shown in Figure 4.8. However, a strong background current (I_A) was measured in all cases. Therefore, these results only represent the possibilities with this hookup and further measurements are required to comment on the SE generated from the bulk.

4.7 Conclusion

Herein the commercially available AAO sheet allowed for the removal of difficult nano-fabrication steps required for nano-well fabrication. I again showed that the AAO adheres to carbon, formvar, and Si_3N_4 windows, and again that formvar is a suitable window material for 3 mm liquid cells. The beam induced radiolysis with the three LC assemblies revealed that the window conductivity influences the total AuNP hemispherical volume, with increasing conductivity decreasing AuNP growth. Therefore these results affirm the use of conductive window materials to mitigate adverse beam effects.

Through biasing the window, I demonstrated the ability to increase or decrease AuNP growth. Although biases most influenced the conductive carbon window, generally, a bias of 20 V increased the growth, and -20 V decreased the total hemispherical AuNP volume and decreased the variation between runs. The ability to bias the LC holder will allow for improved control of future LC experiments. The custom-made liquid cell holder also allowed for the measurement of δ_{SE}. Although the δ_{SE} was low for the insulating windows, carbon showed a decrease by an order of magnitude with the application of a positive bias. I attributed the variations in total hemispherical volume with different window materials and biases to the balance between SERF and SEEF. This was confirmed through the model and simulations that depict an increase in SERF within and outside the beam region. The micrographs outside the beam annulus and SSIM qualitatively validated that the increase in SERF can increase growth due to more reducing species in the bulk.

With the carbon: Si_3N_4-carbon coated LC assembly I controlled electric fields within the Si_3N_4 window and modulation of AuNP growth. Furthermore, I determined that applying a bias is a viable way to modulate beam induced AuNP growth, implying that LCs, in general, can be treated as an electrochemical cell. I note that surface effects and

the different nucleation barriers in the three window materials complicate AuNP growth. However, I have focused on the growth of AuNPs that provides information on the excess solvated/reducing, electron conditions in the near surface region. Overall, these results can serve as a template for future LPEM experiments and exemplify that the window material must be considered when investigating or mitigating sample damage or beam induced radiolysis in the bulk.

5. Summary and Outlook

Overall, this work aimed to characterize the influence of the beam and window material on liquid phase electron microscopy (LPEM) experiments. This was motivated by window bulging, uncontrollable liquid layer, tedious nano-fabrication steps, and inelastic scattering events limiting LPEM research, even after more than 20 years of development. I focused my project on two areas to circumvent these issues: 1) the fabrication of innovative liquid cell architectures and 2) using gold nanoparticle (AuNP) growth as a probe for inelastic scattering byproducts raging within LPEM: radiolysis and the often overlooked secondary electron escape and return.
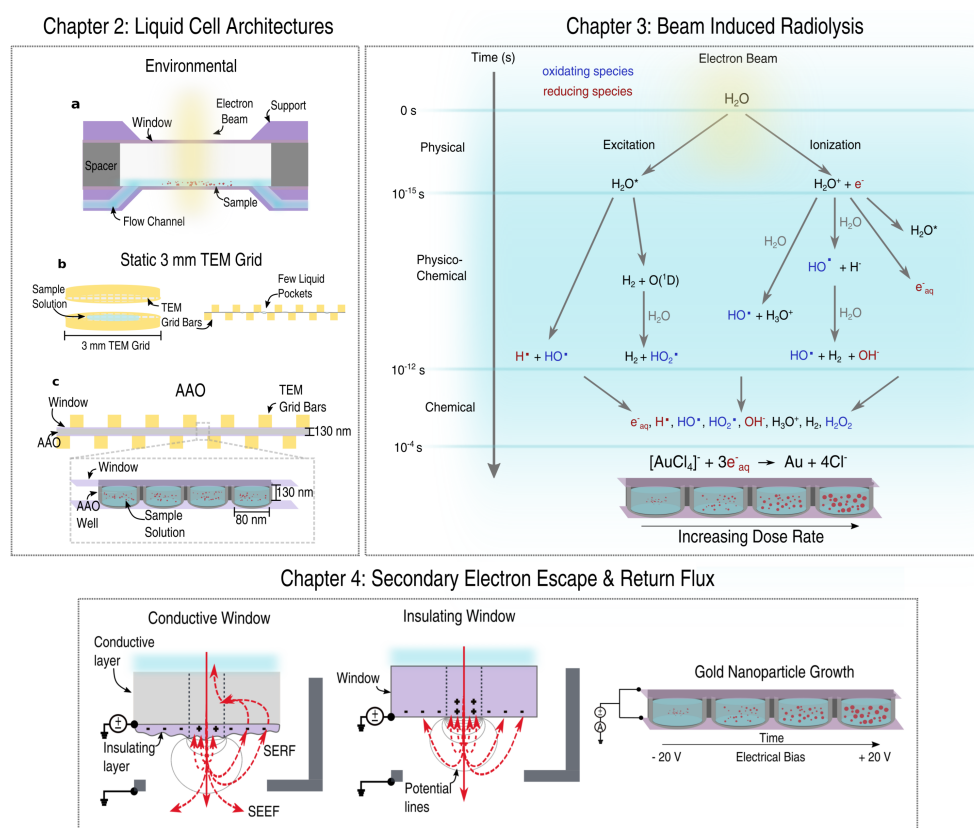
Figure 5.1: Summary of presented work: Chapter 2 introduced novel liquid cell architectures: the environmental liquid cell and AAO liquid cells with formvar and carbon windows. Chapter 3 used gold growth to probe beam induced radiolysis. Chapter 4 described the influence of window material and the secondary electron escape and return flux on AuNP growth.

To begin, I developed new liquid cell assemblies in Chapter 2 that tackled: 1) window bulging, 2) uncontrollable liquid layer, and 3) accessibility of LPEM. The first LC architecture, the environmental liquid cell (ELC), controlled the liquid layer by adjusting the pressure and flow. The implemented nanofluidics was showcased by PNIPAM NGs containing a silica core. The PNIPAM NGs collapsed around the core when dehydrated and extended outwards upon hydration. Usually, with Si_3N_4 LC architectures, window bulging restricts the image acquisition to the periphery of the windows and decreases the available imaging footprint. This chapter showcased how the ELC circumvents this. Here a thin liquid layer forms on one window thanks to the addition of a 10 μm Kapton spacer and increasing the hydrophilicity of one window. By focusing the beam on the liquid layer, the whole 200 x 30 x 0.2 μm window can be imaged. In lieu of electron energy loss spectroscopy (EELS), I demonstrated a good agreement between different ways to determine thickness: parallax, the ratio of image intensities, and computed values from a Monte Carlo simulation. Within the ELC, I calculated stable liquid layers ranging from 160 - 340 nm and showed that spatial resolution improves with decreased liquid layer thickness. The ELC is a promising tool to elucidate the structure-dynamic relationship between molecules. However, as novel and promising this method is, it requires a special holder and LC chips. Therefore it is not accessible to the larger LPEM community.

I addressed this in the second part of the chapter with static LCs from two 3 mm TEM grids. Conventionally these LCs are prepared with monolayer to multi-layer graphene films covering the grids. The graphene coating is expensive in terms of fabrication time and cost. I overcame this by using in-house prepared formvar films via the lesser utilized drop method and commercial carbon grids. I demonstrated for the first time that formvar films could be used for static LCs with average liquid thicknesses of 190 $\pm$ 11 nm. Window bulging is not an issue with these configurations. However, a significant amount of time was spent finding the pockets of liquid. This is a major downside that is not present with Si_3N_4 configurations. I investigated confined micro-wells as a way to avoid sporadic liquid pockets. I circumvented tedious nano-fabrication and lithography steps by adding anodic

aluminum oxide (AAO) films as a spacer between the two windows. The results of the 3 mm static formvar and carbon LCs were generally favorable, which led me to use these as window materials instead of graphene. A two aperture approach for liquid thickness determination was derived to account for the excessive scattering by the AAO film. The AAO LCs had liquid layers under 150 nm. The presence of liquid was also confirmed by the growth of gold nanoparticles (AuNP). These results confirm that the universal formvar and carbon AAO micro-well liquid cells are viable additions to the current LC architectures.

With the novel AAO liquid cells, I investigated the electron beam's interaction with the liquid and sample. Chapters 3 and 4 use AuNP growth as a probe for the radiolysis and secondary electron escape and return. Within LPEM, AuNP growth proceeds by reducing Au^{3+} to Au^0 via e^-_{aq}. Within Chapter 3, I used formvar, carbon, Si_3N_4, and graphene coated Si_3N_4 AAO LC configurations. I demonstrated two methods for picking and tracking particle growth. The concentration of radical species from the radiolysis of the aqueous environment increases with dose rate. In turn, I observed the total number and area of AuNP to increase with dose rate. These results confirm that adjusting the dose is a viable option to mitigate beam induced radiolysis. Coating the inside of the Si_3N_4 LC with graphene resulted in bubble generation within the AAO wells. This demonstrated that the AAO LC assembly produces individually isolated LCs that act as chemical nanochambers.[3, 111, 137, 203] Furthermore, the bubble generation supports the theory that graphene is not chemically inert and that first, graphene scavenges hydroxyl radicals, producing bubbles comprised of O_2, which scavenges e^-_{aq}. Additionally, the results indicated that the average growth rate with increasing dose followed a power law dependency similar to the concentration of e^-_{aq}. The liquid layer only influenced the total number and area of AuNP, not the growth rate. This implied that other factors besides radiolytic species (e^-_{aq}) must influence the AuNP growth. The precursor of e^-_{aq} are SE. Therefore the generation and dynamics of SE will influence e^-_{aq}.

Chapter 4 examined the influence and importance SE escape and return have on AuNP growth dynamics. I executed a systematic study of AuNP growth at a dose rate of 24

e$^-$/Å^{2}s with Si$_3$N$_4$, carbon, and formvar AAO LCs. Carbon and Si$_3$N$_4$ windows exhibit conductive and insulating properties, respectively. I revealed that window conductivity influences the total AuNP growth. Increasing the window conductivity resulted in decreased growth. Therefore, using a conductive window could be a means to mitigate adverse beam effects. By applying an electrical bias to the windows, I could increase or decrease the AuNP growth dynamics. Generally, a bias of 20 V increased, and -20 V not only decreased the growth but also lowered the variation between runs. This phenomenon was greatest with the conductive carbon window. Additionally, with the custom-made LC holder I measured the secondary electron coefficient (σ_{SE}) and showed in the case of carbon under a positive bias a decrease by an order of magnitude. I attributed the variation in growth to be from the balance of SE escape flux (SEEF) and SE return flux (SERF). A model was developed to describe these processes and confirmed with simulations. In general, a positive bias increases SERF within and outside the beam region. This causes an increase in bulk reducing species and growth. I qualitatively confirmed this with the increased growth outside the beam region with a positive bias. Finally, a way to control the electric fields with a carbon:Si$_3$N$_4$-carbon coated LC assembly was presented. Applying a bias allowed for easy modulation of AuNP growth. However, one area that requires further investigation is the different nucleation barriers of the window materials and how this impacts AuNP growth, SEEF, and SERF. In general, these results showcased that every LC can and should be treated as an electrochemical cell.

Overall within this work, I introduced three novel liquid cell architectures and showcased how dose rate and window material influence AuNP growth dynamics. I elucidated the role the electron beam has on the solution, sample, and window by focusing on radiolysis and secondary electrons. The results affirm AuNP growth is a suitable probe for these interactions. The chapters demonstrate formvar as a suitable window material. Additionally that with carbon LCs there is decreased AuNP growth and no bubble formation. Overall, the most striking finding was the window material's impact on the secondary electron escape and return flux. The results presented throughout can be used as templates for additional LPEM

experiments. LPEM studies will likely continue to combine various LC architectures and window materials. For example, new window materials, incorporating microfluidics, relying on multi-well designs, and the possibility of electrical hookups.[218] Projects will incorporate pre- and post-analysis methods to correlate the *in situ* LPEM results with analytical capabilities, such as fluorescence microscopy, MALDI, mass spectrometry, Raman, and AFM.[1, 45, 175, 219] Finally, to elucidate samples in their native environment, LPEM will apply even more advanced image analysis, machine learning, and AI techniques.[220, 221] Regardless of potential LPEM advancements, in one form or another, the interaction of the electron beam with the solution, sample, and window will remain.

REFERENCES

[1] S. Pu, C. Gong, and A. W. Robertson, "Liquid cell transmission electron microscopy and its applications," *Royal Society open science*, vol. 7, no. 1, p. 191204, 2020.

[2] S. M. Rehn and M. R. Jones, "New strategies for probing energy systems with in situ liquid-phase transmission electron microscopy," *ACS Energy Letters*, vol. 3, no. 6, pp. 1269–1278, 2018.

[3] N. M. Schneider, M. M. Norton, B. J. Mendel, J. M. Grogan, F. M. Ross, and H. H. Bau, "Electron–water interactions and implications for liquid cell electron microscopy," *The Journal of Physical Chemistry C*, vol. 118, no. 38, pp. 22373–22382, 2014.

[4] J. Polte, "Fundamental growth principles of colloidal metal nanoparticles–a new perspective," *CrystEngComm*, vol. 17, no. 36, pp. 6809–6830, 2015.

[5] E. Ruska, "The development of the electron microscope and of electron microscopy. nobel lectures. physics 1981-1990 (frngsmyr t. & ekspng g. eds)," 1986.

[6] H. Kohl and L. Reimer, *Transmission Electron Microscopy*. Springer, 2008.

[7] R. Ross, *Liquid Cell Electron Microscopy*. Advances in Microscopy and Microanalysis, Cambridge University Press, 2016.

[8] M. K. Monninger, C. A. Nguessan, C. D. Blancett, K. A. Kuehl, C. A. Rossi, S. P. Olschner, P. L. Williams, S. L. Goodman, and M. G. Sun, "Preparation of viral samples within biocontainment for ultrastructural analysis: Utilization of an innovative processing capsule for negative staining," *Journal of virological methods*, vol. 238, pp. 70–76, 2016.

[9] R. S. Dillard, C. M. Hampton, J. D. Strauss, Z. Ke, D. Altomara, R. C. Guerrero-Ferreira, G. Kiss, and E. R. Wright, "Biological applications at the cutting edge of cryo-electron microscopy," *Microscopy and Microanalysis*, vol. 24, no. 4, pp. 406–419, 2018.

[10] S. Azim, L. A. Bultema, M. B. de Kock, E. R. Osorio-Blanco, M. Calderón, J. Gon-

schior, J.-P. Leimkohl, F. Tellkamp, R. Bücker, E. C. Schulz, *et al.*, "Environmental liquid cell technique for improved electron microscopic imaging of soft matter in solution," *Microscopy and Microanalysis*, vol. 27, no. 1, pp. 44–53, 2021.

[11] S. Giorgio, S. Sao Joao, S. Nitsche, D. Chaudanson, G. Sitja, and C. Henry, "Environmental electron microscopy (etem) for catalysts with a closed e-cell with carbon windows," *Ultramicroscopy*, vol. 106, no. 6, pp. 503–507, 2006.

[12] J. Wu, H. Shan, W. Chen, X. Gu, P. Tao, C. Song, W. Shang, and T. Deng, "In situ environmental tem in imaging gas and liquid phase chemical reactions for materials research," *Advanced Materials*, vol. 28, no. 44, pp. 9686–9712, 2016.

[13] S. Hui and D. Parsons, "Electron diffraction of wet biological membranes," *Science*, vol. 184, no. 4132, pp. 77–78, 1974.

[14] M. Williamson, R. Tromp, P. Vereecken, R. Hull, and F. Ross, "Dynamic microscopy of nanoscale cluster growth at the solid–liquid interface," *Nature materials*, vol. 2, no. 8, pp. 532–536, 2003.

[15] S. Besztejan, S. Keskin, S. Manz, G. Kassier, R. Bücker, D. Venegas-Rojas, H. K. Trieu, A. Rentmeister, and R. J. D. Miller, "Visualization of cellular components in a mammalian cell with liquid-cell transmission electron microscopy," *Microscopy and Microanalysis*, vol. 23, no. 1, p. 46–55, 2017.

[16] D. B. Peckys, G. M. Veith, D. C. Joy, and N. De Jonge, "Nanoscale imaging of whole cells using a liquid enclosure and a scanning transmission electron microscope," *PloS one*, vol. 4, no. 12, p. e8214, 2009.

[17] C. Mueller, M. Harb, J. R. Dwyer, and R. D. Miller, "Nanofluidic cells with controlled pathlength and liquid flow for rapid, high-resolution in situ imaging with electrons," *The Journal of Physical Chemistry Letters*, vol. 4, no. 14, pp. 2339–2347, 2013.

[18] S. Keskin and N. de Jonge, "Reduced radiation damage in transmission electron microscopy of proteins in graphene liquid cells," *Nano Letters*, vol. 18, no. 12, pp. 7435–7440, 2018.

[19] J. S. Bunch, S. S. Verbridge, J. S. Alden, A. M. Van Der Zande, J. M. Parpia, H. G.

Craighead, and P. L. McEuen, "Impermeable atomic membranes from graphene sheets," *Nano letters*, vol. 8, no. 8, pp. 2458–2462, 2008.

[20] C. Lee, X. Wei, J. W. Kysar, and J. Hone, "Measurement of the elastic properties and intrinsic strength of monolayer graphene," *science*, vol. 321, no. 5887, pp. 385–388, 2008.

[21] S. W. Chee, S. H. Pratt, K. Hattar, D. Duquette, F. M. Ross, and R. Hull, "Studying localized corrosion using liquid cell transmission electron microscopy," *Chemical Communications*, vol. 51, no. 1, pp. 168–171, 2015.

[22] F. M. Ross, "Opportunities and challenges in liquid cell electron microscopy," *Science*, vol. 350, no. 6267, 2015.

[23] H.-G. Liao, K. Niu, and H. Zheng, "Observation of growth of metal nanoparticles," *Chemical Communications*, vol. 49, no. 100, pp. 11720–11727, 2013.

[24] S. Azim, *Development, characterization and application of in-liquid electron imaging and diffraction techniques for high-resolution structural analysis*. PhD thesis, Staats- und Universitätsbibliothek Hamburg Carl von Ossietzky, 2020.

[25] J. H. Park, N. M. Schneider, J. M. Grogan, M. C. Reuter, H. H. Bau, S. Kodambaka, and F. M. Ross, "Control of electron beam-induced au nanocrystal growth kinetics through solution chemistry," *Nano letters*, vol. 15, no. 8, pp. 5314–5320, 2015.

[26] X. Chen, L. Zhou, P. Wang, H. Cao, X. Miao, and F. Wei, "A study of electron beam induced deposition and nano device fabrication using liquid cell tem technology," *Chinese Journal of Chemistry*, vol. 32, no. 5, pp. 399–404, 2014.

[27] L. Lu, G. Burkey, I. Halaciuga, and D. V. Goia, "Core–shell gold/silver nanoparticles: Synthesis and optical properties," *Journal of colloid and interface science*, vol. 392, pp. 90–95, 2013.

[28] H. Zheng, R. K. Smith, Y.-w. Jun, C. Kisielowski, U. Dahmen, and A. P. Alivisatos, "Observation of single colloidal platinum nanocrystal growth trajectories," *science*, vol. 324, no. 5932, pp. 1309–1312, 2009.

[29] J. E. Evans, K. L. Jungjohann, N. D. Browning, and I. Arslan, "Controlled growth

of nanoparticles from solution with in situ liquid transmission electron microscopy," *Nano letters*, vol. 11, no. 7, pp. 2809–2813, 2011.

[30] T. J. Woehl, J. E. Evans, I. Arslan, W. D. Ristenpart, and N. D. Browning, "Direct in situ determination of the mechanisms controlling nanoparticle nucleation and growth," *ACS nano*, vol. 6, no. 10, pp. 8599–8610, 2012.

[31] J. Hermannsdörfer, V. Tinnemann, D. B. Peckys, and N. de Jonge, "The effect of electron beam irradiation in environmental scanning transmission electron microscopy of whole cells in liquid," *Microscopy and Microanalysis*, vol. 22, no. 3, pp. 656–665, 2016.

[32] A. Radisic, P. Vereecken, P. Searson, and F. Ross, "The morphology and nucleation kinetics of copper islands during electrodeposition," *Surface science*, vol. 600, no. 9, pp. 1817–1826, 2006.

[33] K. Jungjohann, S. Bliznakov, P. Sutter, E. Stach, and E. Sutter, "In situ liquid cell electron microscopy of the solution growth of au–pd core–shell nanostructures," *Nano letters*, vol. 13, no. 6, pp. 2964–2970, 2013.

[34] J. Yang, C. M. Andrei, Y. Chan, B. L. Mehdi, N. D. Browning, G. A. Botton, and L. Soleymani, "Liquid cell transmission electron microscopy sheds light on the mechanism of palladium electrodeposition," *Langmuir*, vol. 35, no. 4, pp. 862–869, 2019.

[35] C. Zhu, S. Liang, E. Song, Y. Zhou, W. Wang, F. Shan, Y. Shi, C. Hao, K. Yin, T. Zhang, *et al.*, "In-situ liquid cell transmission electron microscopy investigation on oriented attachment of gold nanoparticles," *Nature communications*, vol. 9, no. 1, pp. 1–7, 2018.

[36] K. Gnanasekaran, H. Chang, P. J. Smeets, J. Korpanty, F. M. Geiger, and N. C. Gianneschi, "In situ ni2+ stain for liposome imaging by liquid-cell transmission electron microscopy," *Nano letters*, vol. 20, no. 6, pp. 4292–4297, 2020.

[37] L. R. Parent, E. Bakalis, A. Ramírez-Hernández, J. K. Kammeyer, C. Park, J. De Pablo, F. Zerbetto, J. P. Patterson, and N. C. Gianneschi, "Directly observing

micelle fusion and growth in solution by liquid-cell transmission electron microscopy," *Journal of the American Chemical Society*, vol. 139, no. 47, pp. 17140–17151, 2017.

[38] J. P. Patterson, P. Abellan, M. S. Denny Jr, C. Park, N. D. Browning, S. M. Cohen, J. E. Evans, and N. C. Gianneschi, "Observing the growth of metal–organic frameworks by in situ liquid cell transmission electron microscopy," *Journal of the American Chemical Society*, vol. 137, no. 23, pp. 7322–7328, 2015.

[39] M. T. Proetto, A. M. Rush, M.-P. Chien, P. Abellan Baeza, J. P. Patterson, M. P. Thompson, N. H. Olson, C. E. Moore, A. L. Rheingold, C. Andolina, *et al.*, "Dynamics of soft nanomaterials captured by transmission electron microscopy in liquid water," *Journal of the American Chemical Society*, vol. 136, no. 4, pp. 1162–1165, 2014.

[40] K. M. Vailonis, K. Gnanasekaran, X. B. Powers, N. C. Gianneschi, and D. M. Jenkins, "Elucidating the growth of metal–organic nanotubes combining isoreticular synthesis with liquid-cell transmission electron microscopy," *Journal of the American Chemical Society*, vol. 141, no. 26, pp. 10177–10182, 2019.

[41] A. Ianiro, H. Wu, M. M. van Rijt, M. P. Vena, A. D. Keizer, A. Esteves, R. Tuinier, H. Friedrich, N. A. Sommerdijk, and J. P. Patterson, "Liquid–liquid phase separation during amphiphilic self-assembly," *Nature chemistry*, vol. 11, no. 4, pp. 320–328, 2019.

[42] N. De Jonge, D. B. Peckys, G. Kremers, and D. Piston, "Electron microscopy of whole cells in liquid with nanometer resolution," *Proceedings of the National Academy of Sciences*, vol. 106, no. 7, pp. 2159–2164, 2009.

[43] A. C. Varano, A. Rahimi, M. J. Dukes, S. Poelzing, S. M. McDonald, and D. F. Kelly, "Visualizing virus particle mobility in liquid at the nanoscale," *Chemical Communications*, vol. 51, no. 90, pp. 16176–16179, 2015.

[44] S. Keskin, S. Besztejan, G. Kassier, S. Manz, R. Bücker, S. Riekeberg, H. K. Trieu, A. Rentmeister, and R. J. D. Miller, "Visualization of multimerization and self-assembly of dna-functionalized gold nanoparticles using in-liquid transmission electron microscopy," *The Journal of Physical Chemistry Letters*, vol. 6, no. 22,

pp. 4487–4492, 2015. PMID: 26509279.

[45] I. N. Dahmke, A. Verch, J. Hermannsdorfer, D. B. Peckys, R. S. Weatherup, S. Hofmann, and N. de Jonge, "Graphene liquid enclosure for single-molecule analysis of membrane proteins in whole cells using electron microscopy," *ACS nano*, vol. 11, no. 11, pp. 11108–11117, 2017.

[46] Z. Zeng, W.-I. Liang, H.-G. Liao, H. L. Xin, Y.-H. Chu, and H. Zheng, "Visualization of electrode–electrolyte interfaces in lipf6/ec/dec electrolyte for lithium ion batteries via in situ tem," *Nano letters*, vol. 14, no. 4, pp. 1745–1750, 2014.

[47] B. L. Mehdi, J. Qian, E. Nasybulin, C. Park, D. A. Welch, R. Faller, H. Mehta, W. A. Henderson, W. Xu, C. M. Wang, *et al.*, "Observation and quantification of nanoscale processes in lithium batteries by operando electrochemical (s) tem," *Nano letters*, vol. 15, no. 3, pp. 2168–2173, 2015.

[48] R. L. Sacci, N. J. Dudney, K. L. More, L. R. Parent, I. Arslan, N. D. Browning, and R. R. Unocic, "Direct visualization of initial sei morphology and growth kinetics during lithium deposition by in situ electrochemical transmission electron microscopy," *Chemical Communications*, vol. 50, no. 17, pp. 2104–2107, 2014.

[49] J. Qian, W. Xu, P. Bhattacharya, M. Engelhard, W. A. Henderson, Y. Zhang, and J.-G. Zhang, "Dendrite-free li deposition using trace-amounts of water as an electrolyte additive," *Nano Energy*, vol. 15, pp. 135–144, 2015.

[50] J. H. Park, N. M. Schneider, D. A. Steingart, H. Deligianni, S. Kodambaka, and F. M. Ross, "Control of growth front evolution by bi additives during znau electrodeposition," *Nano letters*, vol. 18, no. 2, pp. 1093–1098, 2018.

[51] B. Mehdi, A. Stevens, J. Qian, C. Park, W. Xu, W. Henderson, J. Zhang, K. Mueller, and N. Browning, "The impact of li grain size on coulombic efficiency in li batteries, sci," 2016.

[52] M. Gu, L. R. Parent, B. L. Mehdi, R. R. Unocic, M. T. McDowell, R. L. Sacci, W. Xu, J. G. Connell, P. Xu, P. Abellan, *et al.*, "Demonstration of an electrochemical liquid cell for operando transmission electron microscopy observation of the

lithiation/delithiation behavior of si nanowire battery anodes," *Nano Letters*, vol. 13, no. 12, pp. 6106–6112, 2013.

[53] J. Xie, J. Li, W. Mai, and G. Hong, "A decade of advanced rechargeable batteries development guided by in situ transmission electron microscopy," *Nano Energy*, vol. 83, p. 105780, 2021.

[54] N. de Jonge, "Theory of the spatial resolution of (scanning) transmission electron microscopy in liquid water or ice layers," *Ultramicroscopy*, vol. 187, pp. 113–125, 2018.

[55] A. Hutzler, *Development of advanced liquid cell architectures for high performance in situ transmission electron microscopy in materials sciences*. PhD thesis, Friedrich-Alexander-Universität Erlangen-Nürnberg (FAU), 2018.

[56] B. Ambrožič, A. Prašnikar, N. Hodnik, N. Kostevšek, B. Likozar, K. Ž. Rožman, and S. Šturm, "Controlling the radical-induced redox chemistry inside a liquid-cell tem," *Chemical science*, vol. 10, no. 38, pp. 8735–8743, 2019.

[57] S. Keskin, *In-liquid Electron Microscopy and Diffraction for real-time observation and structural analysis*. PhD thesis, Staats-und Universitätsbibliothek Hamburg Carl von Ossietzky, 2016.

[58] N. De Jonge and F. M. Ross, "Electron microscopy of specimens in liquid," *Nature nanotechnology*, vol. 6, no. 11, pp. 695–704, 2011.

[59] J. Rodenburg and E. Macak, "Optimising the resolution of tem/stem with the electron ronchigram," *Microscopy*, 2013.

[60] N. de Jonge, N. Poirier-Demers, H. Demers, D. B. Peckys, and D. Drouin, "Nanometer-resolution electron microscopy through micrometers-thick water layers," *Ultramicroscopy*, vol. 110, no. 9, pp. 1114–1119, 2010.

[61] D. Parsons, V. Matricardi, R. Moretz, and J. Turner, "Electron microscopy and diffraction of wet unstained and unfixed biological objects," *Advances in biological and medical physics*, vol. 15, pp. 161–270, 1974.

[62] K. L. Jungjohann, J. E. Evans, J. A. Aguiar, I. Arslan, and N. D. Browning, "Atomic-

scale imaging and spectroscopy for in situ liquid scanning transmission electron microscopy," *Microscopy and Microanalysis*, vol. 18, no. 3, pp. 621–627, 2012.

[63] M. E. Holtz, Y. Yu, D. Gunceler, J. Gao, R. Sundararaman, K. A. Schwarz, T. A. Arias, H. D. Abruña, and D. A. Muller, "Nanoscale imaging of lithium ion distribution during in situ operation of battery electrode and electrolyte," *Nano letters*, vol. 14, no. 3, pp. 1453–1459, 2014.

[64] J. Thomas, M. GraceáBurke, *et al.*, "Real-time imaging and local elemental analysis of nanostructures in liquids," *Chemical Communications*, vol. 50, no. 70, pp. 10019–10022, 2014.

[65] S. Keskin, P. Kunnas, and N. de Jonge, "Liquid-phase electron microscopy with controllable liquid thickness," *Nano letters*, vol. 19, no. 7, pp. 4608–4613, 2019.

[66] P. Kunnas, "Liquid-phase electron microscopy: toward direct imaging of self-assembly processes in low-atomic number colloidal suspensions," 2021.

[67] S. Helveg, C. Lopez-Cartes, J. Sehested, P. L. Hansen, B. S. Clausen, J. R. Rostrup-Nielsen, F. Abild-Pedersen, and J. K. Nørskov, "Atomic-scale imaging of carbon nanofibre growth," *Nature*, vol. 427, no. 6973, pp. 426–429, 2004.

[68] S. Sze, *VLSI Technology*. Electronics and electronic circuits, McGraw-Hill, 1988.

[69] D. Widmann, H. Mader, and H. Friedrich, *Technologie hochintegrierter Schaltungen*, vol. 19. Springer-Verlag, 2013.

[70] W. Runyan and K. Bean, *Semiconductor Integrated Circuit Processing Technology*. Addison-Wesley series in electrical and computer engineering, Addison-Wesley, 1990.

[71] A. J. Leenheer, J. P. Sullivan, M. J. Shaw, and C. T. Harris, "A sealed liquid cell for in situ transmission electron microscopy of controlled electrochemical processes," *Journal of Microelectromechanical Systems*, vol. 24, no. 4, pp. 1061–1068, 2015.

[72] E. R. White, M. Mecklenburg, S. B. Singer, S. Aloni, and B. C. Regan, "Imaging nanobubbles in water with scanning transmission electron microscopy," *Applied physics express*, vol. 4, no. 5, p. 055201, 2011.

[73] M. J. Dukes, R. Thomas, J. Damiano, K. L. Klein, S. Balasubramaniam, S. Kayandan,

J. S. Riffle, R. M. Davis, S. M. McDonald, and D. F. Kelly, "Improved microchip design and application for in situ transmission electron microscopy of macromolecules," *Microscopy and Microanalysis*, vol. 20, no. 2, pp. 338–345, 2014.

[74] J. M. Yuk, J. Park, P. Ercius, K. Kim, D. J. Hellebusch, M. F. Crommie, J. Y. Lee, A. Zettl, and A. P. Alivisatos, "High-resolution em of colloidal nanocrystal growth using graphene liquid cells," *Science*, vol. 336, no. 6077, pp. 61–64, 2012.

[75] N. Mohanty, M. Fahrenholtz, A. Nagaraja, D. Boyle, and V. Berry, "Impermeable graphenic encasement of bacteria," *Nano letters*, vol. 11, no. 3, pp. 1270–1275, 2011.

[76] C. Wang, Q. Qiao, T. Shokuhfar, and R. F. Klie, "High-resolution electron microscopy and spectroscopy of ferritin in biocompatible graphene liquid cells and graphene sandwiches," *Advanced Materials*, vol. 26, no. 21, pp. 3410–3414, 2014.

[77] C. Colliex, "Watching solution growth of nanoparticles in graphene cells," *Science*, vol. 336, no. 6077, pp. 44–45, 2012.

[78] Q. Chen, J. M. Smith, J. Park, K. Kim, D. Ho, H. I. Rasool, A. Zettl, and A. P. Alivisatos, "3d motion of dna-au nanoconjugates in graphene liquid cell electron microscopy," *Nano letters*, vol. 13, no. 9, pp. 4556–4561, 2013.

[79] J. M. Yuk, H. K. Seo, J. W. Choi, and J. Y. Lee, "Anisotropic lithiation onset in silicon nanoparticle anode revealed by in situ graphene liquid cell electron microscopy," *ACS nano*, vol. 8, no. 7, pp. 7478–7485, 2014.

[80] M. Jeong, J. M. Yuk, and J. Y. Lee, "Observation of surface atoms during platinum nanocrystal growth by monomer attachment," *Chemistry of Materials*, vol. 27, no. 9, pp. 3200–3202, 2015.

[81] D. Shin, J. B. Park, Y.-J. Kim, S. J. Kim, J. H. Kang, B. Lee, S.-P. Cho, B. H. Hong, and K. S. Novoselov, "Growth dynamics and gas transport mechanism of nanobubbles in graphene liquid cells," *Nature communications*, vol. 6, no. 1, pp. 1–6, 2015.

[82] C. Wang, T. Shokuhfar, and R. F. Klie, "Precise in situ modulation of local liquid

chemistry via electron irradiation in nanoreactors based on graphene liquid cells," *Advanced Materials*, vol. 28, no. 35, pp. 7716–7722, 2016.

[83] J. M. Yuk, Q. Zhou, J. Chang, P. Ercius, A. P. Alivisatos, and A. Zettl, "Real-time observation of water-soluble mineral precipitation in aqueous solution by in situ high-resolution electron microscopy," *ACS nano*, vol. 10, no. 1, pp. 88–92, 2016.

[84] Y. Huang, J. Wu, and K.-C. Hwang, "Thickness of graphene and single-wall carbon nanotubes," *Physical review B*, vol. 74, no. 24, p. 245413, 2006.

[85] P. Nemes-Incze, Z. Osváth, K. Kamarás, and L. Biró, "Anomalies in thickness measurements of graphene and few layer graphite crystals by tapping mode atomic force microscopy," *Carbon*, vol. 46, no. 11, pp. 1435–1442, 2008.

[86] K. S. Kim, Y. Zhao, H. Jang, S. Y. Lee, J. M. Kim, K. S. Kim, J.-H. Ahn, P. Kim, J.-Y. Choi, and B. H. Hong, "Large-scale pattern growth of graphene films for stretchable transparent electrodes," *nature*, vol. 457, no. 7230, pp. 706–710, 2009.

[87] I. Frank, D. M. Tanenbaum, A. M. van der Zande, and P. L. McEuen, "Mechanical properties of suspended graphene sheets," *Journal of Vacuum Science & Technology B: Microelectronics and Nanometer Structures Processing, Measurement, and Phenomena*, vol. 25, no. 6, pp. 2558–2561, 2007.

[88] X. Wang, L. Zhi, and K. Müllen, "Transparent, conductive graphene electrodes for dye-sensitized solar cells," *Nano letters*, vol. 8, no. 1, pp. 323–327, 2008.

[89] R. S. Pantelic, J. C. Meyer, U. Kaiser, and H. Stahlberg, "The application of graphene as a sample support in transmission electron microscopy," *Solid State Communications*, vol. 152, no. 15, pp. 1375–1382, 2012.

[90] M. Krueger, S. Berg, D. Stone, E. Strelcov, D. A. Dikin, J. Kim, L. J. Cote, J. Huang, and A. Kolmakov, "Drop-casted self-assembling graphene oxide membranes for scanning electron microscopy on wet and dense gaseous samples," *ACS nano*, vol. 5, no. 12, pp. 10047–10054, 2011.

[91] A. De Clercq, W. Dachraoui, O. Margeat, K. Pelzer, C. R. Henry, and S. Giorgio, "Growth of pt–pd nanoparticles studied in situ by hrtem in a liquid cell," *The Journal*

of *Physical Chemistry Letters*, vol. 5, no. 12, pp. 2126–2130, 2014.

[92] K. Nishijima, J. Yamasaki, H. Orihara, and N. Tanaka, "Development of microcapsules for electron microscopy and their application to dynamical observation of liquid crystals in transmission electron microscopy," *Nanotechnology*, vol. 15, no. 6, p. S329, 2004.

[93] W. Wei, H. Zhang, W. Wang, M. Dong, M. Nie, L. Sun, and F. Xu, "Observing the growth of pb3o4 nanocrystals by in situ liquid cell transmission electron microscopy," *ACS applied materials & interfaces*, vol. 11, no. 27, pp. 24478–24484, 2019.

[94] K. He, T. Shokuhfar, and R. Shahbazian-Yassar, "Imaging of soft materials using in situ liquid-cell transmission electron microscopy," *Journal of Physics: Condensed Matter*, vol. 31, no. 10, p. 103001, 2019.

[95] A. Hutzler, B. Fritsch, M. P. Jank, R. Branscheid, R. C. Martens, E. Spiecker, and M. März, "In situ liquid cell tem studies on etching and growth mechanisms of gold nanoparticles at a solid–liquid–gas interface," *Advanced Materials Interfaces*, vol. 6, no. 20, p. 1901027, 2019.

[96] E. S. Pohlmann, K. Patel, S. Guo, M. J. Dukes, Z. Sheng, and D. F. Kelly, "Real-time visualization of nanoparticles interacting with glioblastoma stem cells," *Nano letters*, vol. 15, no. 4, pp. 2329–2335, 2015.

[97] S. R. Cherry, J. Sorenson, M. E. Phelps, and B. M. Methé, "Physics in nuclear medicine," *Medical Physics*, vol. 31, no. 8, pp. 2370–2371, 2004.

[98] B. A. CARTER, D. B. Williams, C. B. Carter, and D. B. Williams, *Transmission electron microscopy: a textbook for materials science. Diffraction. II*, vol. 2. Springer Science & Business Media, 1996.

[99] S. T. Manson, "Dependence of the phase shift on energy and atomic number for electron scattering by atomic fields," *Physical Review*, vol. 182, no. 1, p. 97, 1969.

[100] R. Danev and K. Nagayama, "Transmission electron microscopy with zernike phase plate," *Ultramicroscopy*, vol. 88, no. 4, pp. 243–252, 2001.

[101] R. Danev, B. Buijsse, M. Khoshouei, J. M. Plitzko, and W. Baumeister, "Volta

potential phase plate for in-focus phase contrast transmission electron microscopy," *Proceedings of the National Academy of Sciences*, vol. 111, no. 44, pp. 15635–15640, 2014.

[102] K. Nagayama and R. Danev, "Phase-plate electron microscopy: a novel imaging tool to reveal close-to-life nano-structures," *Biophysical reviews*, vol. 1, no. 1, pp. 37–42, 2009.

[103] L. Rayleigh, "Xii. on the manufacture and theory of diffraction-gratings," *The London, Edinburgh, and Dublin Philosophical Magazine and Journal of Science*, vol. 47, no. 310, pp. 81–93, 1874.

[104] R. F. Egerton *et al.*, *Physical principles of electron microscopy*, vol. 56. Springer, 2005.

[105] K. L. Klein, I. M. Anderson, and N. De Jonge, "Transmission electron microscopy with a liquid flow cell," *Journal of microscopy*, vol. 242, no. 2, pp. 117–123, 2011.

[106] M. Haider, S. Uhlemann, E. Schwan, H. Rose, B. Kabius, and K. Urban, "Electron microscopy image enhanced," *Nature*, vol. 392, no. 6678, pp. 768–769, 1998.

[107] M. Haider, P. Hartel, H. Müller, S. Uhlemann, and J. Zach, "Current and future aberration correctors for the improvement of resolution in electron microscopy," *Philosophical Transactions of the Royal Society A: Mathematical, Physical and Engineering Sciences*, vol. 367, no. 1903, pp. 3665–3682, 2009.

[108] N. de Jonge, L. Houben, R. E. Dunin-Borkowski, and F. M. Ross, "Resolution and aberration correction in liquid cell transmission electron microscopy," *Nature Reviews Materials*, vol. 4, no. 1, pp. 61–78, 2019.

[109] J. M. Grogan and H. H. Bau, "The nanoaquarium: a platform for in situ transmission electron microscopy in liquid media," *Journal of Microelectromechanical Systems*, vol. 19, no. 4, pp. 885–894, 2010.

[110] S. Lagana, E. Mikkelsen, H. Sun, R. Marie, and K. Mølhave, *Quasi-nanofluidic liquid cell for in situ liquid transmission electron microscopy*. Germany: Wiley-VCH, 2016. The 16th European Microscopy Congress, EMC2016 ; Conference date: 28-08-2016

Through 02-09-2016.

[111] J. M. Grogan, N. M. Schneider, F. M. Ross, and H. H. Bau, "Bubble and pattern formation in liquid induced by an electron beam," *Nano letters*, vol. 14, no. 1, pp. 359–364, 2014.

[112] S. B. Alam, J. Yang, K. C. Bustillo, C. Ophus, P. Ercius, H. Zheng, and E. M. Chan, "Hybrid nanocapsules for in situ tem imaging of gas evolution reactions in confined liquids," *Nanoscale*, vol. 12, no. 36, pp. 18606–18615, 2020.

[113] E. A. Ring and N. De Jonge, "Microfluidic system for transmission electron microscopy," *Microscopy and Microanalysis*, vol. 16, no. 5, pp. 622–629, 2010.

[114] Y. Nishizawa, S. Matsui, K. Urayama, T. Kureha, M. Shibayama, T. Uchihashi, and D. Suzuki, "Non-thermoresponsive decanano-sized domains in thermoresponsive hydrogel microspheres revealed by temperature-controlled high-speed atomic force microscopy," *Angewandte Chemie International Edition*, vol. 58, no. 26, pp. 8809–8813, 2019.

[115] E. R. Osorio-Blanco, J. Bergueiro, B. E. Abali, S. Ehrmann, C. Böttcher, A. J. Müller, J. L. Cuellar-Camacho, and M. Calderón, "Effect of core nanostructure on the thermomechanical properties of soft nanoparticles," *Chemistry of Materials*, vol. 32, no. 1, pp. 518–528, 2019.

[116] W. H. Press, S. A. Teukolsky, B. P. Flannery, and W. T. Vetterling, *Numerical recipes in Fortran 77: volume 1, volume 1 of Fortran numerical recipes: the art of scientific computing*. Cambridge university press, 1992.

[117] A. Maigne and Gatan, "How to optimize your eels experiments by adjusting the collection angle of your spectrometer." https://analyticalscience.wiley.com/do/10.1002/micro.140/full/. (accessed: 01.09.2020).

[118] J. Vlassak and W. Nix, "A new bulge test technique for the determination of young's modulus and poisson's ratio of thin films," *Journal of materials research*, vol. 7, no. 12, pp. 3242–3249, 1992.

[119] R. Ghosh Chaudhuri and S. Paria, "Core/shell nanoparticles: classes, properties, synthesis mechanisms, characterization, and applications," *Chemical reviews*, vol. 112, no. 4, pp. 2373–2433, 2012.

[120] Y. Han, Z. Lu, Z. Teng, J. Liang, Z. Guo, D. Wang, M.-Y. Han, and W. Yang, "Unraveling the growth mechanism of silica particles in the stober method: in situ seeded growth model," *Langmuir*, vol. 33, no. 23, pp. 5879–5890, 2017.

[121] N. Razza, G. Rizza, P.-E. Coulon, L. Didier, G. C. Fadda, B. Voit, A. Synytska, H. Grützmacher, and M. Sangermano, "Enabling the synthesis of homogeneous or janus hairy nanoparticles through surface photoactivation," *Nanoscale*, vol. 10, no. 30, pp. 14492–14498, 2018.

[122] M. Molina, M. Asadian-Birjand, J. Balach, J. Bergueiro, E. Miceli, and M. Calderón, "Stimuli-responsive nanogel composites and their application in nanomedicine," *Chemical Society Reviews*, vol. 44, no. 17, pp. 6161–6186, 2015.

[123] J. Bergueiro and M. Calderón, "Thermoresponsive nanodevices in biomedical applications," *Macromolecular bioscience*, vol. 15, no. 2, pp. 183–199, 2015.

[124] M. Stieger, W. Richtering, J. S. Pedersen, and P. Lindner, "Small-angle neutron scattering study of structural changes in temperature sensitive microgel colloids," *The Journal of chemical physics*, vol. 120, no. 13, pp. 6197–6206, 2004.

[125] S. Takata, M. Shibayama, R. Sasabe, and H. Kawaguchi, "Preparation and structure characterization of hairy nanoparticles consisting of hydrophobic core and thermosensitive hairs," *Polymer*, vol. 44, no. 2, pp. 495–501, 2003.

[126] K. Kratz, T. Hellweg, and W. Eimer, "Structural changes in pnipam microgel particles as seen by sans, dls, and em techniques," *Polymer*, vol. 42, no. 15, pp. 6631–6639, 2001.

[127] J. J. Crassous, C. N. Rochette, A. Wittemann, M. Schrinner, M. Ballauff, and M. Drechsler, "Quantitative analysis of polymer colloids by cryo-transmission electron microscopy," *Langmuir*, vol. 25, no. 14, pp. 7862–7871, 2009.

[128] Y. Liao, "Practical electron microscopy and database-an online book," *can be found*

under *http://www. globalsino. com/EM/, nd*, 2018.

[129] A. Verch, M. Pfaff, and N. de Jonge, "Exceptionally slow movement of gold nanoparticles at a solid/liquid interface investigated by scanning transmission electron microscopy," *Langmuir*, vol. 31, no. 25, pp. 6956–6964, 2015.

[130] J. Wang, R. P. Sagar, H. Schmider, and V. Smith, "X-ray elastic and inelastic scattering factors for neutral atoms z= 2-92," *Atomic data and nuclear data tables*, vol. 53, no. 2, pp. 233–269, 1993.

[131] E. J. Kirkland, *Advanced computing in electron microscopy*. Springer Nature, 2020.

[132] T. Kaneko, "Partial and total electronic stopping cross sections of atoms and solids for protons," *Atomic Data and Nuclear Data Tables*, vol. 53, no. 2, pp. 271–340, 1993.

[133] L. Reimer and K. Sommer, "Messungen und berechnungen zum elektronen-mikroskopischen streukontrast für 17 bis 1200 kev-elektronen," *Zeitschrift für Naturforschung A*, vol. 23, no. 10, pp. 1569–1582, 1968.

[134] H. Zhang, R. F. Egerton, and M. Malac, "Local thickness measurement in tem," *Microscopy and Microanalysis*, vol. 16, no. S2, pp. 344–345, 2010.

[135] F. Salvat, A. Jablonski, and C. J. Powell, "Elsepa—dirac partial-wave calculation of elastic scattering of electrons and positrons by atoms, positive ions and molecules," *Computer physics communications*, vol. 165, no. 2, pp. 157–190, 2005.

[136] H. Demers, N. Poirier-Demers, A. R. Couture, D. Joly, M. Guilmain, N. de Jonge, and D. Drouin, "Three-dimensional electron microscopy simulation with the casino monte carlo software," *Scanning*, vol. 33, no. 3, pp. 135–146, 2011.

[137] S. Le Caër, "Water radiolysis: influence of oxide surfaces on h2 production under ionizing radiation," *Water*, vol. 3, no. 1, pp. 235–253, 2011.

[138] H. G. Schild, M. Muthukumar, and D. A. Tirrell, "Cononsolvency in mixed aqueous solutions of poly (n-isopropylacrylamide)," *Macromolecules*, vol. 24, no. 4, pp. 948–952, 1991.

[139] J. C. Cuggino, E. R. O. Blanco, L. M. Gugliotta, C. I. A. Igarzabal, and M. Calderón,

"Crossing biological barriers with nanogels to improve drug delivery performance," *Journal of Controlled Release*, vol. 307, pp. 221–246, 2019.

[140] M. R. Hauwiller, J. C. Ondry, C. M. Chan, P. Khandekar, J. Yu, and A. P. Alivisatos, "Gold nanocrystal etching as a means of probing the dynamic chemical environment in graphene liquid cell electron microscopy," *Journal of the American Chemical Society*, vol. 141, no. 10, pp. 4428–4437, 2019.

[141] R. Egerton, "Control of radiation damage in the tem," *Ultramicroscopy*, vol. 127, pp. 100–108, 2013.

[142] J. Yang, S. B. Alam, L. Yu, E. Chan, and H. Zheng, "Dynamic behavior of nanoscale liquids in graphene liquid cells revealed by in situ transmission electron microscopy," *Micron*, vol. 116, pp. 22–29, 2019.

[143] V. Brunella, S. A. Jadhav, I. Miletto, G. Berlier, E. Ugazio, S. Sapino, and D. Scalarone, "Hybrid drug carriers with temperature-controlled on–off release: A simple and reliable synthesis of pnipam-functionalized mesoporous silica nanoparticles," *Reactive and Functional Polymers*, vol. 98, pp. 31–37, 2016.

[144] E. Auchter, J. Marquez, G. Stevens, R. Silva, Q. Mcculloch, Q. Guengerich, A. Blair, S. Litchfield, N. Li, C. Sheehan, *et al.*, "Ultra-thin and strong formvar-based membranes with controlled porosity for micro-and nano-scale systems," *Nanotechnology*, vol. 29, no. 21, p. 215712, 2018.

[145] E. Davison and W. Colquhoun, "Ultrathin formvar support films for transmission electron microscopy," *Journal of electron microscopy technique*, vol. 2, no. 1, pp. 35–43, 1985.

[146] A. Ren, D. Lu, E. Wong, M. R. Hauwiller, A. P. Alivisatos, and G. Ren, "Real-time observation of dynamic structure of liquid-vapor interface at nanometer resolution in electron irradiated sodium chloride crystals," *Scientific reports*, vol. 10, no. 1, pp. 1–13, 2020.

[147] G. Both, E. Kanter, Z. Vager, B. Zabransky, and D. Zajfman, "Ultrathin foils for coulomb-explosion experiments," *Review of scientific instruments*, vol. 58, no. 3,

pp. 424–427, 1987.

[148] N. D. Loh, S. Sen, M. Bosman, S. F. Tan, J. Zhong, C. A. Nijhuis, P. Král, P. Matsudaira, and U. Mirsaidov, "Multistep nucleation of nanocrystals in aqueous solution," *Nature chemistry*, vol. 9, no. 1, pp. 77–82, 2017.

[149] E. Gachard, H. Remita, J. Khatouri, B. Keita, L. Nadjo, and J. Belloni, "Radiation-induced and chemical formation of gold clusters," *New Journal of Chemistry*, vol. 22, no. 11, pp. 1257–1265, 1998.

[150] M. Wang, C. Park, and T. J. Woehl, "Quantifying the nucleation and growth kinetics of electron beam nanochemistry with liquid cell scanning transmission electron microscopy," *Chemistry of Materials*, vol. 30, no. 21, pp. 7727–7736, 2018.

[151] Q. Zhang, X. Yang, P. Li, G. Huang, S. Feng, C. Shen, B. Han, X. Zhang, F. Jin, F. Xu, *et al.*, "Bioinspired engineering of honeycomb structure–using nature to inspire human innovation," *Progress in Materials Science*, vol. 74, pp. 332–400, 2015.

[152] K. Lim, Y. Bae, S. Jeon, K. Kim, B. H. Kim, J. Kim, S. Kang, T. Heo, J. Park, and W. C. Lee, "A large-scale array of ordered graphene-sandwiched chambers for quantitative liquid-phase transmission electron microscopy," *Advanced Materials*, vol. 32, no. 39, p. 2002889, 2020.

[153] R. Egerton, P. Li, and M. Malac, "Radiation damage in the tem and sem," *Micron*, vol. 35, no. 6, pp. 399–409, 2004.

[154] R. Egerton, "Radiation damage to organic and inorganic specimens in the tem," *Micron*, vol. 119, pp. 72–87, 2019.

[155] T. Woehl and P. Abellan, "Defining the radiation chemistry during liquid cell electron microscopy to enable visualization of nanomaterial growth and degradation dynamics," *Journal of microscopy*, vol. 265, no. 2, pp. 135–147, 2017.

[156] J. Korpanty, L. R. Parent, and N. C. Gianneschi, "Enhancing and mitigating radiolytic damage to soft matter in aqueous phase liquid-cell transmission electron microscopy in the presence of gold nanoparticle sensitizers or isopropanol scavengers," *Nano letters*, vol. 21, no. 2, pp. 1141–1149, 2021.

[157] B. H. Kim, J. Yang, D. Lee, B. K. Choi, T. Hyeon, and J. Park, "Liquid-phase transmission electron microscopy for studying colloidal inorganic nanoparticles," *Advanced Materials*, vol. 30, no. 4, p. 1703316, 2018.

[158] B. Pastina and J. A. LaVerne, "Effect of molecular hydrogen on hydrogen peroxide in water radiolysis," *The Journal of Physical Chemistry A*, vol. 105, no. 40, pp. 9316–9322, 2001.

[159] A. J. Elliot and D. R. McCracken, "Computer modelling of the radiolysis in an aqueous lithium salt blanket: Suppression of radiolysis by addition of hydrogen," *Fusion engineering and design*, vol. 13, no. 1, pp. 21–27, 1990.

[160] P. Abellan, T. Woehl, L. Parent, N. Browning, J. Evans, and I. Arslan, "Factors influencing quantitative liquid (scanning) transmission electron microscopy," *Chemical Communications*, vol. 50, no. 38, pp. 4873–4880, 2014.

[161] Y.-C. Chen, J.-Y. Chen, and W.-W. Wu, "In situ observation of au nanostructure evolution in liquid cell tem," *The Journal of Physical Chemistry C*, vol. 121, no. 46, pp. 26069–26075, 2017.

[162] W. Kleber, H.-J. Bautsch, J. Bohm, and D. Klimm, *Einführung in die Kristallographie*. Oldenbourg Wissenschaftsverlag, 2010.

[163] H.-G. Liao, D. Zherebetskyy, H. Xin, C. Czarnik, P. Ercius, H. Elmlund, M. Pan, L.-W. Wang, and H. Zheng, "Facet development during platinum nanocube growth," *science*, vol. 345, no. 6199, pp. 916–919, 2014.

[164] P. Abellan, L. R. Parent, N. Al Hasan, C. Park, I. Arslan, A. M. Karim, J. E. Evans, and N. D. Browning, "Gaining control over radiolytic synthesis of uniform sub-3-nanometer palladium nanoparticles: Use of aromatic liquids in the electron microscope," *Langmuir*, vol. 32, no. 6, pp. 1468–1477, 2016.

[165] D. Alloyeau, W. Dachraoui, Y. Javed, H. Belkahla, G. Wang, H. Lecoq, S. Ammar, O. Ersen, A. Wisnet, F. Gazeau, *et al.*, "Unravelling kinetic and thermodynamic effects on the growth of gold nanoplates by liquid transmission electron microscopy," *Nano letters*, vol. 15, no. 4, pp. 2574–2581, 2015.

[166] Y. Jiang, G. Zhu, F. Lin, H. Zhang, C. Jin, J. Yuan, D. Yang, and Z. Zhang, "In situ study of oxidative etching of palladium nanocrystals by liquid cell electron microscopy," *Nano letters*, vol. 14, no. 7, pp. 3761–3765, 2014.

[167] T. Ngo and H. Yang, "Toward ending the guessing game: study of the formation of nanostructures using in situ liquid transmission electron microscopy," *The journal of physical chemistry letters*, vol. 6, no. 24, pp. 5051–5061, 2015.

[168] C. Wagner, "Theorie der alterung von niederschlägen durch umlösen (ostwald-reifung)," *Zeitschrift für Elektrochemie, Berichte der Bunsengesellschaft für physikalische Chemie*, vol. 65, no. 7-8, pp. 581–591, 1961.

[169] C. N. R. Rao, A. Müller, and A. K. Cheetham, "Nanomaterials chemistry: recent developments and new directions," 2007.

[170] "User instructions graphena monolayer graphene film "easy transfer"." `https://cdn.shopify.com/s/files/1/0191/2296/files/Graphenea_Easy_Transfer_Instructions_20210126.pdf?v=1611681633`. Accessed: 2022-02-14.

[171] "Custom Feature Detection: Bubble tracking in 2D foams, howpublished = `http://soft-matter.github.io/trackpy/v0.3.0/tutorial/custom-feature-detection.html`, note = Accessed: 2010-09-30."

[172] S. A. Canepa, B. T. Sneed, H. Sun, R. R. Unocic, and K. Mølhave, "Influence of cetyltrimethylammonium bromide on gold nanocrystal formation studied by in situ liquid cell scanning transmission electron microscopy," *The Journal of Physical Chemistry C*, vol. 122, no. 4, pp. 2350–2357, 2018.

[173] M. J. Meijerink, K. P. De Jong, and J. Zečević, "Growth of supported gold nanoparticles in aqueous phase studied by in situ transmission electron microscopy," *The Journal of Physical Chemistry C*, vol. 124, no. 3, pp. 2202–2212, 2019.

[174] D. Keller, T. R. Henninen, and R. Erni, "Formation of gold nanoparticles in a free-standing ionic liquid triggered by heat and electron irradiation," *Micron*, vol. 117, pp. 16–21, 2019.

[175] H. Cho, M. R. Jones, S. C. Nguyen, M. R. Hauwiller, A. Zettl, and A. P. Alivisatos,

"The use of graphene and its derivatives for liquid-phase transmission electron microscopy of radiation-sensitive specimens," *Nano Letters*, vol. 17, no. 1, pp. 414–420, 2017. PMID: 28026186.

[176] Y. Qiu, Z. Wang, A. C. Owens, I. Kulaots, Y. Chen, A. B. Kane, and R. H. Hurt, "Antioxidant chemistry of graphene-based materials and its role in oxidation protection technology," *Nanoscale*, vol. 6, no. 20, pp. 11744–11755, 2014.

[177] E. J. Radich and P. V. Kamat, "Making graphene holey. gold-nanoparticle-mediated hydroxyl radical attack on reduced graphene oxide," *ACS nano*, vol. 7, no. 6, pp. 5546–5557, 2013.

[178] C. Yu, B. Zhang, F. Yan, J. Zhao, J. Li, L. Li, and J. Li, "Engineering nano-porous graphene oxide by hydroxyl radicals," *Carbon*, vol. 105, pp. 291–296, 2016.

[179] Y. Chong, C. Ge, G. Fang, X. Tian, X. Ma, T. Wen, W. G. Wamer, C. Chen, Z. Chai, and J.-J. Yin, "Crossover between anti-and pro-oxidant activities of graphene quantum dots in the absence or presence of light," *ACS nano*, vol. 10, no. 9, pp. 8690–8699, 2016.

[180] S. G. Rinaldo, W. Lee, J. Stumper, and M. Eikerling, "Nonmonotonic dynamics in lifshitz-slyozov-wagner theory: Ostwald ripening in nanoparticle catalysts," *Physical Review E*, vol. 86, no. 4, p. 041601, 2012.

[181] R. Viswanatha and D. D. Sarma, *Growth of Nanocrystals in Solution*, ch. 4, pp. 139–170. John Wiley Sons, Ltd, 2007.

[182] T. J. Woehl, T. Moser, J. E. Evans, and F. M. Ross, "Electron-beam-driven chemical processes during liquid phase transmission electron microscopy," *MRS Bulletin*, vol. 45, no. 9, pp. 746–753, 2020.

[183] Y. Liu, K. Tai, and S. J. Dillon, "Growth kinetics and morphological evolution of zno precipitated from solution," *Chemistry of Materials*, vol. 25, no. 15, pp. 2927–2933, 2013.

[184] E. Alizadeh and L. Sanche, "Precursors of solvated electrons in radiobiological physics and chemistry," *Chemical Reviews*, vol. 112, no. 11, pp. 5578–5602, 2012. PMID:

22724633.

[185] L. Reimer, *Scanning Electron Microscopy*. Springer Series in Optical Sciences, Springer, 1998.

[186] D. R. G. Mitchell and G. Casillas, "Secondary electron imaging in an aberration-corrected stem," *Microscopy Today*, vol. 24, no. 5, p. 22–27, 2016.

[187] R. M. Glaeser and K. H. Downing, "Specimen charging on thin films with one conducting layer: discussion of physical principles," *Microscopy and Microanalysis*, vol. 10, no. 6, pp. 790–796, 2004.

[188] S. Hettler, E. Kano, M. Dries, D. Gerthsen, L. Pfaffmann, M. Bruns, M. Beleggia, and M. Malac, "Charging of carbon thin films in scanning and phase-plate transmission electron microscopy," *Ultramicroscopy*, vol. 184, pp. 252–266, 2018.

[189] C. J. Russo and R. Henderson, "Charge accumulation in electron cryomicroscopy," *Ultramicroscopy*, vol. 187, pp. 43–49, 2018.

[190] E. R. B. Adamson, *Secondary electron emission coefficient from Lexan: The low-energy crossover*. Texas Tech University, 1993.

[191] T. Gupta, N. M. Schneider, J. H. Park, D. Steingart, and F. M. Ross, "Spatially dependent dose rate in liquid cell transmission electron microscopy," *Nanoscale*, vol. 10, no. 16, pp. 7702–7710, 2018.

[192] J. Goldstein, D. Newbury, J. Michael, N. Ritchie, J. Scott, and D. Joy, *Scanning Electron Microscopy and X-Ray Microanalysis*. Springer New York, 2017.

[193] J. Fijol, A. Then, G. Tasker, and R. Soave, "Secondary electron yield of sio2 and si3n4 thin films for continuous dynode electron multipliers," *Applied surface science*, vol. 48, pp. 464–471, 1991.

[194] T. J. Woehl, K. L. Jungjohann, J. E. Evans, I. Arslan, W. D. Ristenpart, and N. D. Browning, "Experimental procedures to mitigate electron beam induced artifacts during in situ fluid imaging of nanomaterials," *Ultramicroscopy*, vol. 127, pp. 53–63, 2013.

[195] M. Malac, M. Beleggia, M. Kawasaki, P. Li, and R. F. Egerton, "Convenient contrast

enhancement by a hole-free phase plate," *Ultramicroscopy*, vol. 118, pp. 77–89, 2012.

[196] E. White, M. Mecklenburg, B. Shevitski, S. Singer, and B. Regan, "Charged nanoparticle dynamics in water induced by scanning transmission electron microscopy," *Langmuir*, vol. 28, no. 8, pp. 3695–3698, 2012.

[197] J. Cazaux, "Correlations between ionization radiation damage and charging effects in transmission electron microscopy," *Ultramicroscopy*, vol. 60, no. 3, pp. 411–425, 1995.

[198] K.-L. Liu, C.-C. Wu, Y.-J. Huang, H.-L. Peng, H.-Y. Chang, P. Chang, L. Hsu, and T.-R. Yew, "Novel microchip for in situ tem imaging of living organisms and bio-reactions in aqueous conditions," *Lab on a Chip*, vol. 8, no. 11, pp. 1915–1921, 2008.

[199] J. P. Buban, Q. Ramasse, B. Gipson, N. D. Browning, and H. Stahlberg, "High-resolution low-dose scanning transmission electron microscopy," *Journal of electron microscopy*, vol. 59, no. 2, pp. 103–112, 2010.

[200] S. M. Sze, "Current transport and maximum dielectric strength of silicon nitride films," *Journal of Applied Physics*, vol. 38, no. 7, p. 2951, 1967.

[201] "Download area for poisson superfish." `https://laacg.lanl.gov/laacg/services/download_sf.phtml#ps6`. Accessed: 2022-01-21.

[202] "Astra." `https://www.desy.de/~mpyflo/`. Accessed: 2022-01-21.

[203] H. A. Schwarz, "Applications of the spur diffusion model to the radiation chemistry of aqueous solutions," *The Journal of Physical Chemistry*, vol. 73, no. 6, pp. 1928–1937, 1969.

[204] J. Yang, C. M. Andrei, G. A. Botton, and L. Soleymani, "In liquid observation and quantification of nucleation and growth of gold nanostructures using in situ transmission electron microscopy," *The Journal of Physical Chemistry C*, vol. 121, no. 13, pp. 7435–7441, 2017.

[205] W.-G. Jung, J. H. Park, Y.-R. Jo, and B.-J. Kim, "Growth kinetics of individual au

spiky nanoparticles using liquid-cell transmission electron microscopy," *Journal of the American Chemical Society*, vol. 141, no. 32, pp. 12601–12609, 2019.

[206] Y. Zhang, D. Keller, M. D. Rossell, and R. Erni, "Formation of au nanoparticles in liquid cell transmission electron microscopy: from a systematic study to engineered nanostructures," *Chemistry of Materials*, vol. 29, no. 24, pp. 10518–10525, 2017.

[207] S.-T. Wang, Y. Lin, M. H. Nielsen, C. Y. Song, M. R. Thomas, C. D. Spicer, R. Kröger, P. Ercius, S. Aloni, and M. M. Stevens, "Shape-controlled synthesis and in situ characterisation of anisotropic au nanomaterials using liquid cell transmission electron microscopy," *Nanoscale*, vol. 11, no. 36, pp. 16801–16809, 2019.

[208] J. Scholtz, D. Dijkkamp, and R. Schmitz, "Secondary electron emission properties," *Philips journal of research*, vol. 50, no. 3-4, pp. 375–389, 1996.

[209] N. Jiang, "Beam damage by the induced electric field in transmission electron microscopy," *Micron*, vol. 83, pp. 79–92, 2016.

[210] S. Hettler, J. Onoda, R. Wolkow, J. Pitters, and M. Malac, "Charging of electron beam irradiated amorphous carbon thin films at liquid nitrogen temperature," *Ultramicroscopy*, vol. 196, pp. 161–166, 2019.

[211] K. Danov, R. Danev, and K. Nagayama, "Reconstruction of the electric charge density in thin films from the contrast transfer function measurements," *Ultramicroscopy*, vol. 90, no. 2-3, pp. 85–95, 2002.

[212] K. Danov, R. Danev, and K. Nagayama, "Electric charging of thin films measured using the contrast transfer function," *Ultramicroscopy*, vol. 87, no. 1-2, pp. 45–54, 2001.

[213] G.-B. Feng, M. Cao, L.-P. Yan, and H.-B. Zhang, "Combined effects of sample parameters on polymer charging due to electron irradiation: A contour simulation," *Micron*, vol. 52, pp. 62–66, 2013.

[214] S. F. Tan, S. W. Chee, G. Lin, and U. Mirsaidov, "Direct observation of interactions between nanoparticles and nanoparticle self-assembly in solution," *Accounts of chemical research*, vol. 50, no. 6, pp. 1303–1312, 2017.

[215] B. Mehdi, A. Stevens, L. Kovarik, N. Jiang, H. Mehta, A. Liyu, S. Reehl, B. Stanfill, L. Luzi, W. Hao, *et al.*, "Controlling the spatio-temporal dose distribution during stem imaging by subsampled acquisition: In-situ observations of kinetic processes in liquids," *Applied Physics Letters*, vol. 115, no. 6, p. 063102, 2019.

[216] Z. Wang and A. C. Bovik, "Mean squared error: Love it or leave it? a new look at signal fidelity measures," *IEEE signal processing magazine*, vol. 26, no. 1, pp. 98–117, 2009.

[217] Z. Wang, A. C. Bovik, H. R. Sheikh, and E. P. Simoncelli, "Image quality assessment: from error visibility to structural similarity," *IEEE transactions on image processing*, vol. 13, no. 4, pp. 600–612, 2004.

[218] J. Park, K. Koo, N. Noh, J. H. Chang, J. Y. Cheong, K. S. Dae, J. S. Park, S. Ji, I.-D. Kim, and J. M. Yuk, "Graphene liquid cell electron microscopy: progress, applications, and perspectives," *ACS nano*, vol. 15, no. 1, pp. 288–308, 2021.

[219] M. A. Touve, A. S. Carlini, and N. C. Gianneschi, "Self-assembling peptides imaged by correlated liquid cell transmission electron microscopy and maldi-imaging mass spectrometry," *Nature communications*, vol. 10, no. 1, pp. 1–12, 2019.

[220] L. Yao, Z. Ou, B. Luo, C. Xu, and Q. Chen, "Machine learning to reveal nanoparticle dynamics from liquid-phase tem videos," *ACS central science*, vol. 6, no. 8, pp. 1421–1430, 2020.

[221] H. Zheng, X. Lu, and K. He, "In situ transmission electron microscopy and artificial intelligence enabled data analytics for energy materials," *Journal of Energy Chemistry*, 2021.

APPENDIX A

Appendix 1

A.1 List of Hazardous Substances

Chemicals (CAS number)	Hazard Class	H-Phrases	P-Phrases
1,2-dichloroethane (DCE) (107-06-2)		H225, H302, H304, H315, H319, H331, H335, H350	P210, P301+P310 P303+P361+P353 P304+P340+P311 P305+P351+P338
3-(trimethoxysilyl) propyl methacrylate (2530-85-0)	---	---	---
Acetone (67-64-1)		H225-H319-H336	P210-P305 + P351 + P338-P370 + P378-P403 + P235
Ethanol		H225-H319	P210, P233, P240, P241, P242, P305+P351+P338
Polyvinylformal (9003-33-2)	---	---	---
Gold chloride (16903-35-8)		H290, H302, H314, H373, H411	P273, P280, P301+P312, P303+P361+P353, P305+P351+P338
Isopropyl alcohol (67-63-0)		H225, H319, H336	P210, P233, P240, P242, P242, P305+P351+P338
N,N'-methylenebisacrylamide (110-26-9)		H301, H340	P202, P264, P270, P280, P301+P310, P405
N-isopropyl-acrylamide (2210-25-5)		H302, H318	P264,P270,P280, P301+P312, P305+P351+P338, P501
Potassium persulfate (7727-21-1)		H272, H302, H315, H317, H319, H334	P210, P220, P280, P301+P312, P302+P352, P305+P351+P338
Silica nanoparticles (7631-86-9)		H225, H319	P210, P233, P240, P241, P242, P305+P351+P338
Sodium dodecyl sulfate (151-21-3)		H228, H302+H332, H315, H318, H335, H412	P210, P273, P280, P301+P312, P304+P340+P312, P305+P351+P338

Figure A.1: Information extracted from: http://www.sigmaaldrich.com

ACKNOWLEDGMENTS

Esther Earbin, and Sarah Young, thank you for "filling my cup." I could not have managed this work if not for my friendships and connections outside of the laboratory. Thank you Lydia Smith, Johannes Reppin, Eglė Cebrian and Arthur Cebrian. I must recognize Alberto de la Fuente Ceballos, who will be my husband when this thesis is published. Throughout my dissertation, he has been my: travel companion, calming support, python helper, confidant, roommate, kayaking partner, cheerleader, and much more.

Although I've been grateful to have found myself amongst excellent supervisors, colleagues, and friends, my family is a significant reason I've made it this far. My many aunts and uncles, with whom I've enjoyed many memories. My aunts Karen Krause and Nancy Bernhagen who made their first trip to Europe to attend my defense. My aunt, Dr. Darci Bultema, showed me to dream big, live boldly, and go get the "Dr." title. My brothers, Hunter and Carson, plus my sister-in-law, Emily, not only do I admire them dearly, they have always been there for me and are up to my outlandish ideas. But finally I must recognize, my parents, Scott and Nancy Bultema, who nurtured and supported me into the tenacious, outgoing, compassionate, curious, and confident individual I am today.

Overall, I am genuinely overwhelmed when thinking of all of those who have supported me up to this point. Thank you.

CONTRIBUTORS AND FUNDING SOURCES

Declaration of Authenticity

Hiermit versichere ich an Eides statt, die vorliegende Dissertation selbst verfasst und keine anderen als die angegebenen Hilfsmittel benutzt zu haben. Die eingereichte schriftliche Fassung entspricht der auf dem elektronischen Speichermedium. Ich versichere, dass diese Dissertation nicht in einem früheren Promotionsverfahren eingereicht wurde.

I hereby declare on oath that this doctoral dissertation is written independently and solely by my own based on the original work of my PhD and has not been used other than the acknowledged resources and aids. The submitted written version corresponds to the version on the electronic storage medium. I declare that the present dissertation was prepared maintaining the Rules of Good Scientific Practice of the German Research Foundation and it has never been submitted in the present form or similar to any other University or board of examiners.

Hamburg, 20/06/2022

Hamburg, den | City, Date

Lindsey Ann Bultema